




University of  
Stavanger

**Faculty of Science and Technology**

## MASTER'S THESIS

Study program/ Specialization:  Petroleum Geoscience Engineering	Spring semester, 2020  Open
Writer:  Susanne S. Espeli	 (Writer's signature)
Faculty supervisor:  Main supervisor: Cooperative supervisor	Alejandro Escalona Carita Augustsson
External supervisor(s):	Harry Brandsen Equinor ASA
Thesis title:  <b>Petrophysical Evaluation of the Thinly Bedded Nordmela Formation in the Johan Castberg Field, Barents Sea</b>	
Credits (ECTS): 30 Sp	
Key words:  Nordmela Formation Thinly bedded reservoir Southwestern Barents Sea Petrophysics Johan Castberg Field	Pages: 95  + appendix: 21 pages  Stavanger, 21.06.2020 Date/year

Copyright  
by  
Susanne Solheim Espeli  
2020

**Petrophysical Evaluation of the Thinly Bedded Nordmela  
Formation in the Johan Castberg Field, Barents Sea**

by

**Susanne Solheim Espeli**

**Master Thesis**

Presented to the Faculty of Science and Technology

The University of Stavanger

**University of Stavanger**

**June, 2020**

## Acknowledgements

I would like to express my sincere gratitude to Hans Petter Norman, his team and Equinor Energy for giving me the opportunity to learn from the best! A special thanks to my external supervisor in Equinor Energy, Harry Brandsen, who has been a mentor related to petrophysics with valuable discussions, guidance and motivating challenges throughout this study. I would also like to thank Trond Anders Seland and Ørjan Berge Øygard in Equinor Energy for the support.

In addition I would like to thank the operator Equinor Energy and the partners Vår Energi and Petoro for permission to publish this thesis.

I would also acknowledge my supervisor and co-supervisor, Alejandro Escalona and Carita Augustsson respectively for helping me with the academical and geological aspects of this thesis. In addition, they have been an enormous support during these special Covid-19 times.

Furthermore, I would say thank you to my fellow student, Maren Fuglesten. We met the first day at the bachelor program and from that day she has challenged me and supported me to become better.

Lastly, I would like to thank my future husband, Sven Leseth, my two daughters, Victoria and Leah and my family and friends for all the support and understanding throughout these five years.

## Abstract

This study demonstrates how contrasting different distributions of shale in a reservoir determines the petrophysical properties. The Skrugard prospect (Well 7220/8-1), drilled in 2011, confirmed that the western Barents Sea was not only gas prone as the well struck oil and gas in the Stø and Nordmela formations. The field development plan was approved in 2018, with planned production start in late 2022. The new discovery of both oil and gas in the southwestern Barents Sea initiated several studies based on the data from two exploration wells (7220/8-1 and 7220/7-1). The Jurassic Nordmela Formation is a tide dominated formation alternating between sandstone and shale. Commonly thin shale laminae in a reservoir results in underestimation of bulk fraction hydrocarbon using conventional water saturation models such as Archie (1942). Therefore, several other methods such as Waxman and Smits (1968), Thomas and Stieber (1975) and the series receptivity model after Klein and Martin (1997) was addressed to attack this problem.

The study aims to develop a porosity-, water saturation- and permeability model that may contribute to optimize future production from the reservoir in the Nordmela Formation at the Johan Castberg Field, using three main steps: (1) Input – core data measurements will be collected and evaluated together with quality control of the well log data; (2) Petrophysical evaluation – petrophysical model(s) will be generated based on available input data; (3) Correlation, where the resultant petrophysical model(s) will be correlated with the results obtained from core measurements.

The method after Thomas and Stieber (1975) is revised and improved. Results obtained from the newly and confident series resistivity model after Klein and Martin (1997) supports that trustworthy water saturation and net-to-gross calculations can be obtained from the method after Thomas and Stieber (1975) where only gamma ray and density logs are needed. Furthermore, this method differentiate between dispersed and laminated shale which can be used to improve the permeability model and the understanding of differentiation in reservoir quality in a convincing manner.

# Table of Contents

- 1 Introduction ..... 1
- 2 Geological Setting ..... 3
- 3 Theoretical background ..... 9
  - 3.1 Shale, Clay and Clay minerals ..... 10
    - 3.1.1 Clay and silt ..... 10
    - 3.1.2 Clay minerals ..... 10
    - 3.1.3 Shale ..... 11
  - 3.2 Shale effect on well logs ..... 11
- 4 Dataset ..... 15
- 5 Method and calibration processes ..... 16
  - 5.1 Input ..... 17
    - 5.1.1 Core evaluation ..... 17
    - 5.1.2 Core plug preparation ..... 17
  - 5.2 Petrophysical evaluation ..... 19
    - 5.2.1 Volume of shale ..... 20
    - 5.2.2 Porosity model ..... 21
    - 5.2.3 Thomas and Stieber (1975) ..... 23
    - 5.2.4 Permeability model ..... 27
    - 5.2.5 Water saturation model ..... 28
  - 5.3 Correlation ..... 38
- 6 Results ..... 41
  - 6.1 Core results ..... 41
    - 6.1.1 Core description for well 7220/8-1 ..... 41
    - 6.1.2 Core description for well 7220/7-1 ..... 43
    - 6.1.3 Lithofacies results ..... 45
    - 6.1.4 Net confining pressure ..... 48

6.2 Petrophysical evaluation results .....	48
6.3 Porosity model.....	51
6.4 Thomas and Stieber (1975) .....	52
6.4.1 Well 7220/8-1 Skrugard .....	52
6.4.2 Well 7220/7-1 Havis .....	56
6.5 Permeability model .....	60
6.6 Water saturation model .....	65
6.6.1 Archie (1942) and Waxman and Smits (1968).....	65
6.6.2 Poupon and Leveaux (1971) .....	67
6.6.3 Klein and Martin (1997).....	70
6.6.4 Bulk fraction hydrocarbon results .....	70
7 Interpretation and discussion.....	74
7.1 Petrophysical quality of the Nordmela Formation .....	74
7.2 Porosity models .....	75
7.3 Thomas and Stieber (1975) methodology .....	75
7.4 Conflicting shale conductivity results .....	77
7.5 Hydrocarbon underestimation .....	77
7.6 Net sand fraction from cut-off.....	79
7.7 Permeability model .....	79
7.8 Source of errors .....	80
8 Conclusions .....	81
References .....	83
Appendix 1 .....	88
Appendix 2 .....	89
Appendix 3 .....	101
Appendix 4 .....	102
Appendix 5 .....	103

Appendix 6 .....	104
Appendix 7 .....	105
Appendix 8 .....	106
Appendix 9 .....	107
Appendix 10 .....	108



## 1 Introduction

When the hydrocarbons initially in place in a reservoir are calculated, the petrophysicist is involved in determining the average hydrocarbon-bearing thickness, the porosity and the hydrocarbon saturation in the wells (Passey et al., 2006). In addition, permeability is one of the most important petrophysical properties to understand the dynamic behavior in the reservoir (Revil and Cathles, 1999). Water saturation is generally derived using empirical relations, such as Archie's equation, based on resistivity logs and correlated with Dean-Stark saturation measurements, if possible (Springer et al., 2015). Porosity, water saturation and permeability are all petrophysical properties that are affected by shale or clay minerals. According to Passey et al. (2006), the problem of obtaining accurate petrophysical results using well logs in thinly bedded clastic reservoirs, has been recognized and addressed for more than 50 years. Because of limitations in the vertical resolution of well logs, these measure an average of the sandstone fraction and the shale fraction, which again may result in erroneous hydrocarbon volume in the reservoir (Passey et al., 2006). Knowing the distribution and fractional thickness of sandstone versus shale laminae may therefore be the key to arrive at a reliable petrophysical model. Different petrophysical models have been developed to address this problem during the last half century. New methods, such as the triaxial true resistivity scanner, have been evolved to correct for shoulder bed effects, resulting in improved hydrocarbon saturations calculated within thinly bedded reservoirs such as the Jurassic Nordmela Formation in the Johan Castberg Field in the Barents Sea.

This study aims to develop a porosity-, water saturation- and permeability model for the Nordmela Formation in the Johan Castberg Field using wells 7220/8-1 and 7220/7-1. Improved property models may contribute to optimize future production from the reservoir. The four main research questions are: (1) From core data measurements, what is the lithological alternation and distribution of sandstone and shale in the Nordmela Formation? (2) How can the Nordmela Formation be divided into separate lithological facies and do the lithological facies have any similarities regarding petrophysical properties? (3) How can these lithological facies be recognized using well logs in order to be categorized into electrofacies? and (4) Which petrophysical analyses provides the best porosity, water saturation- and permeability models in the thinly-bedded Nordmela Formation?

The petrophysical properties of the Nordmela Formation at the Johan Castberg Field have been calculated using conventional methods. Until this point the main focus has been the primary target, the overlying Stø Formation. In order to address the petrophysical properties of the Nordmela Formation accordingly, less commonly used methods and data such as Thomas and Stieber (1975) and the triaxial resistivity scanner will be used. In addition, the more conventional methods of Archie (1942), Waxman and Smits (1968) and Poupon and Leveaux (1971) will be tested to establish a reference point for the Nordmela Formation. The understanding of the lithological changes in the Nordmela Formation may be the key for success, in order to differentiate between the outcome from the various models.

## 2 Geological Setting

The Johan Castberg Field is located in the Barents Sea, 100 km NW from the Snøhvit Field, situated on the Bjørnøyrenna Fault Complex SW from the Loppa High (Figure 1). The Johan Castberg Field comprises the three prospects Skrugard (7220/8-1), Havis (7220/7-1) and Drivis (7220/7-3 S), which were drilled in 2011, 2012 and 2013 respectively (NPD, 2019a). Wells 7220/8-1 and 7220/7-1 targeted the Stø and Nordmela formations (Skjelle et al., 2011; Paulsen et al., 2012, Figure 2). The Nordmela Formation of Lower Jurassic age is a tidal dominated heterolithic formation alternating between sandstone, siltstone and shale (Worsley et al., 1988)

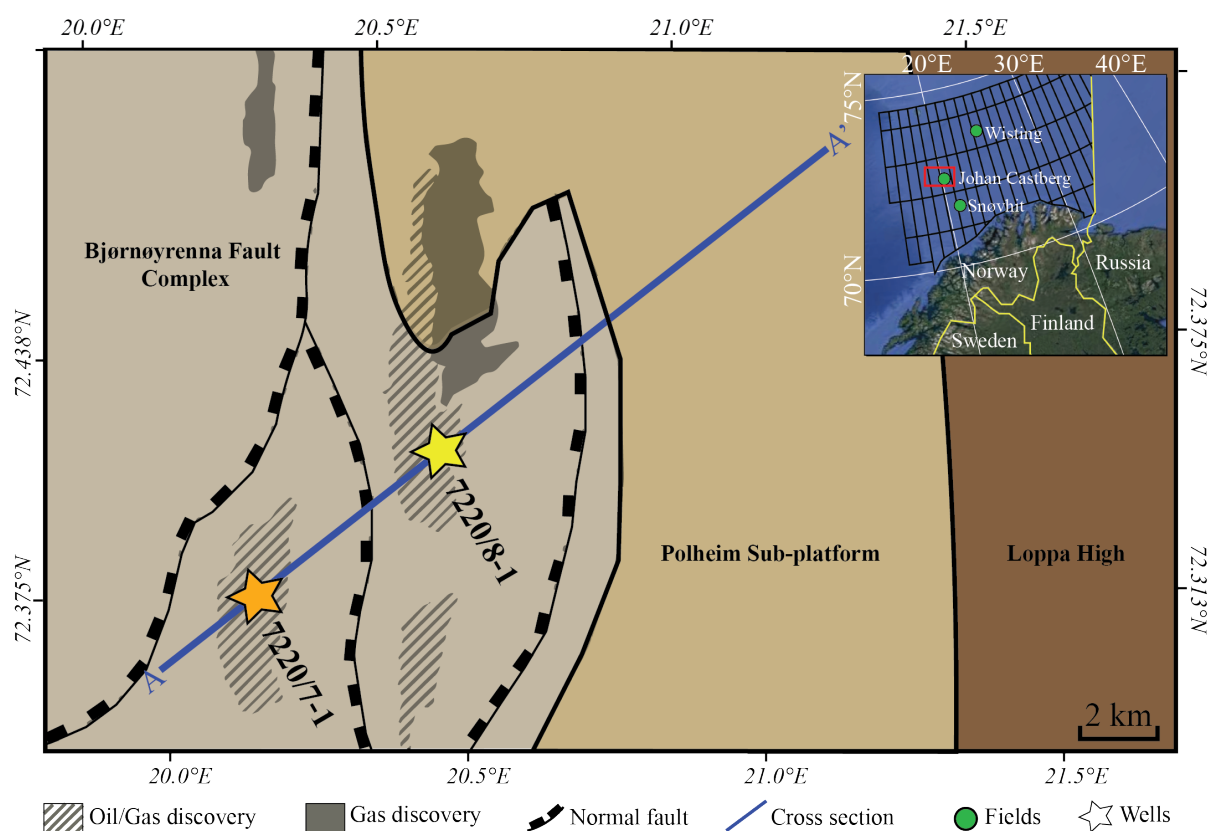


Figure 1 – The study area in the SW Barents Sea modified from NPD (2019b) and GoogleEarth (2020). The Johan Castberg Field is located on the Bjørnøyrenna Fault Complex, NW of the Snøhvit Field. The Skrugard (well 7220/8-1) and Havis (well 7220/7-1) prospects are two of three prospects forming the Johan Castberg Field. The study area comprises three main structural elements: The Loppa High, the Polheim Sub-platform and the Bjørnøyrenna Fault Complex.

The Nordmela Formation is bounded by the overlying Stø Formation and the underlying Tubåen Formation which all are part of the upper Kapp Toscana Group (Figure 2). The Kapp Toscana Group is of Upper Triassic to Lower Jurassic age. The Nordmela Formation at the Bjarmeland platform, 130 km northeast of the Johan Castberg Field, comprises of tide influenced coastal plain with some fluvial channels (Knight, 2017).

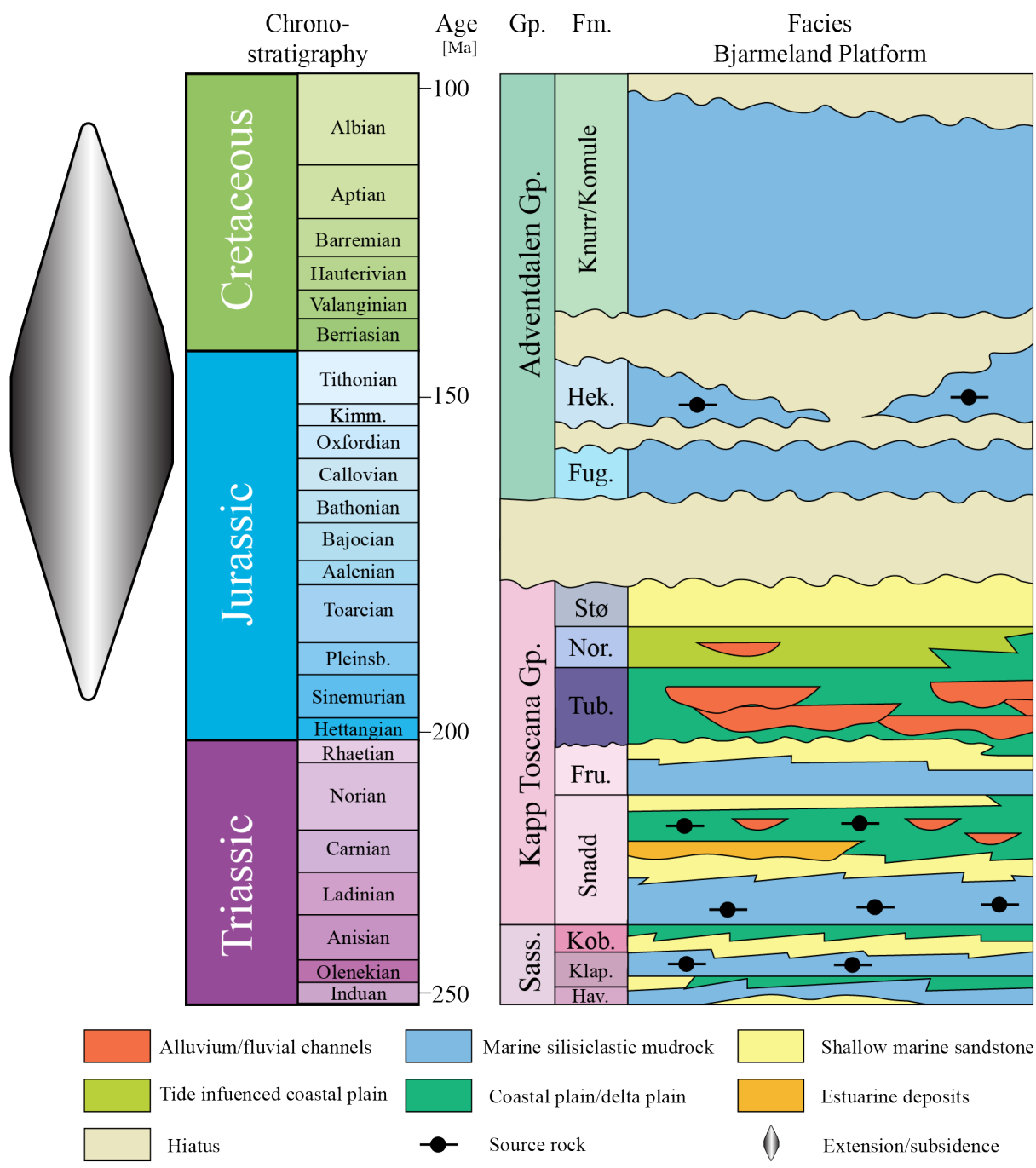


Figure 2 – Stratigraphic table of the Bjarmeland Platform (130 km northeast of the Johan Castberg Field) in the Barents Sea (modified after Knight (2017)).

Henriksen et al. (2011a) relate the numerous topographic highs and lows of the greater Barents Sea to three main tectonic phases: (1) The Caledonian orogeny leading to uplift in the west and sedimentation in the east; (2) The Late Paleozoic-Mesozoic Uralide Orogeny, which reversed the basin with uplift in the east and widespread clastic deposition in the west; and (3) The last

main phase with major rifting during the Mesozoic-Cenozoic, leading to development of the different basins in the area.

The study area is mainly controlled by three main structural elements (Figure 1), the Loppa High, the Polheim Sub-platform, and the Bjørnøyrenna Fault Complex. The Loppa High as seen today, is the result of tectonic phases during the Late Jurassic to Early Cretaceous and Late Cretaceous to Neogene. The Paleo Loppa High (also known as the Selis Rigde) rejuvenated at least four times after the Devonian and acted as a barrier to sediment supply during the Triassic (Indrevær et al., 2010). This is explained by renewed extension in the North Atlantic region with subsidence of the Selis Rigde prior to Jurassic uplift and formation of the present day Loppa High. Subsequently a depocenter was established on top of the Selis Rigde (Gabrielsen et al., 1990; Glørstad-Clark et al., 2010; Indrevær et al., 2017). The Loppa High is bounded by the Polheim Sub-platform and the Bjørnøyrenna Fault Complex in the west (Figure 1). The Polheim Sub-platform was part of the Loppa High during the Paleozoic. This part was downfaulted relative to the present day Loppa High during Lower to Middle Triassic time. The Bjørnøyrenna Fault Complex trends NE-SW (Figure 1). The age of the Bjørnøyrenna Fault complex relates to the third tectonic phase described by Henriksen et al. (2011a), and according to Gabrielsen et al. (1990) it was active during Late Jurassic to Early Cretaceous time and was reactivated again during Late Cretaceous, Paleogene and Neogene times.

The erosion in the Barents Sea from Cenozoic to recent time varies from 0 m to more than 3000 m and the process is of great importance for the petroleum system (Henriksen et al., 2011b). According to Matapour and Karlsen (2017), possible positive effects on the petroleum system such as up-dip remigration were not considered, and therefore before the Skrugard (well 7220/8-1) prospect was drilled in 2011, the western Barents Sea was considered as being only gas prone. Resultant petrography analysis from Aase (2011) and Tårup (2012) of wells 7220/8-1 and 7220/7-1 indicated uplift of 1000 m and 500 m respectively. This is based on the amount of polycrystalline quartz found in thin section of the Stø and Nordmela formations.

The main objective of the wells was to prove hydrocarbons in the Lower to Middle Jurassic Kapp Toscana Group, where oil and gas was found in the Stø and Nordmela formations in both wells. The wells are drilled in the footwall of two rotated fault blocks (Figure 3). In well 7220/8-1 (Skrugard), the gas-oil contact (red) and oil-water contact (green) could be easily identified in the seismic cross section as two flat spots (Figure 3). There is little thickness variation in the Stø and Nordmela Formations in this area, and no growth strata towards the

fault planes, indicating pre-rift sedimentation. Nevertheless Klausen et al. (2018) did a broader study of the depositional history of the area. They found that both the Stø and Nordmela formations decrease in thickness East of the Loppa High and explain this with possible local variations of subsidence and uplift in the area. Furthermore, the deposition of the two formations occurred before the Late Jurassic to Early Cretaceous rift system along the western margin of the Barents Sea platform, supporting the constant thickness in the area.

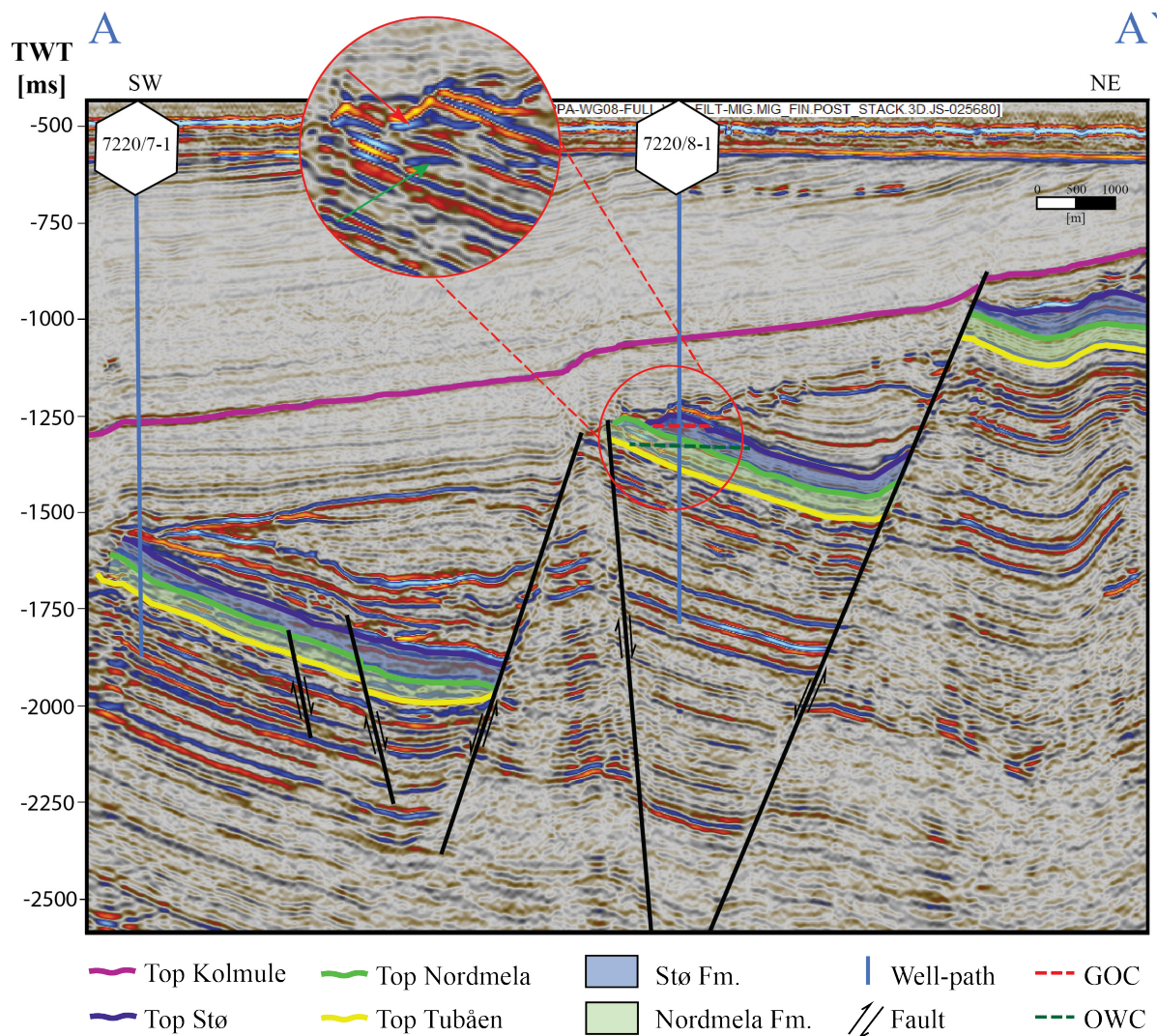


Figure 3 – Cross section A-A' (Figure 1) over wells 7220/7-1 and 7220/8-1. The two wells are positioned in the footwalls of two separate rotated fault blocks. The thickness of the Stø and Nordmela formations seems constant over this area, indicating pre-rift deposition. In well 7220/8-1 the gas-oil contact (GOC) and the oil-water contact (OWC) could be identified as two flat spots (inside red circle: red arrow marking the gas-oil contact and green arrow marking the oil-water contact). 3D seismic cube (WEST\_LOPPA-WG08) provided by the University of Stavanger.

According Skjelle et al. (2011), the Nordmela Formation consists of light to medium brown and fine to medium grained sandstone, alternating with medium to dark and grey blocky to platy claystone. The depositional environment is a tidal flat to flood plain where the individual

sandstone sequences are related to architectural elements such as estuarine and tidal channels (Worsley et al., 1988). The conceptual depositional model for the Nordmela Formation after Knight (2017) builds on data from several wells around the Loppa High and are listed from older to youngest (Figure 4):

- A. The lower and upper boundaries of Nordmela zone 1.1 is bound by flooding intervals and defined by maximum gamma ray values. The lower boundary of the zone towards the Tubåen Formation comprises of hot sand. The zone is interpreted as a prograding mouth bar complex with paleocurrent directional data in well 7220/8-1 pointing predominately to the southwest direction and in 7220/7-1 towards the south. Local differences are expected due to heterolithic interfingering of stacked bayfill, proximal and distal mouth bar and distributary channels (Figure 4, A).
- B. The top of the Nordmela zone 1.2 is defined as a flooding interval with high gamma ray and is interpreted as a prograding mouth bar complex prograding from east to west. Well 7220/8-1 is positioned in the proximal part of the delta towards the proximal mouth bar whereas well 7220/7-1 is positioned in the distal mouth bar towards the lower shoreface area (Figure 4, B).
- C. The upper boundary of the Nordmela zone 2 is defined by a flooding surface and a high peak in gamma ray. Both wells have paleocurrent directional data with a southwest direction, but more variability is observed in well 7220/7-1. Well 7220/8-1 is located in the center of the proximal mouth bar whereas well 7229/7-1 is located more in the distal part of the proximal mouth bar. This zone is thicker than the two previous where stacking of mouth bars is more dominant (Figure 4, C).
- D. The top of the Nordmela Formation and the Nordmela zone 3 is defined by a change in provenance and can also be seen in the core as a conglomerate layer, with a base of very clean sand. The prograding mouth bar complex has now slightly changed direction from a source from east to a source from the northeast. The zone is tidally influenced, creating tidal channels and tidal mouth bars. Well 7220/8-1 is located more toward the proximal part of a tidal channel than well 7220/7-1. The tidal channels are interfingered by stacked bayfill (Figure 4, D).

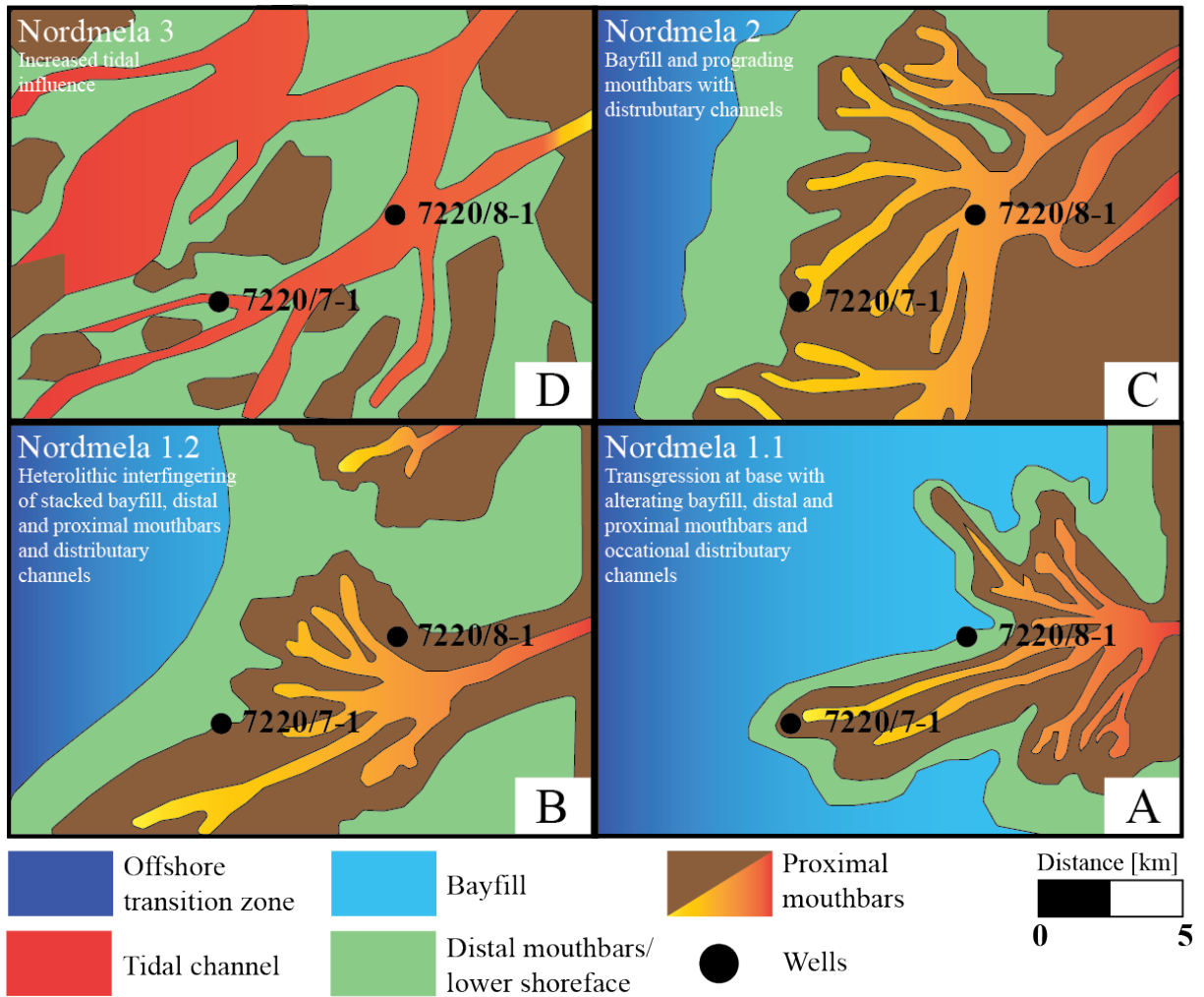


Figure 4 – Conceptual depositional model of the Nordmela Formation in the study area from oldest to youngest: (A) Nordmela 1.1 with mainly bayfill and distal/proximal mouth bars; (B) Nordmela 1.2 with a prograding mouth bar complex where the wells is located in the transition between proximal mouth bars and lower shoreface; (C) Nordmela 2 with well 7220/8-1 located in the more proximal part of the prograding mouth bar complex than well 7220/7.1; and (D) Nordmela 3 with a slightly change of direction of source from east to north-east in addition to increase in tidal influence (modified after Knight (2017)).



### 3 Theoretical background

The challenge with thin bedded reservoirs is when the resolution of the well logs fail to identify each single bed. According to Campbell (1967, p:12) a bed is defined as: “a layer of sedimentary rocks or sediments bounded above and below bedding surfaces”. There is one exception when the bed is bounded by an unconformity above and/or below. Furthermore, geological beds can be divided into laminae (Figure 5). The petrophysical definition of a thin bed is when the well logs start to fail to identify the single bed (Passay et al., 2006). For petrophysical very thin beds, core plugs and thin sections can be used to help determining the petrophysical properties of the bed or lamina (Figure 5).

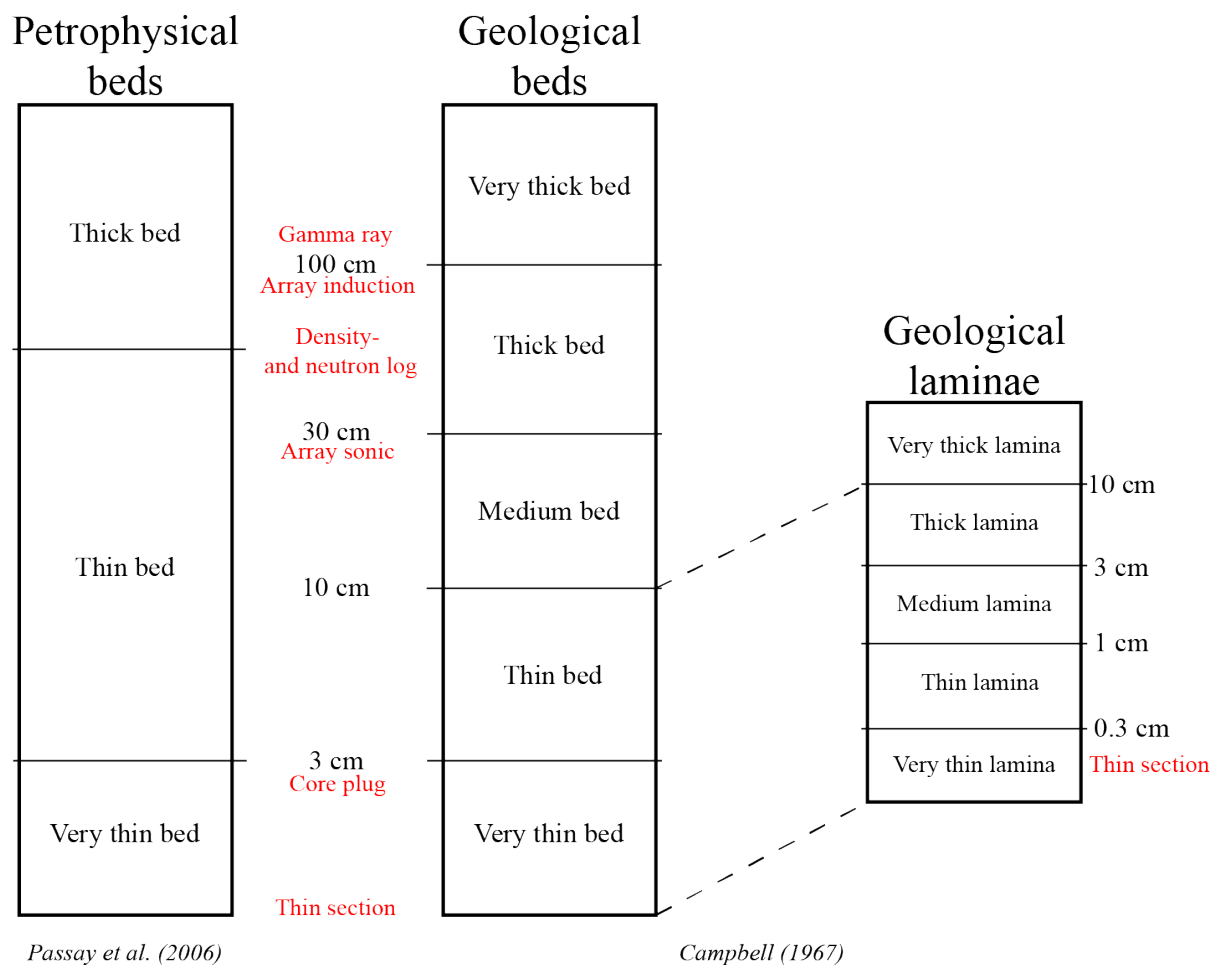


Figure 5 – Geological definitions of beds and laminae after Campbell (1967). Petrophysical definition of beds and the well log vertical resolution (red) after Passay et al. (2006).

### 3.1 Shale, Clay and Clay minerals

According to La Vigne et al. (1994), many petrophysicists interchange the terms shale, clay minerals, clay and silt. The terms therefore need to be defined in order to understand the further methods and discussion of this thesis (Figure 6).

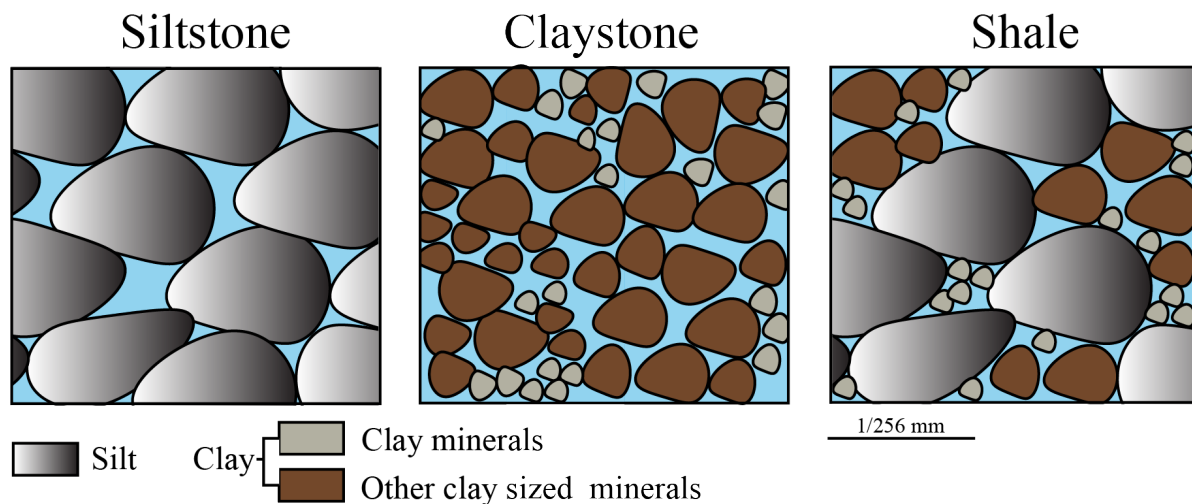


Figure 6 – Siltstone, claystone and siltstone and the relations between the size of the particles and the distribution

#### 3.1.1 Clay and silt

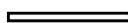
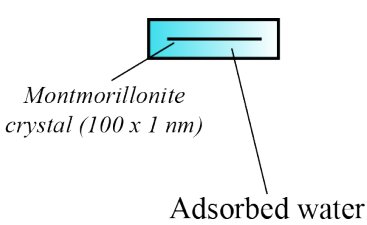
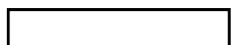
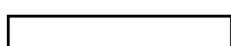

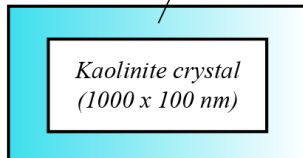
According to the Wentworth scale (Wentworth, 1922) the terms silt and clay refer to defined particle sizes (Figure 6). Silt is defined as particles between 62.5  $\mu\text{m}$  and 3.9  $\mu\text{m}$ . Below 3.9  $\mu\text{m}$ , we find clay size particles (Wentworth, 1922). Consolidated these two terms refer to siltstone and claystone respectively.

#### 3.1.2 Clay minerals

Clay minerals are phyllosilicates (silica mineral group) forming as flat sheets comprising of alternating tetrahedrons and octahedrons with silica and oxygen in the chemical formula (Bonewitz, 2012; Barton and Karathanasis, 2017). Weathering allows isomorphous substitution of cations within the clay mineral structure. This means that one structural cation is replaced for another of similar size. For example, if one  $\text{Al}^{3+}$  is substituted for  $\text{Si}^{4+}$  in the octahedron, it will result in an electrical deficit (gain of one negative charge). This will result in an imbalanced and negatively charged clay mineral (Barton and Karathanasis, 2017). To gain electrical balance the clay mineral dynamically adsorbs cations from the formation brine ( $\text{Na}^+$ ) to the surface. The cations are surrounded by  $\text{H}_2\text{O}$  molecules, resulting in the clay being bound by water. The clay mineral's ability to adsorb water is called the cation exchange

capacity. The different clay minerals have different surface areas, and the surface area together with the cation exchange capacity controls the mineral’s ability to adsorb water (Table 1 after Holz and Kovacs (1981)). As an example, despite the small size of montmorillonite it has the ability to attach a large amount of water because of the high specific surface area (Table 1).

Table 1 – Common clay minerals and their average relative size, thickness, specific surface area and size of adsorbed water layer (modified after Holtz and Kovacs (1981)).

Edge View	Typical Thickness (nm)	Typical Diameter (nm)	Specific Surface (m <sup>2</sup> /g)	Relative size of adsorbed water layer
 Montmorillonite	3	100 - 1000	800	
 Illite	30	10 000	80	Adsorbed water
 Chlorite	30	10 000	80	
 Kaolinite	50 - 2000	300 - 4000	15	

### 3.1.3 Shale

According to Tourtelot (1960) the first recorded use of the word shale is from 1747 referring to a laminated “clayey” rock developed in the English mining industry. La Vigne et al. (1994) define shale as a rock type typically consisting of 35 to 70 % clay minerals. This definition is supported by Schön (2015) who describe shale as a term for sedimentary rocks that comprise of mainly clay sized and silt sized particles (Figure 6)., and operationally some sand sized particles. Furthermore, the clay sized particles should mainly consist of clay minerals.

### 3.2 Shale effect on well logs

Onovughe and Sofolabo (2016) claim that the presence of shale can result in erroneous values of porosity and water saturation calculated from well logs. Furthermore, they describe how the resistivity log is affected by increased shale conductivity. The effect of shale on well logs was already described in 1975 by Thomas and Stieber (1975), related to the gamma ray log and the different distribution of shale. Gamma ray values are often used directly to estimate the shale

content in a reservoir, which again is used for further correction of other logs (Thomas and Stieber, 1975). However, Thomas and Stieber (1975) relate the log behavior not only to the amount of shale, but how the shale is distributed in the reservoir: laminated, dispersed and structural shale. These shale distributions are further described by Serra and Serra (2004) who divide the reservoirs into clean sandstone and shaly sandstone reservoirs, where the shaly sandstone reservoirs are subdivided into three sub-groups (Figure 7): (1) Laminated shale reservoirs, alternating between sandstone and shale, where the shale laminae may be vertical barriers for production; (2) Structural shale reservoirs, where parts of the grains are composed of shale. The mixture reflects the depositional environment, where eroded shale clasts were deposited alongside other minerals; and (3) Dispersed shale reservoirs that also are mixtures of shale and sandstone, but in this case the shale refers to clay minerals formed in a secondary process related to cementation of the reservoir or detrital shale grains. In this case the shale or clay minerals occupy pore spaces resulting in reduction of primary porosity.

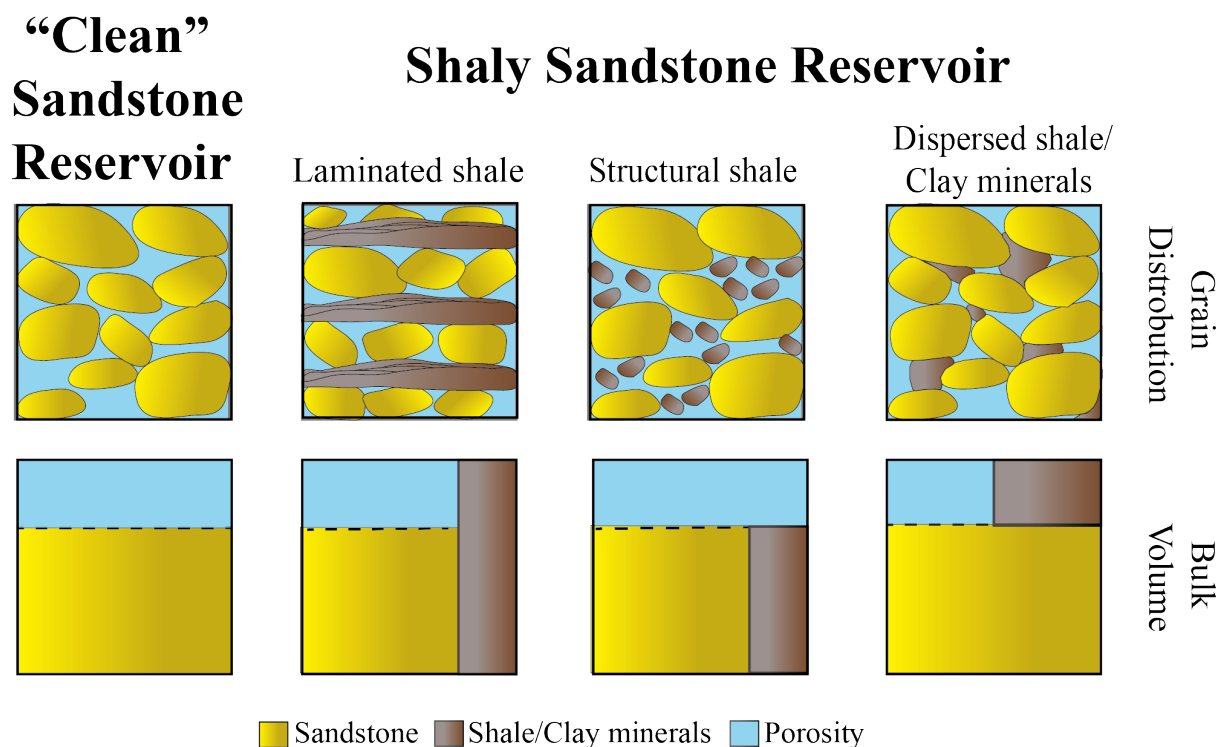


Figure 7 – Clean sandstone versus shaly sandstone reservoirs, where shaly sandstone reservoir can be further divided into (1) laminated shaly sandstone reservoirs; (2) structural shaly sandstone reservoirs; and (3) dispersed shaly sandstone reservoirs (modified after Serra and Serra (2004)).

Serra and Serra (2004) describe the clay minerals as solid conductors that affect the petrophysical properties. They summarize the conductivity of sedimentary rock comprising clay minerals as the sum of two terms: (a) the water-filled porosity referred to as free water;

and (b) the cation exchange capacity (CEC), related to the negative surface charge of the clay minerals, which attracts positive ions. The cation exchange capacity is the property that quantifies the conductive capacity of the clay, but the formation water's salinity (and temperature) is also of importance. Water saturation models such as Waxman and Smits' (1968) were developed to correct for the excess conductivity introduced by clay (Waxman and Smits, 1968; Cheng and Heidari, 2018).

Schön (2015) explained how permeability of shaly sand is controlled by clay-mineral distribution, clay-mineral types and content, porosity and confining stress. He illustrates that decreasing permeability values were related to increasing clay content. Revil and Cahles (1999) developed an improved model for permeability of shaly sand and concluded that permeability loss was related to loss of porosity due to clay filling the pore space, and that this was strongly dependent on the shale/clay fraction. Neasham (1977) documented how the dispersed clay minerals in the pore space had great impact on the permeability. Furthermore he divided the dispersed clay minerals into (1) pore-filling (discrete) clay minerals with no intergrowths such as kaolinite; (2) pore lining clay minerals such as chlorite; and (3) bridging clay-minerals such as illite that build bridges across pores. Predominantly sandstone with discrete clay minerals had the highest air permeability. Sandstone comprising pore lining clay minerals were in the intermediate permeability range. Sandstone with pore bridging clay minerals had the lowest permeability values (Neasham, 1977).

In a thinly bedded reservoir where the area of investigation covers different lithologies (such as shale and sandstone), the recorded log will read an average of the true variation (blue shaded circle, Figure 8) (Kennedy, 2015). Furthermore, the recorded well log of sandstone interval with adjacent beds of shale will be affected by the shale in the transition between sandstone and shale. This is what petrophysicist refer to as the shoulder bed effect. If the investigated bed is precisely as thick as the vertical resolution of the logging tool, the true value will be recorded in the center of the bed (orange shaded circle, Figure 8). According to Kennedy (2015), the task of a petrophysicist in these cases is: (1) to find how much of the log response comes from the net reservoir; (2) to find what would be the true log value in the net reservoir without shoulder bed effects and mixing of lithologies; and (3) to correct the log towards the true reading in order to calculate the petrophysical properties of the net sand.

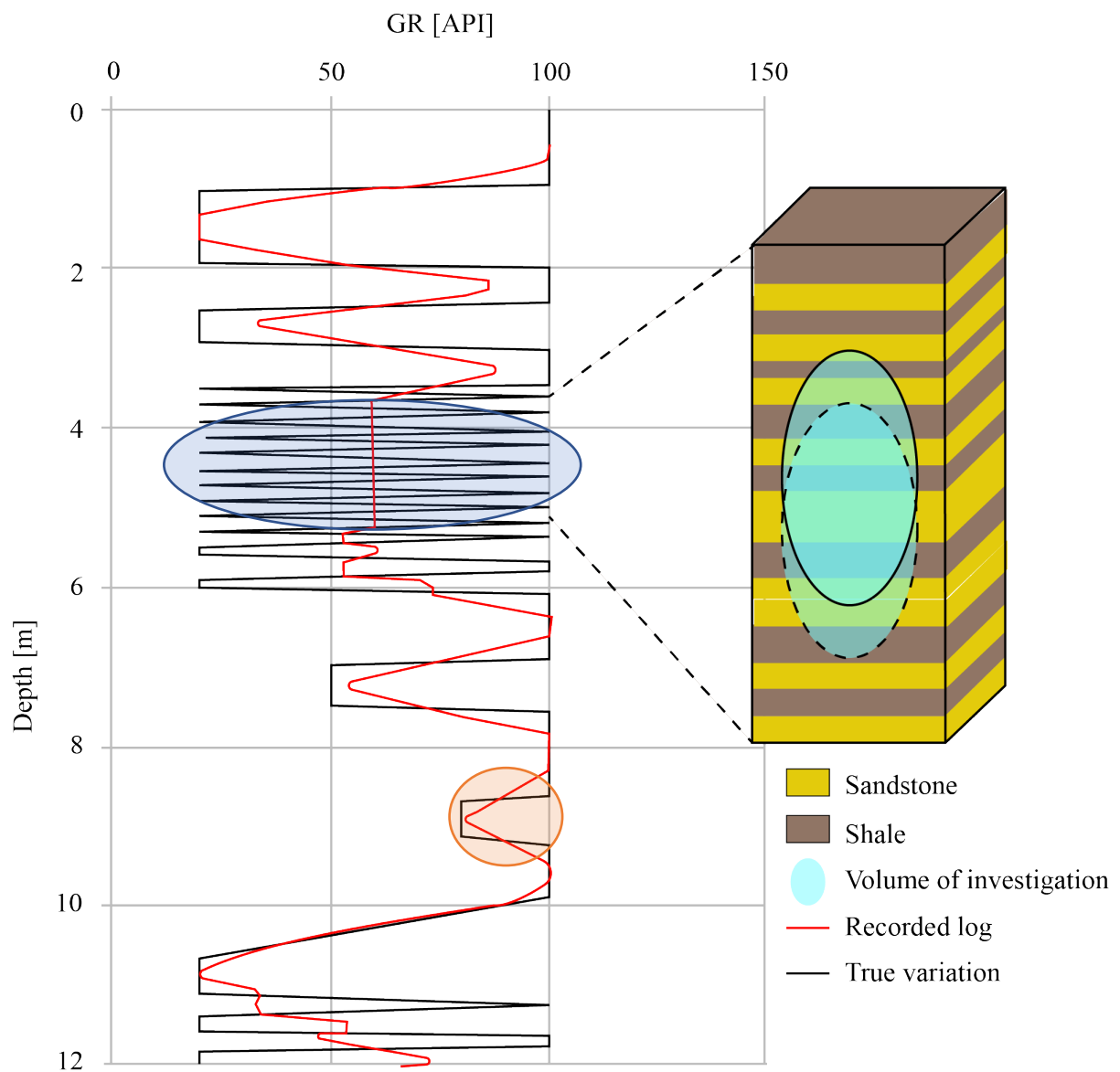


Figure 8 – Shoulder bed effect on nearby beds (below and above) and well log resolution in thin-bedded reservoir. When shale alternated with sandstone and the beds are below well log resolution the recorded is an average between the true variation, modified after Kennedy (2015). The blue shaded circle highlights an area where the recorded log is an average of the true variation. The orange shaded circle highlights an area where the vertical well log resolutions is approximately the same size as the thickness of the bed, hence the true variation is only detected in the center of the bed.

## 4 Dataset

The data available for this thesis include different well data from well 7220/8-1 and well 7220/7-1 provided by Equinor ASA (Table 2). A composite well log catalogue from both logging while drilling and wireline logging together with resistivity scanning data were available. In addition, routine- and special core analysis data for both wells were present. In well 7220/8-1 no fluid samples below the oil-water contact were taken. Internal petrography reports and thin section images, together with x-ray diffraction results and core images were included and available for this study.

Table 2 – Available dataset for the two wells, provided by Equinor ASA

7220/7-1	7220/8-1
Composite well logs <ul style="list-style-type: none"> <li>• Logging while drilling</li> <li>• Wireline logging</li> </ul> Rt-scanner	Composite well logs <ul style="list-style-type: none"> <li>• Logging while drilling</li> <li>• Wireline logging</li> </ul> Rt-scanner
Thin Sections and x-ray diffraction results	Thin Sections and x-ray diffraction results
Routine core analysis (RCA) <ul style="list-style-type: none"> <li>• Porosity</li> <li>• Permeability</li> <li>• Density</li> <li>• Dean-Stark extractions</li> <li>• Lithological description</li> </ul> Special core analysis (SCAL) <ul style="list-style-type: none"> <li>• Capillary pressure data</li> <li>• Archie's parameters</li> <li>• Waxman-Smits parameters</li> </ul> Fluid samples Core-shifts	Routine core analysis (RCA) <ul style="list-style-type: none"> <li>• Porosity</li> <li>• Permeability</li> <li>• Density</li> <li>• Dean-Stark extractions</li> <li>• Lithological description</li> </ul> Special core analysis (SCAL) <ul style="list-style-type: none"> <li>• Capillary pressure data</li> <li>• Archie's parameters</li> </ul> Core-shifts
Core (B-cut)	Core (B-cut)
Core Images	Core Images

## 5 Method and calibration processes

The workflow of the method is summarized using three main steps from preparing the input data, to the petrophysical evaluation and correlation of the resultant models with the available core data measurements (Figure 9). The porosity model was used as input for the water saturation models and the permeability model. In addition resultant calculations after Thomas and Stieber (1975) were used as input for both the water saturation model and the permeability model (Figure 9).

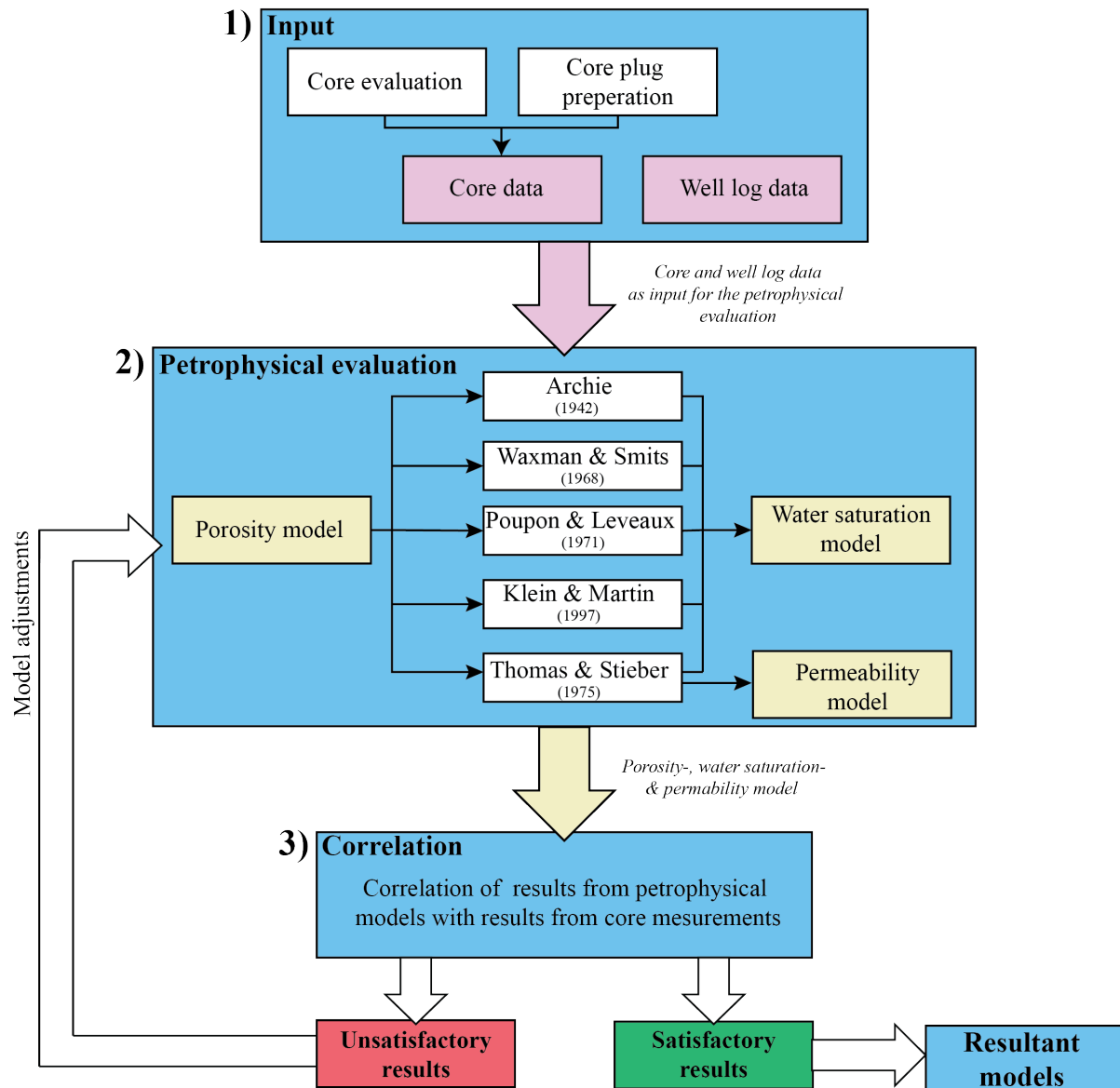


Figure 9 – Summarized workflow of the methodology using three main steps: (1) input data such as core data and well logs; (2) petrophysical evaluation with resultant models displayed in yellow; and (3) correlation, where quality control of the resultant models were correlated with available core data.



## 5.1 Input

The input for the petrophysical model comprises of core data with resultant core evaluation and the different corrected core measurements together with well logs.

### 5.1.1 Core evaluation

During core evaluation of the B-cuts, the focus was to estimate the distribution and alternation of shale versus sandstone laminae in the Nordmela Formation. Other lithological descriptions, such as facies, lamination and burrows were also recorded on core depth. Purple ultraviolet light will turn the core intervals containing hydrocarbons yellow. Thus, it can be used to detect presence of residual hydrocarbons. The ultraviolet light was used on the two cores in the oil-zone to indicate if some lithofacies did not contain hydrocarbons, implying a tight impermeable interval. Porous and permeable rocks were reflected by strong yellow light. Observations of the sandstone intervals in the core, as well as results from thin-sections and x-ray diffraction were also used to reveal if the sandstone intervals were clean sandstone or a mixture of sandstone and shale.

### 5.1.2 Core plug preparation

To be able to correlate the core data with the well logs, all core depths were shifted to match the measured depth in the logs. The core-data-shifts are derived from the gamma ray of the core correlated with the gamma ray of the well logs. The resultant core shifts that were used are displayed in Table 3, and the correction was applied to the core depth using equation 1.

Table 3 – The core shift results applied on core plugs/measurements in wells 7220/8-1 and 7220/7-1 in the Nordmela Formation. The core intervals in measured depth (MD) with the core shift for each zone.

Well	Cored Interval [MD]	Core shift
7220/8-1	1351.5 m - 1378.5 m	-0.5 m
	1378.5 m - 1405.5 m	-0.2 m
7220/7-1	1813.0 m – 1867.0 m	-1.4 m

$$\text{Log depth} = \text{Core depth} + \text{Core Shift} \quad (1)$$

Due to the overburden, the reservoir rock has been compacted. When the core (from which the core plugs later will be taken) is brought from the reservoir up to the surface, the compression from the overburden disappears. Core data measurements such as porosity and permeability are made at 20 bar confining pressure (i.e. less than in the reservoir) and are therefore

overestimated. Thus, these need to be corrected before they can be used as input and quality control for the petrophysical models. The first step was to establish the overburden pressure gradient for the Nordmela Formation in order to calculate the net confining pressure within the formation, which is defined by equation 2 (Appendix 1):

$$NCP = \frac{S_x + S_y + S_z}{3} - P_p \quad (2)$$

where the parameters are defined as follows: NCP – net confining pressure;  $S_x$  – minimum horizontal stress;  $S_y$  – maximum horizontal stress, defined as an average between  $S_x$  and  $S_z$ ;  $S_z$  – maximum vertical stress; and  $P_p$  – pore pressure.

Breckels and Van Eekelen (1983) analyzed hydraulic fracturing data to create a relationship between the horizontal stress and the depth. Minimum horizontal stress in the Nordmela Formation was calculated after Breckels and Van Eekelen (1983) using equation 3:

$$S_x = 0.0053 * D^{1.145} - 0.46 * (P_p - P_{pn}) \quad (3)$$

where the parameters are defined as follow:  $S_x$  – maximum horizontal stress;  $D$  – depth of interest;  $P_p$  – pore pressure; and  $P_{pn}$  – normal pore pressure.

Furthermore, minimum horizontal stress could be obtained from flow tests during the drilling operation. Both the minimum horizontal stress calculated after Breckels and Van Eekelen (1983) and the one obtained from flow tests in the reservoirs was used as input for the net confining pressure calculations in wells 7220/8-1 and 7220/7-1.

The maximum vertical stress was calculated by integrating the density log and adding the stress from the water column, equation 4.

$$S_z = P_w + g \int_{z_w}^z \rho(z) dz \quad (4)$$

where the parameters are defined as follows:  $S_z$  – maximum vertical stress;  $P_w$  – overburden pressure from the water column,  $z_w$  to  $z$  – depth from sea bottom to depth of interest

respectively;  $g$  – gravitational acceleration;  $\rho(z)$  – bulk density from density log; and  $dz$  – sampling interval of the density log.

Each core plug has been measured for porosity and permeability during different applied net confining pressures. Porosity and permeability were plotted against the net confining pressure. A best-fit line was made for each core plug, in order to calculate the porosity or permeability for the given net confining pressure found from in each well. Then porosity and permeability at ambient conditions could be plotted against porosity and permeability at net confining pressure respectively. A relationship ( $X_1$  and  $X_2$ ) could be established between measurements done at ambient conditions versus net confining pressure. The porosity and permeability at ambient conditions were then corrected using equation 5:

$$\varphi_{NCP} = x_1 * \varphi_{AC} \quad \text{and} \quad k_{NCP} = x_2 * k_{AC} \quad (5)$$

where the parameters are defined as follows:  $\varphi_{NCP}$  – porosity at reservoir condition;  $X_1$  correction coefficient for porosity\*;  $\varphi_{SC}$  – porosity at ambient (standard) conditions;  $k_{NCP}$  – permeability at reservoir condition;  $X_2$  – correction coefficient for permeability; and  $k_{SC}$  – permeability at ambient condition (20 bar due to capillary pressure).

## 5.2 Petrophysical evaluation

Available well log data and core data were imported, and quality controlled in the software. The zonation of the Nordmela Formation in wells 7220/8-1 and 7220/7-1 was done according to available well reports (Skjelle et al., 2011; Paulsen et al., 2012), Table 4.

Table 4 – Zonation of the Nordmela Formation from well reports in well 7220/8-1 and well 7220/7-1

<b>Zone</b>	<b>7220/8-1</b>	<b>7220/7-1</b>
	<i>Measured depth [m]</i>	
<b>Nordmela zone 3</b>	1354.10	1857.90
<b>Nordmela zone 2</b>	1379.34	1887.21
<b>Nordmela zone 1.2</b>	1458.07	1970.34
<b>Nordmela zone 1.1</b>	1494.56	2003.73
<b>Tubåen Formation</b>	1511.12	2023.48

### 5.2.1 Volume of shale

Volume of shale for wells 7220/8-1 and 7220/7-1 was calculated from the gamma ray log using equation 6 (Appendix 2, A) and from neutron-density log separation using equation 7 (Appendix 2, B):

$$V_{sh} = \frac{GR_{log} - GR_{min}}{GR_{max} - GR_{min}} \quad (6)$$

where the parameters are defined as:  $V_{sh}$  – shale volume calculated from well logs;  $GR_{log}$  – gamma ray log value;  $GR_{min}$  – gamma ray value found in a nearby clean sandstone interval; and  $GR_{max}$  – gamma ray value found in a nearby pure shale interval.

As input for the gamma ray of clean sand and gamma ray of 100 % shale in equation 6, the same values as for the laminates shale versus clean sandstone endpoints after Thomas and Stieber's (1975) envelope was used.

According to Glover (2005) the effect of bound water in shaly formations results in higher readings in the neutron log. Hence large positive separation in neutron-density separation is associated with shale. Furthermore, he claims that the size of separation in the best quantitative method for volume of shale estimation (equation 7 and Appendix 2, B):

$$V_{sh} = \frac{\gamma - \gamma_{sa}}{\gamma_{sh} - \gamma_{sa}} \quad (7)$$

where the parameters are defined as:  $V_{sh}$  – shale volume calculated from separation between neutron and density logs;  $\gamma$  – log separation;  $\gamma_{sh}$  – shale separation in 100 % shale zone; and  $\gamma_{sa}$  – sand separation in 100 % clean sandstone zone.

A neutron-density cross-plot was constructed to find the sand- and shale separation as input for equation 7 (Figure 10). The data points were colored according to gamma ray. Furthermore, only data points from Nordmela zone 2 and 3 were included whereas calcite intervals were excluded. Calcite cemented sandstone will give low or no volume of shale readings in addition to low porosity and low permeability values. A carbonate flag curve therefore was generated as 1 when the volume of shale was less than 50 % and the log porosity was less than 10 %. In other cases, the curve was set to 0. This curve could further be used to filter out values that should not be plotted (i.e. a different lithology or lithofacies).

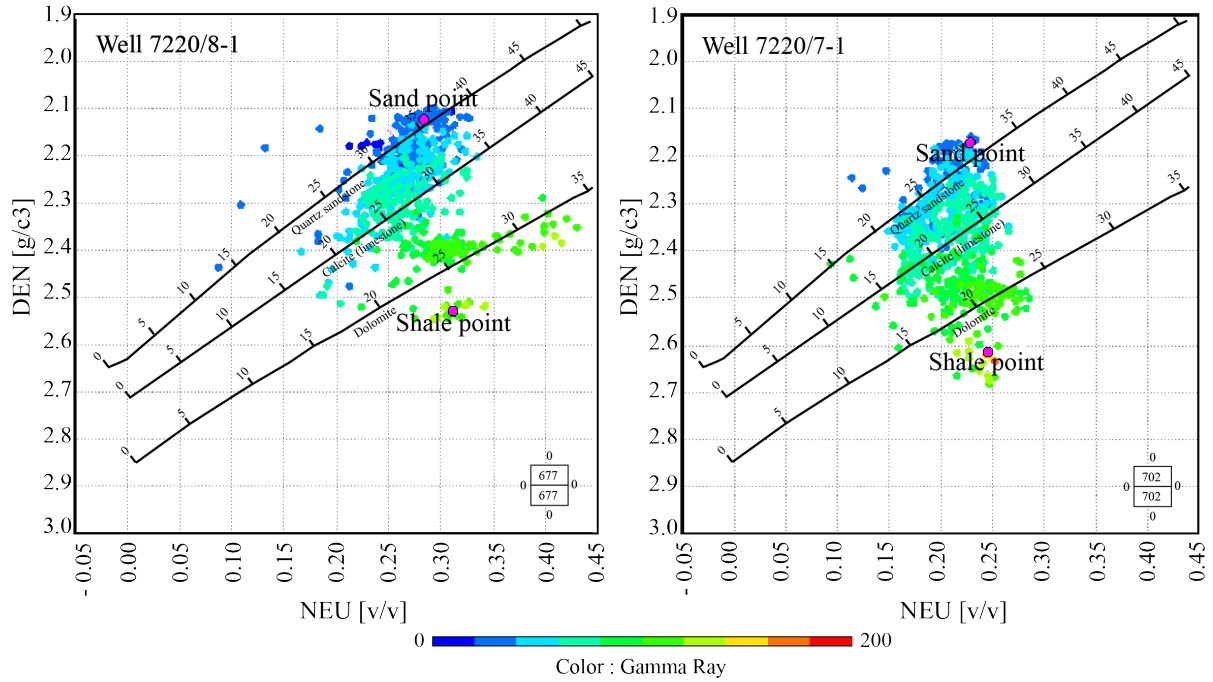


Figure 10 – Neutron-density cross-plot of wells 7220/8-1 and 7220/7-1, which was used to obtain the neutron-density separation of clean sandstone and 100 % shale. The data points were colored according to gamma ray. The iso-lines for quartz, calcite and dolomite is obtained from the porosity and lithology chart for compensated neutron log in saltwater after Schlumberger (2013).

### 5.2.2 Porosity model

The porosity model was generated using the depth and overburden corrected core plugs as references point, where the porosity from the well logs was calculated by using equation 8 (Appendix 2, C):

$$\varphi_{DEN} = \frac{\rho_{ma} - \rho_b}{\rho_{ma} - \rho_f} \quad (8)$$

where the parameters are defined as:  $\varphi_{DEN}$  – porosity calculated from density log;  $\rho_{ma}$  – density of the matrix found from routine core analyses data;  $\rho_b$  – bulk density found from the density log; and  $\rho_f$  – fluid density, found plotting the corrected porosity from core with the density derived from the density log (Figure 11). The corrected porosity values from routine core analysis controlled the sampling such that the log porosity was interpolated and sampled from the total porosity log only at core depths. A regression line was generated and forced through grain density (found from routine core analysis) reflecting zero porosity. This regression line could then be used to find the density value at 100 % porosity, which corresponds to the fluid density. With several fluid phases, such as water, gas and oil, several regression lines should be generated to get different fluid densities. The Nordmela Formation in wells 7220/8-1 and

7220/7- is located below the gas-oil contact, hence only an oil case was needed for this study. Furthermore, the density of the matrix was found by plotting the grain density from matrix (routine core analysis), creating an average for each well in addition to an average for each lithofacies.

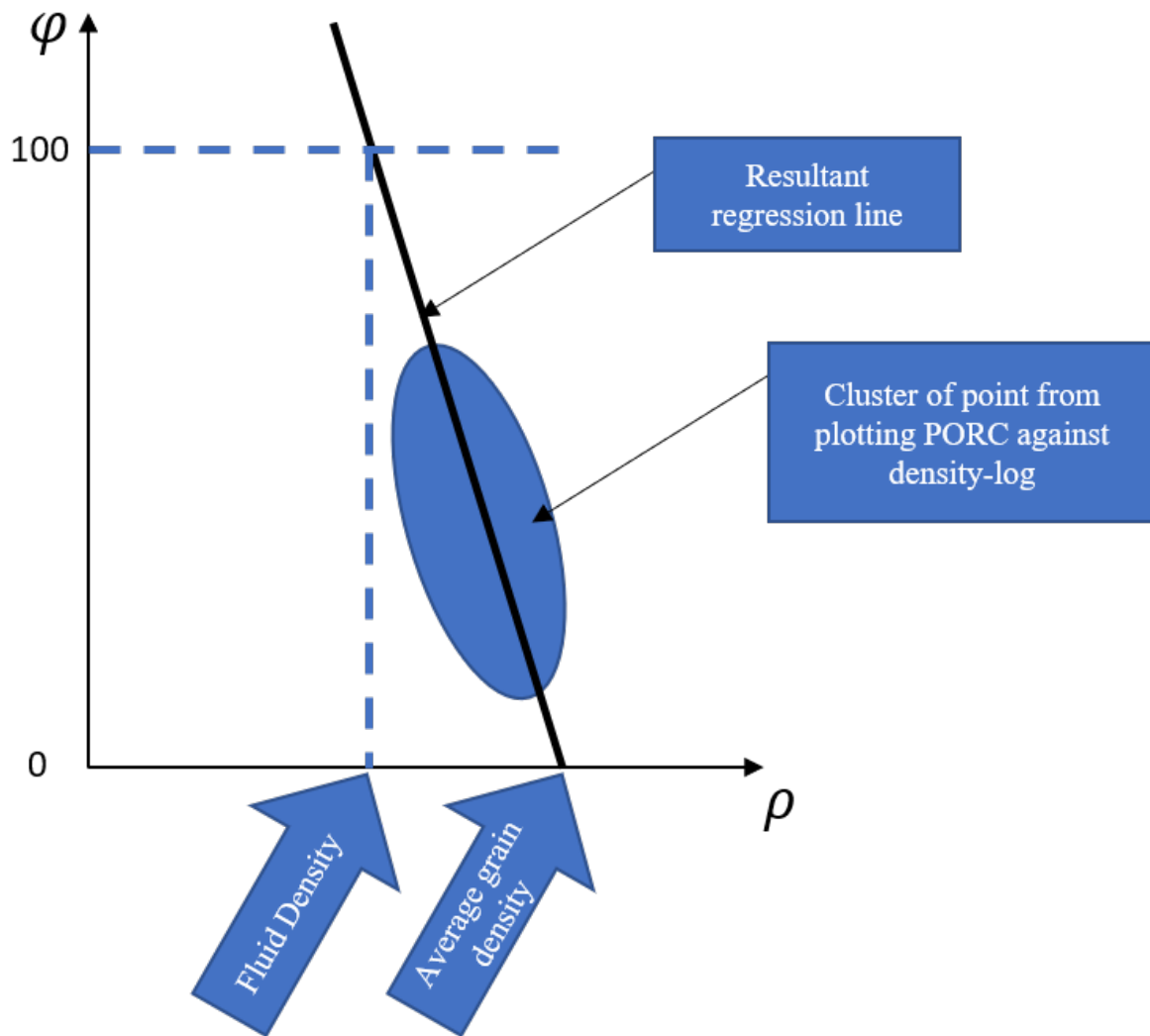


Figure 11 – Fluid density derived from cross-plotting extrapolated density from density log on x-axis against corrected porosity from core plugs (PORC) on y-axis

The porosity from sonic log was calculated after Wyllie et al. (1956), equation 9 (Appendix 2, D):

$$\varphi_{Sonic} = \frac{1}{C_p} * \frac{\Delta t - \Delta t_{ma}}{\Delta t_{fl} - \Delta t_{ma}} \quad (9)$$

where the parameters are defined as:  $\Delta t_{ma}$  – slowness (transit time) of the matrix which is commonly between 52-56  $\mu\text{s}/\text{ft}$  for sandstone;  $\Delta t_{fl}$  – slowness of the pore fluid which is commonly 189  $\mu\text{s}/\text{ft}$  default value for formation brine;  $\Delta t$  – slowness of the formation found from sonic log; and  $C_p$  – compaction factor.

The velocity-depth after Scherbaum (1982) results in a shale velocity in the Nordmela Formation around 3 km/s (transit time  $\sim 100 \mu\text{s}/\text{ft}$ ) for the two wells (taken the uplift into consideration). In addition, the transit time in adjacent shale interval in well 7220/-1 were 99  $\mu\text{s}/\text{ft}$ . Hence, 1 was used as input for the compaction factor in wells 7220/8-1 and 7220/7-1 (compaction factor = slowness of an adjacent shale layer divided by 100).

The quality control of the porosity log was done to check how the derived porosity compares to (overburden) corrected core porosities. The core depth controls the sampling, such that the log data were interpolated and sampled on core sample depth only. This was done using a frequency plot where the total porosity from routine core analysis was subtracted from total log derived porosity. An unbiased model would result in the histogram to center around zero.

### 5.2.3 Thomas and Stieber (1975)

The Nordmela Formation is a heterolithic reservoir comprising sandstone and shale intervals and where the sandstone intervals contain dispersed clay minerals. Therefore, to only use a single method such as Archie's (1942) or Waxman and Smits' (1968) for the entire formation may not give good results. The method described by Thomas and Stieber (1975) was therefore tested to obtain a better result for the water saturation calculations and permeability curve. Thomas and Stieber (1975) developed a mathematical model to relate gamma ray and total porosity to the different distributions of shale. The results are a calculated net sand fraction in addition to laminated shale and dispersed shale fractions. The net sand fraction was used as input to correct the electrical log and improve the hydrocarbon saturation calculation. The model has for simplicity some limitations: (1) There are only two types of lithologies, clean sand and 100% (laminated) shale. Shale is assumed to be the only cause for porosity loss; (2) Within one specific investigated interval, it is assumed that there is no change in sandstone versus shale mixture or shale type.

In oil saturated reservoirs where thin shale laminae alternate with sandstone laminae, the shale can act as parallel conductors and result in low resistivity values. By using the method after

Thomas and Stieber (1975), the shale laminae can be excluded from the net sand and the resistivity of the net sand can be calculated.

The Thomas and Stieber (1975) cross-plot was generated using porosity on the y-axis and gamma ray on the x-axis. The following three end points were set (Figure 12): (1) Clean sand with porosity and gamma ray found from a nearby clean sandstone zone; (2) Pure shale with porosity and gamma ray found from a pure nearby shale zone; and (3) Dispersed sand endpoint (fixed based on clean sand point and pure laminated shale point), where all the sandstone porosity is occupied by shale/clay minerals, and was calculated based on the two previous (equation 10):

$$\begin{aligned} \varphi_{disp} &= \varphi_{sh} * \varphi_{sa} \\ \gamma_{disp} &= \gamma_{sa} + (\gamma_{sh} * \varphi_{sa}) \end{aligned} \tag{10}$$

where the parameters are as follows:  $\varphi_{disp}$  – porosity of the dispersed sandstone endpoint;  $\varphi_{sh}$  – (micro) porosity of the 100 % pure shale;  $\varphi_{sa}$  – porosity of the clean sandstone;  $\gamma_{disp}$  – gamma ray of the dispersed sandstone endpoint;  $\gamma_{sa}$  – gamma ray of clean sandstone; and  $\gamma_{sh}$  – gamma ray of 100 % laminated shale.

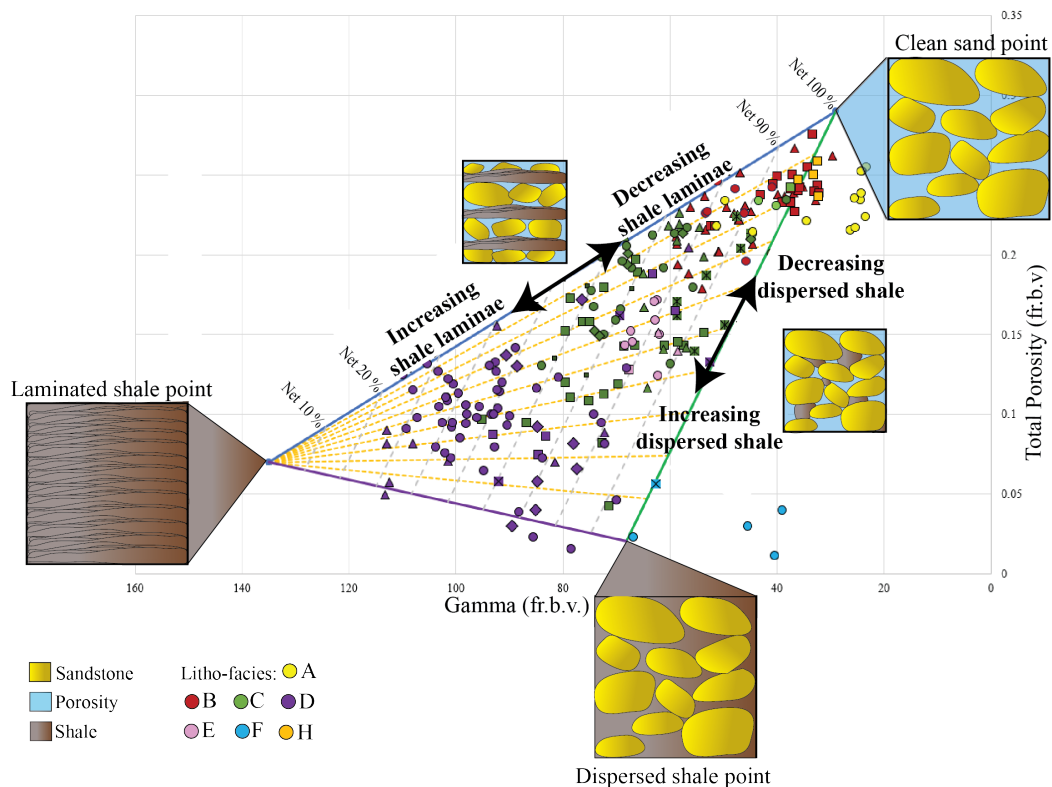


Figure 12 – Cross-plot of corrected porosity from core plugs (PORC) versus gamma ray after Thomas and Stieber (1975). End points in the diagram mark clean sand, laminated shale and dispersed shale. Arrows marking increasing shale laminae (left), decreasing shale laminae (right) and increasing dispersed shale (down).



The laminated shale point in well 7220/8-1 for Nordmela zones 1 and 2 was based on the interval from 1375.50 m to 1379.76 m measured depth. From gamma ray response and the lithology description, this interval correlated to the lithofacies I was observed in well 7220/7-1. In well 7220/8-1 a relatively clean sandstone interval from 1402 m to 1404 m measured depth was observed below the oil-water contact which was used to estimate the “clean” sandstone endpoint. Using available x-ray diffraction results from this interval, core description and porosity loss estimation cross-plot after Lundegard (1992) (Appendix 3), the total porosity of clean sandstone was predicted together with the gamma ray without shale. In well 7220/7-1 the interval from 1885.05 m to 1886.95 m measured depth was used as reference for the laminated shale end point. The clean sandstone end point for the Nordmela Formation in well 7220/7-1 was chosen based on a sandstone interval from 1923.07 m to 1927.50 m (zone 2). X-ray diffraction results were used to estimate the clean sandstone porosity after Lundegard (1992) (Appendix 4) where the gamma ray was adjusted accordingly.

In order to solve the Thomas and Stieber (1975) cross-plot mathematically, a relationship between the plotted points in respect to the diagram was established calculating the slope of each end-point line and establish a relationship to the plotted point using four equations, 11, 12, 13 and 14 (Figure 13 and Appendix 2, E). The intersection of equations 11 and 12 marked as point k (Figure 13) would result in the gamma ray value of the laminated shale (equation 15). Then equation 16 was used to determine the fraction of laminated shale. Furthermore the intersection between equation 13 and 14 is represented as point j (Figure 13), equation 17, where the gamma ray of the plotted point excludes laminated shale. From there the porosity of the net sand could be calculated from equation 18 and the relative fraction of dispersed shale from equation 19:

$$Eq_a = -A_0(x - GR_0) + \varphi_0 \quad (11)$$

$$Eq_b = -A_1(x - GR_{sa}) + \varphi_{sa} \quad (12)$$

$$Eq_c = -A_0(x - GR_{sa}) + \varphi_{sa} \quad (13)$$

$$Eq_d = -A_2(x - GR_0) + \varphi_0 \quad (14)$$

$$GR_k = \frac{-(A_1 * GR_{sa}) + \varphi_{sa} + (A_0 GR_0) - \varphi_0}{(A_0 * A_1)} \quad (15)$$

$$L_{sh} = \frac{GR_k - GR_{sa}}{GR_{sh} - GR_{sa}} \quad (16)$$

$$GR_j = \frac{-(A_2 * GR_0) + \varphi_0 + (A_0 GR_{sa}) - \varphi_{sa}}{(A_0 * A_1)} \quad (17)$$

$$\varphi_j = A_0 (GR_j * GR_{sa}) + \varphi_{sa} \quad (18)$$

$$D_{sh} = \frac{GR_j - GR_{sa}}{GR_{ds} - GR_{sa}} \quad (19)$$

where the parameters for equations 11 to 19 are as follows: Eq<sub>a</sub>, Eq<sub>b</sub>, Eq<sub>c</sub> and Eq<sub>d</sub> – equations a, b, c and d respectively for establish a relationship between the plotted point and the Thomas and Stieber (1975) envelope (Figure 13);  $L_{sh}$  – fraction of laminated shale;  $D_{sh}$  – fraction dispersed shale by clean sand porosity;  $A_0$  – Slope of equations a and c;  $A_1$  and  $A_2$  – slope of equations b and d respectively;  $GR_{sa}$  – gamma ray of the clean sand end point;  $GR_{sh}$  – gamma ray of the laminated shale end point;  $GR_{ds}$  – gamma ray of the dispersed shale end point;  $GR_0$  – gamma ray of the plotted point;  $GR_k$  – gamma ray of the intersection between equations a and b;  $GR_j$  – Gamma ray of intersection between equations c and d;  $\varphi_{sa}$  – porosity of clean sand end point;  $\varphi_{sh}$  – porosity of laminated shale end point;  $\varphi_{ds}$  – porosity of laminated shale end point;  $\varphi_0$  – porosity of plotted point;  $\varphi_k$  – porosity of intersection between equations a and b; and  $\varphi_j$  – porosity of intersection between equations c and d.

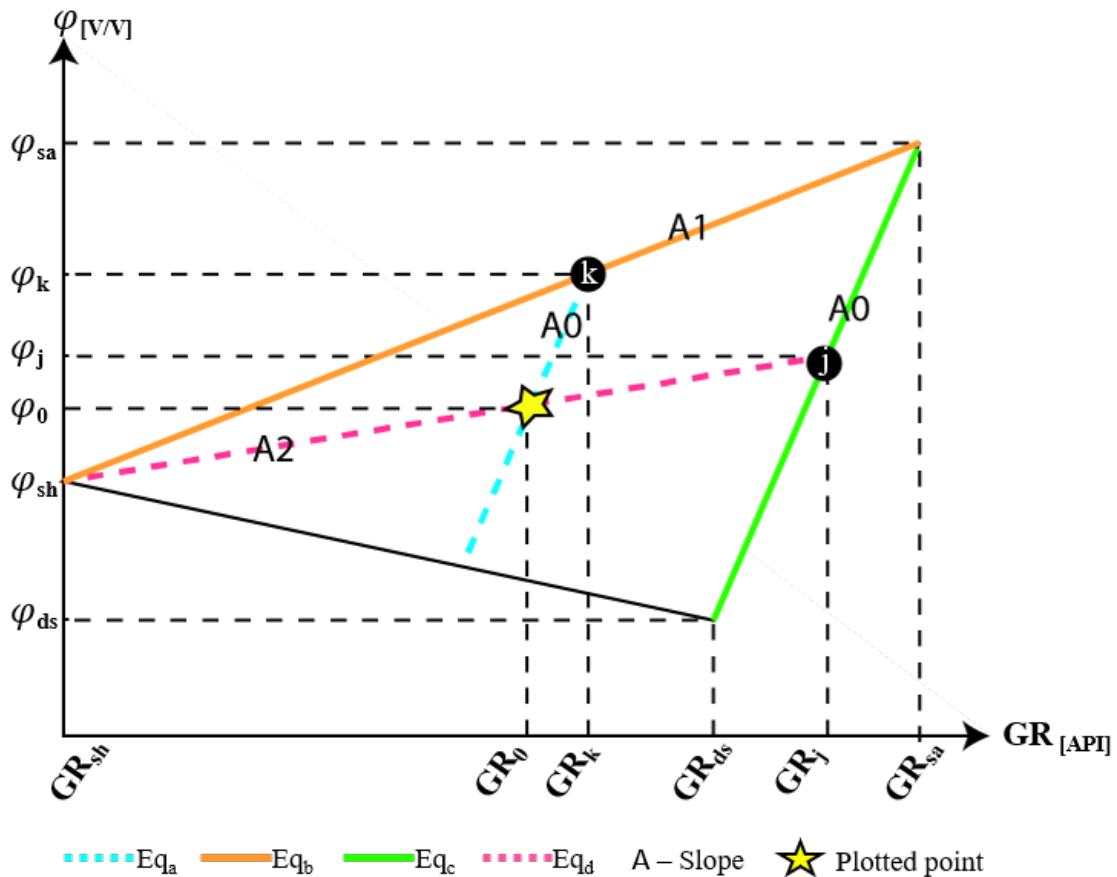


Figure 13 – Thomas and Stieber cross-plot solved mathematically using the four equations 11, 12, 13 and 14.

#### 5.2.4 Permeability model

Permeability is one of the most important properties of a rock, but it is hard to predict (e.g. Revil and Cathles (1999)). Permeability is generally strongly controlled by porosity. Therefore, the first step was to get an overview over the available data and to plot the logarithm of permeability with porosity obtained from core corrected measurements to look for trends. Based on the trends, a simple linear relation (permeability = f (porosity)) between these two could be established. Permeability is also dependent on sorting and amount of clay in the reservoirs. Therefore, a relationship with volume of shale was constructed in addition to the porosity in a multivariate linear regression (permeability = f (porosity, volume of shale)). The dependent variable permeability was regressed against independent variables such as total porosity (calculated porosity log and total core corrected porosity) and volume of shale (from gamma ray, neutron-density separation and after Thomas and Stieber (1975)). Different shale curves were tested in order to understand how these curves could predict the permeability. According to Glover (2005) the neutron-density separation is the best method to predict the volume of shale due to two variables detecting the lithologies (neutron and density log).

Nevertheless, based on the method described by Thomas and Stieber (1975) where the shale distribution is differentiated, and shale is not only considered as shale. Whether the shale is situated inside the pore space (dispersed), or as laminated layers, should theoretically affect the permeability. All data points which were marked as possible calcite were excluded in the model to describe the correlation between the dependent (to-be-predicted) variable and the independent variable(s) (inputs to the equation to the predicted equation).

The horizontal permeability was correlated with the available corrected permeability values obtained from routine core analyses. From Thomas and Stieber (1975), the sum of dispersed and laminated clay was calculated as input for the permeability. The horizontal permeability curve was generated based on porosity calculated from combined density and sonic log and from the core corrected porosity obtained from routine core measurements.

#### 5.2.5 Water saturation model

According to Springer et al. (2015), Archie's approach should be generated first as a reference point for further water saturation models. For a quality control of the water saturation model, a 100 % water saturated net reservoir zone was used. The mean water saturation in this zone should be around one. Furthermore, the estimated water saturation from the different approaches, was correlated with the Dean-Stark using the water volume (equation 20):

$$\varphi_{t_{core}} * S_{wt_{core}} * B_w = \left( \varphi_{t_{log}} * S_{wt_{log}} \right)_{\text{sampled as core in net reservoir}} \quad (20)$$

where the parameters are defined as:  $\varphi_{t_{core}}$  – Total porosity from routine core analysis;  $S_{wt_{core}}$  – total water saturation from Dean-Stark measurements;  $B_w$  – volume expansion factor for the formation brine evaluated at reservoir conditions;  $\varphi_{t_{log}}$  – calculated total log porosity; and  $S_{wt_{log}}$  – calculated total water saturation

##### 5.2.5.1 Archie (1942)

Archie (1942) demonstrated empirically the relation between the resistivity of the formation water and the resistivity of the fully water saturated core-plug for clean sandstone reservoirs. He related the resistivity to water saturation with the cementation exponent and the saturation exponent, equation (21) (Appendix 2, F):

$$S_{wt} = \left( \frac{a * R_w}{\varphi_t^m * R_t} \right)^{\frac{1}{n}} \quad (21)$$

where the parameters are defined as follows:  $S_{wt}$  – calculated total water saturation;  $a$  – tortuosity which is set as one;  $R_w$  – resistivity of the formation water;  $\varphi_t$  – total porosity;  $m$  – cementation exponent,  $R_t$  – true resistivity of the formation; and  $n$  – the saturation exponent.

A Picket plot was generated (Figure 14). On a Picket plot, resistivity is plotted against porosity (on log-log scale). The regression through the data (in the water zone) will give both tortuosity times the resistivity of the formation water (the “intercept” at porosity = 1) and the cementation exponent in the Archie equation ( $m$  is derived from the slope of the line).

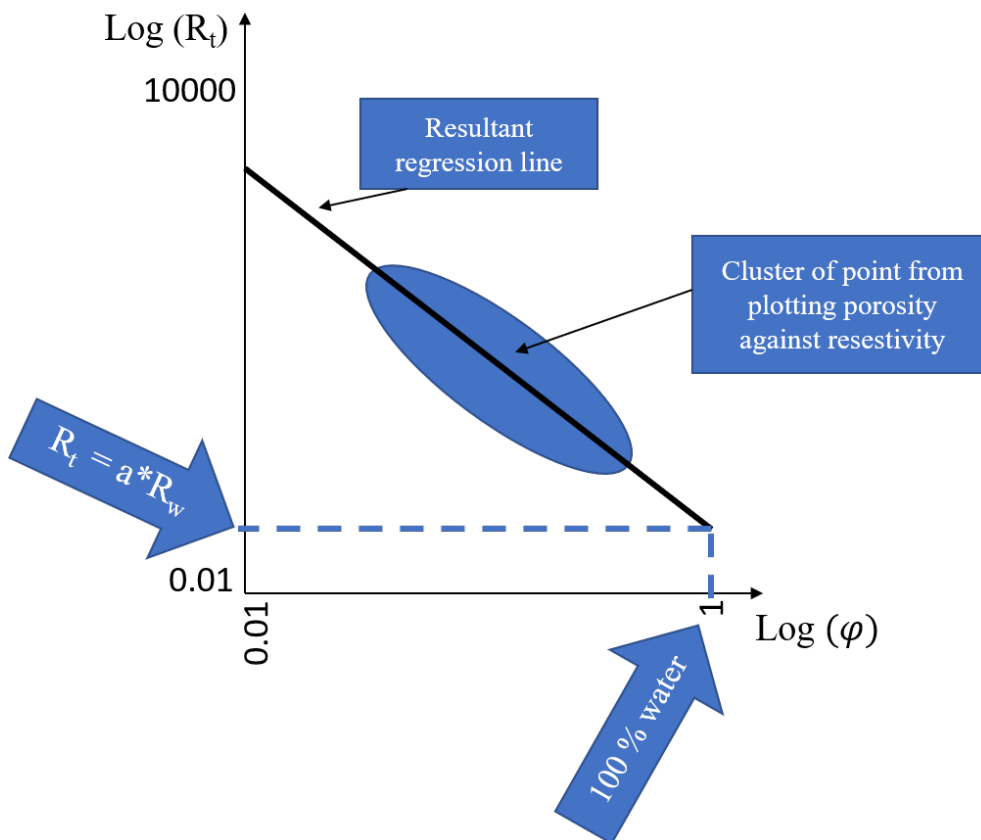


Figure 14 – Picket plot, where total porosity ( $\varphi$ ) is plotted against true resistivity ( $R_t$ ). If the water saturation after Archie (1942) is a good match, the resultant regression line of the points should in porosity equivalent to 100 % match where  $R_t = a * R_w$ . This can be correlated with water resistivity from water samples. The slope of the regression line should reflect the cementation exponent ( $m$ ).

Using data from the fluid samples in the water zones of the reservoir in well 7220/7-1, the resistivity of the water at standard condition (23.8 °C) was corrected to reservoir condition (61.6 °C) using temperature versus resistivity chart (Resistivity of NaCl solution (e.g.

Schlumberger, 2013), Appendix 5). In well 7220/8-1, no water samples were collected, therefore the density of the water was estimated from pressure gradient obtained from depth versus pressure plots in the water zone. This density was plotted against the reservoir temperature using chart (Appendix 6) which can be accessed for example from Schlumberger (2013) to retrieve the salinity of the water. Again, a chart (Resistivity of NaCl solution, Appendix 6) was used together with the salinity of the water and the reservoir temperature to estimate the resistivity of the water (e.g. Schlumberger, 2013).

Archie (1942) assumes that nothing but the brine is conductive. This is violated when shale is introduced due to presence of cation exchange capacity in the clay minerals (Cheng and Heidari, 2018). Generally, two types of shaly sand equations have been developed: (1) Cation exchange-capacity-based such as Waxman and Smits (1968) and (2) Volume-of-shale-based such as Poupon and Leveaux (1971). The resistivity log measures the true resistivity of the whole rock. Therefore, resistivity models such as Waxman and Smits (1968) are developed to compensate for the shale contribution to the log. They use cation exchange capacity per unit pore volume rock as input to correct the excess conductivity caused by the clay minerals (Waxman and Smits, 1968; Cheng and Heidari, 2018). According to Springer et al. (2015), the rule of thumb is that Archie's equation can be used for shaly sand if the clay causes less than 10 % decrease in resistivity as the difference in calculated water saturation (Archie versus Waxman and Smits) will not be significantly different (equation 22):

$$\left(\frac{R_{t_{corrected}}}{R_t}\right) = R_w * B * \frac{Q_v}{S_w} = X \quad (22)$$

where the parameters are defined as follows:  $R_{t_{corrected}}$  – true resistivity corrected by shale effect;  $R_t$  – true resistivity found from deep resistivity log;  $R_w$  – resistivity of the water;  $B$  – Ionic equivalent conductance of the exchange ion which need to be salinity and temperature corrected;  $Q_v$  – cation exchange capacity of clay dependent of amount and type of clay present; and  $S_w$  – water saturation.

#### 5.2.5.2 Waxman and Smits (1968)

Due to the clay content in the Nordmela Formation, the Waxman and Smits (1968) equation 23 for exchange cation associated with dispersed clay was tested (Appendix 2, G):

$$S_{wt} = \left( \frac{a^* * R_w}{\varphi_t^{m^*} * R_t * \left( 1 + \frac{R_w * B * Q_v}{S_{wt}} \right)} \right)^{\frac{1}{n^*}} \quad (23)$$

where the parameters are defined as follows:  $S_{wt}$  – calculated total water saturation, which is also a part of the calculation, and therefore needs to be solved mathematically by iteration;  $R_w$  – resistivity of the formation water, usually found from water samples;  $\varphi_t$  – total porosity calculated from the porosity model; and  $R_t$  – true resistivity;  $B$  – ionic equivalent conductance of the exchange ion which need to be salinity and temperature corrected;  $Q_v$  – cation exchange capacity of clay; and  $a^*$ ,  $m^*$  and  $n^*$  – which are the shaly sand tortuosity factor, shaly sand cementation exponent and shaly sand saturation exponent, respectively.

A relationship between the ionic equivalent conductance of exchange ion and ionic equivalent conductance of exchange ( $BQ_v$ ) together with volume of shale was used for each well plotting the calculated volume of shale against the  $BQ_v$  values from special core analysis (Figure 15). One regression line for each well was then established and used as input for calculating the water saturation after Waxman and Smits (1968).

According to Juhasz (1981), the equivalent conductance of the exchange cations can be approximated using equation 24 with relation to temperature:

$$B = \frac{-1.28 + 0.225T - 0.0004059T^2}{1 + R_w^{1.23}(0.045T - 0.27)} \quad (24)$$

where the parameters are as follows:  $B$  – equivalent conductance of the ( $Na^+$ ) exchange cations;  $R_w$  – resistivity of the water; and  $T$  – temperature in degrees Celcius.

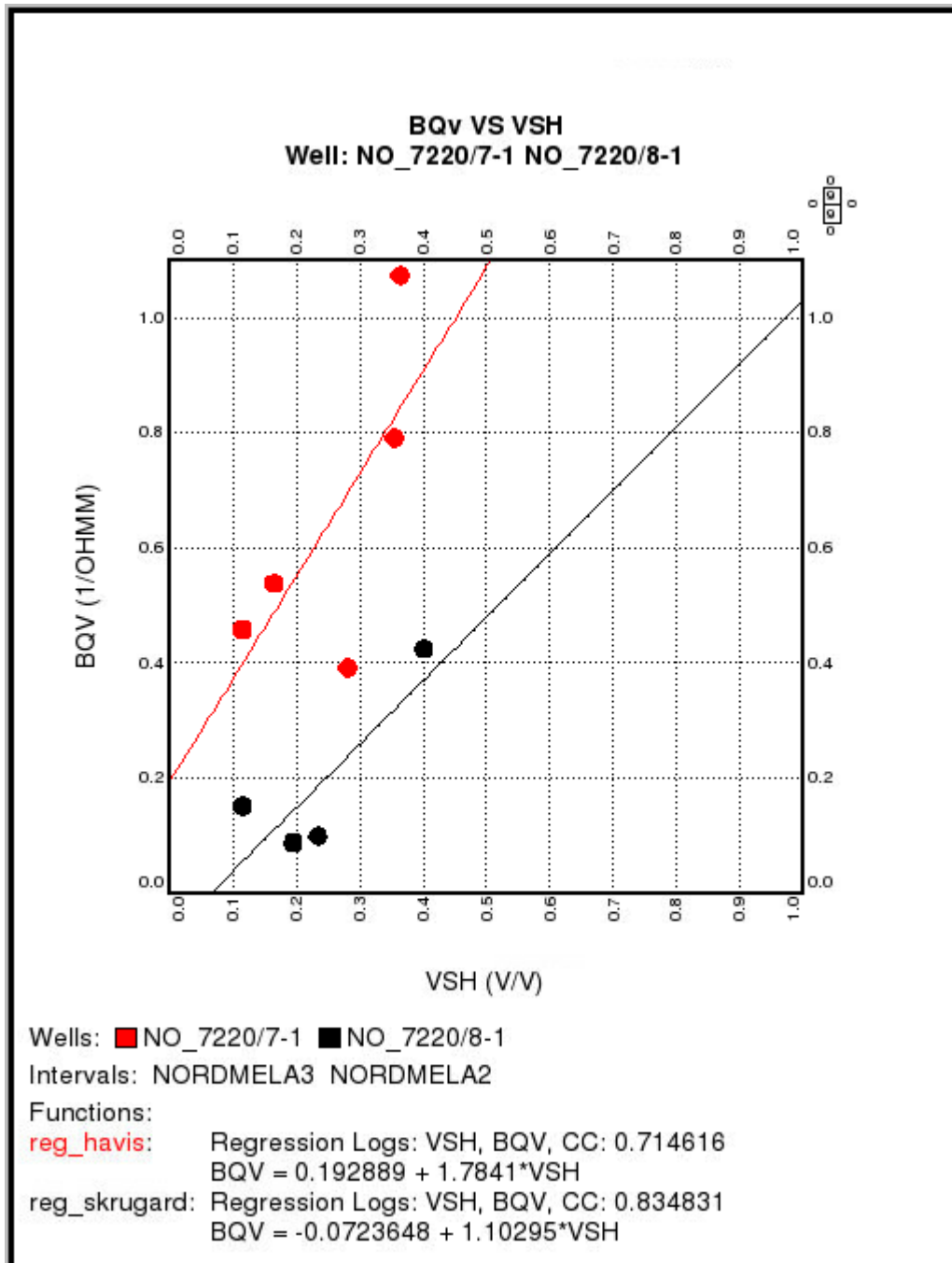


Figure 15 – Cross-plot of BQ<sub>v</sub> versus volume of shale (V<sub>sh</sub>) in order to create a relationship between the measured BQ<sub>v</sub> from core plugs and the amount of shale volume. This relationship was then applied as a function to calculate the water saturation after Waxman and Smits (1968)

From special core analyses, a combined equivalent conductance of the (Na<sup>+</sup>) exchange cations and cation exchange capacity for the shale can be obtained as parameter BQ<sub>v</sub>. In order to understand the conductance of shale in the Nordmela Formation, equation 24 was used together with the BQ<sub>v</sub> parameter to obtain the cation exchange capacity of shale.



### 5.2.5.3 Poupon and Leveaux (1971)

Poupon and Leveaux developed several equations for shaly formations which express the relationship between true resistivity related to the content of shale. Their equations are not based on the cation exchange capacity of the shale but the volume of shale alone. Like Waxman and Smits (1968), Poupon and Leveaux (1971) claim that water saturation is overestimated based on the contribution of shale conductance. Nevertheless, based on the results from the water saturation model calculated after Waxman and Smits (1968), the equations after Poupon and Leveaux chosen for the Nordmela formation were equations 25 and 26. The equations are based on an empirical relationship between volume of shale and shale resistivity related to the water saturation. Although equation 25 gave the overall best results in Poupon and Leveaux's (1971) study, equation 26 also was tested in the Nordmela Formation (Appendix 2, H). According to Poupon and Leveaux (1971), the tendency of overestimation of water saturation in formation with high shale content and low clay resistivity versus water resistivity could be corrected using equation 26 instead of equation 25.

$$\frac{1}{R_t} = \left[ \frac{(V_{sh})^{1-\left(\frac{V_{sh}}{d}\right)}}{\sqrt{R_{sh}}} + \frac{\varphi_e^{\frac{m}{2}}}{\sqrt{a * R_w}} \right] * S_{we}^{\frac{n}{2}} \quad (25)$$

$$\frac{1}{\sqrt{R_t}} = \left[ \frac{(V_{sh})^{1-\left(\frac{V_{sh}}{d}\right)}}{\sqrt{R_{sh}}} + \frac{\varphi_e^{\frac{m}{2}}}{\sqrt{a * R_w}} \right] * S_{we}^{\frac{n}{2}} \quad (26)$$

where the parameters are listed as follows:  $R_t$  – true resistivity of the formation;  $V_{sh}$  – volume of shale calculated from gamma ray log or neutron-density separation,  $d$  – factor usually set to one but can be change with relation to the individual formation;  $S_{we}$  – effective water saturation;  $R_{sh}$  – resistivity of shale found in a zone with 100 % pure shale;  $\varphi$  – effective porosity;  $m$  – cementation factor,  $n$  – saturation exponent;  $R_w$  – Resistivity of water; and  $a$  – tortuosity set to one in this case.

In order to find the resistivity of 100 % shale, a cross-plot between volume of shale and deep resistivity was constructed for the wells 7220/8-1 (red, Figure 16) and 7220/7-1 (blue, Figure 16). Only the points in the water zone were included and furthermore points interpreted as calcite were excluded to enhance the trend of the data. The transition between the Tubåen Formation and the Nordmela formation comprises of “hot” sand. Data points from Nordmela zone 1.1 was therefore excluded. The hot sand will give high gamma ray values, and hence

erroneously high volumes of shale. One regression line for each well was constructed based on the available data. The resistivity of 100 % shale was then obtained from these regression lines when the fraction of volume of shale equals one. The resultant resistivities of shale were used as input for both the Poupon and Leveaux (1971) model and for the model after Thomas and Stieber (1975).

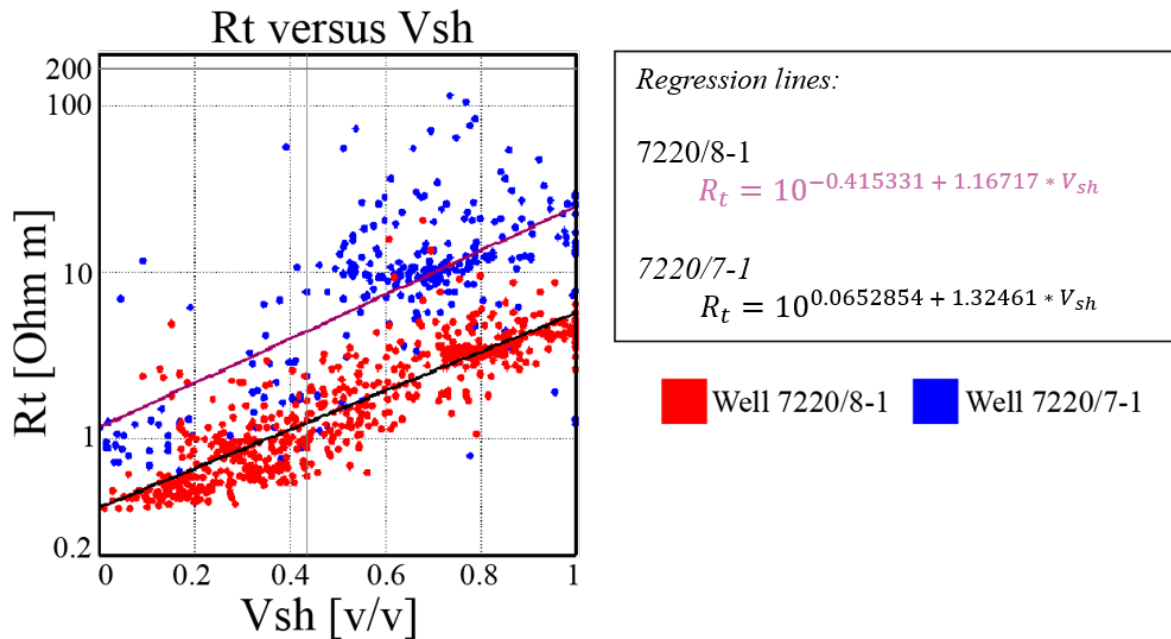


Figure 16 – Cross-plot of volume of shale (Vsh) versus deep resistivity (Rt) to estimate the resistivity of 100 % shale. This was obtained from the regression lines of the two wells when the fraction of laminated shale corresponded to one.

#### 5.2.5.4 Thomas and Stieber (1975)

The net sand found from the Thomas and Stieber (1975) calculation (Figure 13) was used together with the true resistivity log to calculate the resistivity of the sand fraction only from parallel resistivity equation 27 (Appendix 2, I):

$$\frac{1}{R_t} = \frac{f_{sd}}{R_{sd}} + \frac{f_{sh}}{R_{sh}} \quad (27)$$

where the parameters are defined as:  $R_t$  – true resistivity of the formation from deep resistivity log;  $f_{sd}$  – fraction of sandstone;  $f_{sh}$  – fraction of shale,  $R_{sd}$  – resistivity of clean sandstone found in a nearby sandstone interval within the water zone; and  $R_{sh}$  – resistivity of shale found in a nearby shale lamina interval within the water zone.

Equation 27 has a singularity point when  $1/R_t = f_{sd}/R_{sh}$ , where the function is not defined. Around this point of singularity, the function starts to become unstable. For  $1/R_t < f_{sd}/R_{sh}$  the function results in negative sand resistivity value (i.e. physically not possible). In addition, when  $1/R_t$  is nearly equal to  $f_{sd}/R_{sh}$  (but still slightly larger), the function will return positive, but extremely high values for sand resistivity. Hence, around the singularity point this function should not be used.

After the resistivity curve for the net-sand fraction (equation 27) had been generated, this curve together with the total porosity of the sand fraction was used to calculate the water saturation. Due to low clay conductivity, there is no good reason to use Waxman and Smits (1968), therefore the water saturation for the net sand was further calculated using the method after Archie (1942).

#### *5.2.5.5 Series resistivity model after Klein and Martin (1997)*

Conventional well logs cannot detect if an interval is anisotropic since the measurements are only obtained from one single direction (perpendicular to the borehole). This means that the calculations from these logs are done as if the zone was isotropic and homogenous even though the petrophysicist fully understand that rocks are not isotropic. In the Nordmela Formation, thin shale laminae alternating with sand laminae result in electrical anisotropy. Thin laminated hydrocarbon bearing-formations act anisotropic due to alternating of grain size (Hagiwara, 1997), with high resistivity in sand laminae due to high permeabilities and porosities, alternating with low impermeable and low porosity shale laminae with low resistivity values. Furthermore, the shale laminae tend to be anisotropic themselves due to the layering of the rock, crystal lattices and morphology of the clay minerals. Klein and Martin (1997) concluded that thinly bedded reservoirs could not be treated the same regarding the petrophysical properties as reservoirs composed of thicker beds. Their conclusions could only be used for resistivity data obtained from logging while drilling in highly deviated wells. Based on Klein and Martin's (1997) conclusion a logging tool which could determine resistivity both vertical and horizontally was developed by Schlumberger (Leveridge (2010)). Leveridge (2010) presented the three-dimensional true resistivity scanner containing multiple triaxial arrays measuring the vertical and horizontal resistivity together with formation dip and azimuth. The vertical and the horizontal resistivities are defined as resistivity perpendicular and parallel to bedding, respectively (Leveridge, 2010). Leveridge (2010) claims that the true resistivity

scanner will reduce uncertainties and resolve problems such as shoulder-bed effects and anisotropy in laminated pay zones. In order to obtain the fraction of net sand and the sand resistivity from the true resistivity scanner the modified Klein and Martin (1997) equations 28, 29 and 30, after Minh et al. (2007) were used (Appendix 2, J):

$$R_v = F_{sa} * R_{sa} + F_{sh} * R_{sh_v} \quad (28)$$

$$\frac{1}{R_h} = \frac{F_{sa}}{R_{sa}} + \frac{F_{sh}}{R_{sh_h}} \quad (29)$$

$$1 = F_{sa} + F_{sh} \quad (30)$$

Equations 29 and 30 are substituted into equation 28, resulting in only fraction of net sand as the unknown parameter, equation 31. Equation 31 was solved mathematically using the ABC-formula.

$$a(F_{sa})^2 + b(F_{sa}) + c = 0 \text{ where,}$$

$$a = R_h * R_{sh_h} - R_h * R_{sh_v} \quad (31)$$

$$b = 2 * R_{sh_v} * R_h - R_v * R_h - R_{sh_v} * R_{sh_h}$$

$$c = R_{sh_h} * R_{sh_v} - R_h * R_{sh_v} - R_v * R_{sh_h} + R_h * R_v$$

where the parameter for equations 28, 29, 30 and 31 are:  $R_v$  and  $R_h$  – Vertical and horizontal resistivity respectively;  $R_{sa}$  – resistivity of net-sand fraction;  $F_{sa}$  – fraction of net-sand;  $R_{sh_v}$  and  $R_{sh_h}$  – vertical and horizontal resistivity of 100 % shale respectively; and  $F_{sh}$  – fraction of shale

The shale point was chosen based on a cross-plot between horizontal- and vertical resistivity colored according to volume of shale. After the vertical- and horizontal resistivity had been chosen, equations 28, 29 and 30 were graphically illustrated using the modified Klein (butterfly) plot after Minh et al. (2007) for wells 7220/7-1 (Figure 17) and 7220/8-1 (Figure 18). Only Nordmela zones 2 and 3 were included in the cross-plot whilst carbonates were excluded using the calcite filter curve. Some data points plotted outside the butterfly cross-plot (red circle, Figure 18). These points were classified as calcite cemented sandstone from core observations. Due to total porosity calculations slightly above the limit set for the calcite filter

curve (< 10 %) these points needed to be manually excluded. The blue lines are iso-shale lines/iso-sand lines. Points plotted on the straight blue line (0.0) reflect isotropic intervals where vertical and horizontal resistivity are the same. Since the shale point is drawn northeast from this line, it is an indication of shale with anisotropy supporting the use of the series resistivity model.

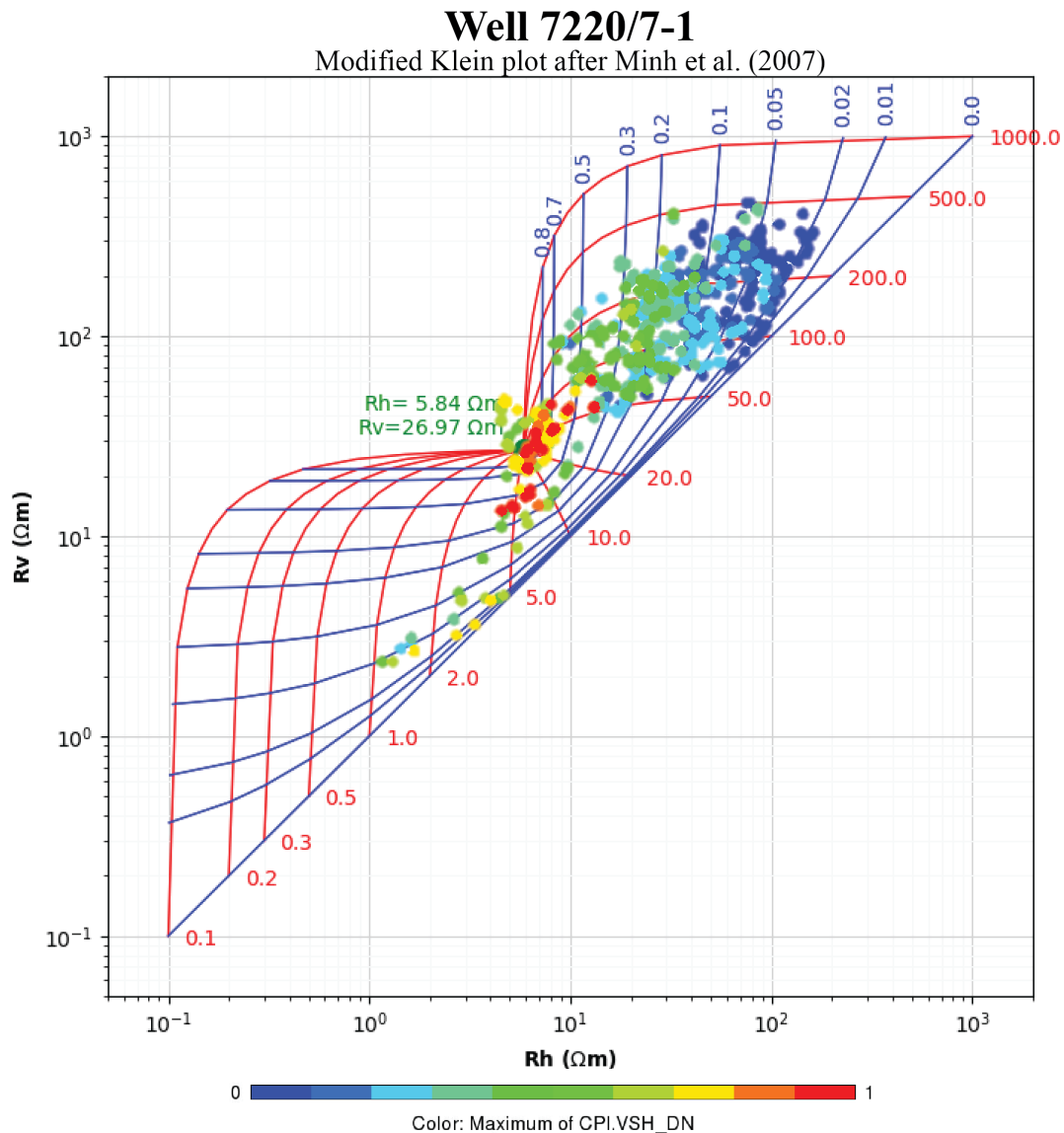


Figure 17 – Klein plot after Minh et al. (2007) from well 7220/7-1 with horizontal resistivity ( $R_h$ ) on the x-axis and vertical resistivity ( $R_v$ ) on the y-axis. The plot is made from the Nordmela Formation including Nordmela zones 2 and 3. The shale point is displayed with green letters with vertical resistivity of  $5.84 \Omega m$  and horizontal resistivity of  $26.97 \Omega m$ .

# Well 7220/8-1

Modified Klein plot after Minh et al. (2007)

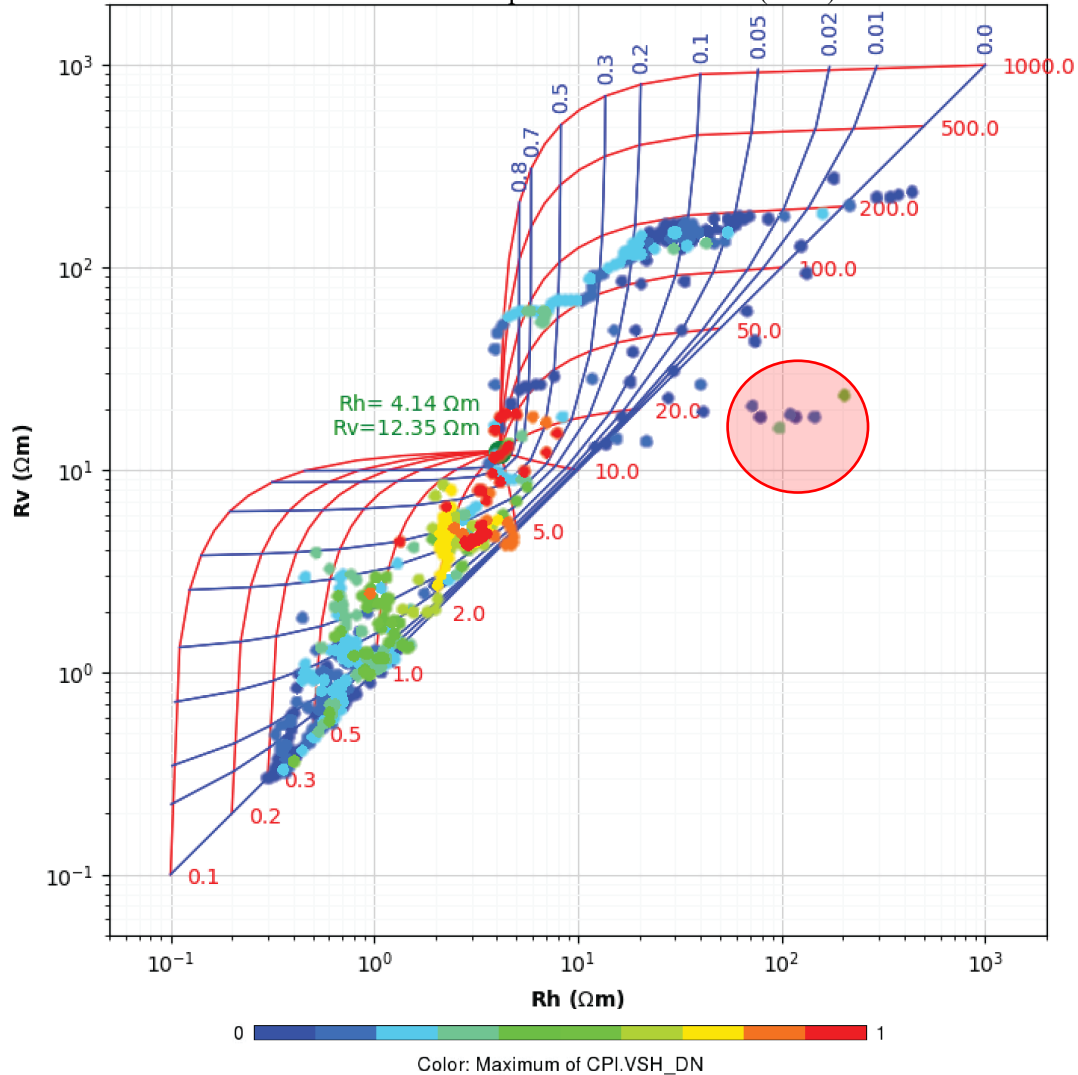


Figure 18 – Klein plot after Minh et al. (2007) from well 7220/8-1 with horizontal resistivity ( $R_h$ ) on the x-axis and vertical resistivity ( $R_v$ ) on the y-axis. The plot is made from the Nordmela Formation including Nordmela zones 2 and 3. The shale point is displayed with green letters with vertical resistivity of 12.35  $\Omega m$  and horizontal resistivity of 4.14  $\Omega m$ . Points which are plotted outside the butterfly (red circle) are calcite cemented sandstone (from core observations) which failed to be captured by the calcite curve constructed for filtration. The points have slightly higher porosity values than the limit set ( $< 10\%$ ) for the filtration curve and should not be included in the calculations.

## 5.3 Correlation

All the three models, porosity, permeability and water saturation, were correlated with available core plug measurements. The resultant models were also correlated with the interpreted lithofacies from the core. Volume of shale calculated from gamma ray cannot directly be correlated with clay mineral fractions obtained from x-ray diffraction results (Vernik, 2016) because volume of shale calculated from well logs also include silt and clay sized particles and not only clay minerals (Figure 19).

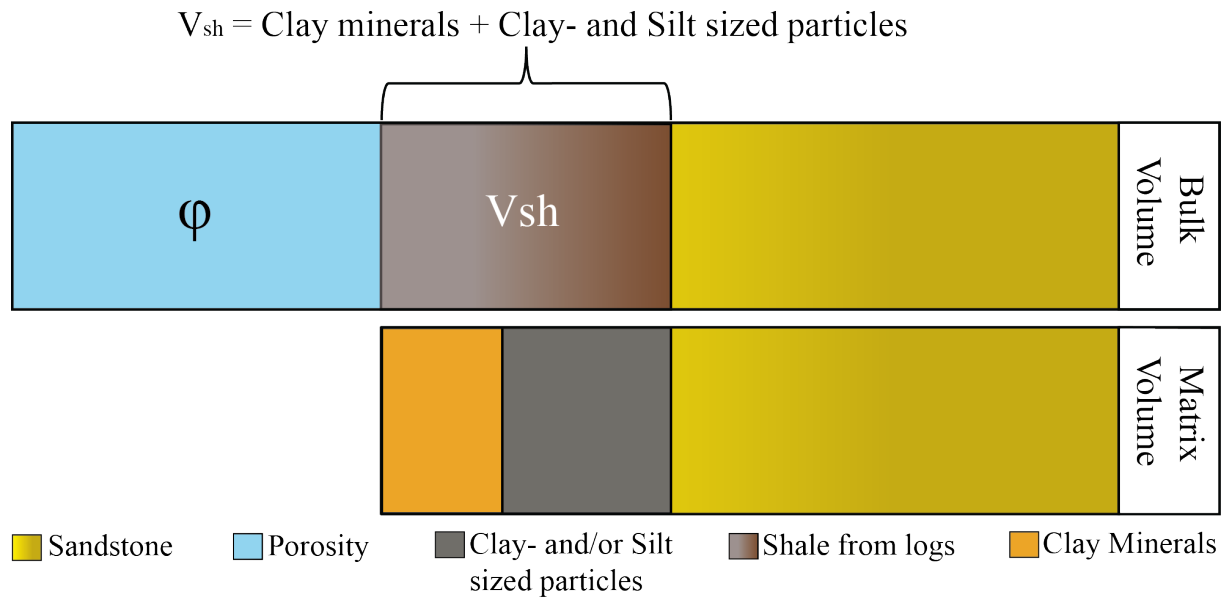


Figure 19 – Volume of shale calculated from well logs correlated with clay mineral estimation from x-ray diffraction methods. Volume of shale ( $V_{sh}$ ) is the fraction from the bulk volume, where the clay minerals from XRD is the fraction from matrix volume excluding the porosity.

With the volume of shale calculated from the gamma ray log, an estimation of bulk shale volume is obtained, whereas the x-ray diffraction results, hence clay minerals are given in weight percentage (Figure 19). Therefore, to be able to correlate the results estimated from volume of shale with x-ray diffraction results equation 32 is used to convert from weight percentage to volume percentage. Furthermore equation 33 is such that the volume percentage of the bulk is corrected to volume percentage of the bulk. Volume of shale should always be larger or equal to volume of clay minerals, related to clay mineral fraction of the shale:

$$vol\%_{mineral} = \frac{\left[ \frac{XRD_{weigh\% mineral}}{\rho_{mineral}} \right]}{\sum \left[ \frac{XRD_{weigh\% mineral}}{\rho_{mineral}} \right]} \quad (32)$$

where the parameters are as follows:  $vol\%_{mineral}$  – fraction of mineral in percentage of the bulk; numerator –  $XRD_{weigh\% mineral}$  and  $\rho_{mineral}$  mineral are the fraction in weight percentage and density of mineral respectively; denominator – sum of all  $XRD_{weigh\% mineral}$  and  $\rho_{mineral}$  mineral.

$$V_{sh_{matrix}} = (1 - \varphi) * V_{sh}$$
$$V_{sh_{matrix}} \geq V_{cl_{minerals}}$$
(33)

where the parameters are as follows:  $V_{sh_{matrix}}$  – volume of shale (excluding porosity);  $\varphi$  – porosity;  $V_{sh}$  – volume of shale (including porosity); and  $V_{cl_{minerals}}$  – clay minerals in volume percentage from x-ray diffraction.



## 6 Results

The top of the Nordmela Formation is at 1354.1 m and 1857.9 m measured depth in wells 7220/8-1 and 7220/7-1 respectively, thus with a depth difference of approximately 500 m. The thickness of the Nordmela Formation is approximately 160 m with a 9 m thicker interval in well 7220/7-1 than in well 7220/8-1.

### 6.1 Core results

The resultant lithology description for wells 7220/8-1 and 7220/7-1 displayed similarities in thickness in the Nordmela Formation with a thickness of 25 m and 25.3 m respectively.

#### 6.1.1 Core description for well 7220/8-1

Observation of the core revealed that the finer-grained Nordmela Formation zone three in well 7220/8-1 correlates with zone two, despite that several core intervals were stored as seal-peals in zone 3. The thicker sandstone bodies were observed in zone two, as fine-grained clean sandstone (Figure 20). The lower part of the core displays a grey fine to medium grained sandstone in the interval from depth 1405 m to 1402 m. In zone 2 from depth 1402 m to 1380 m, two coarsening upwards cycles was observed where fine grained sandstone was underlying the very fine-grained sandstone with bioturbation (red arrows, Figure 20). An abrupt change from the fine sandstone to the bioturbated very fine sandstone indicating an erosional surface. Calcite cemented sandstone at depth 1887 m is observed below the overlying fine-grained sandstone with parallel lamination. In zone 3, two thicker intervals of alternating sandstone and shale were observed in the intervals from depth 1368 m to 1371 m and from depth 1358 m to 1360 m with a total thickness of approximately 5 m. The amount of laminated clay was varying around 15 to 40 % in these two intervals. The thicker sandstone package in zone 3 was found from depth 1360 m to 1664 m with a coarsening upwards trend. Furthermore, the heterolithic sandstone with very thin laminae comprising of approximately 50/50 % sandstone and shale was observed in one-meter tick intervals adjacent to the seal-peal interval from depth 1372.5 to 1380 m.

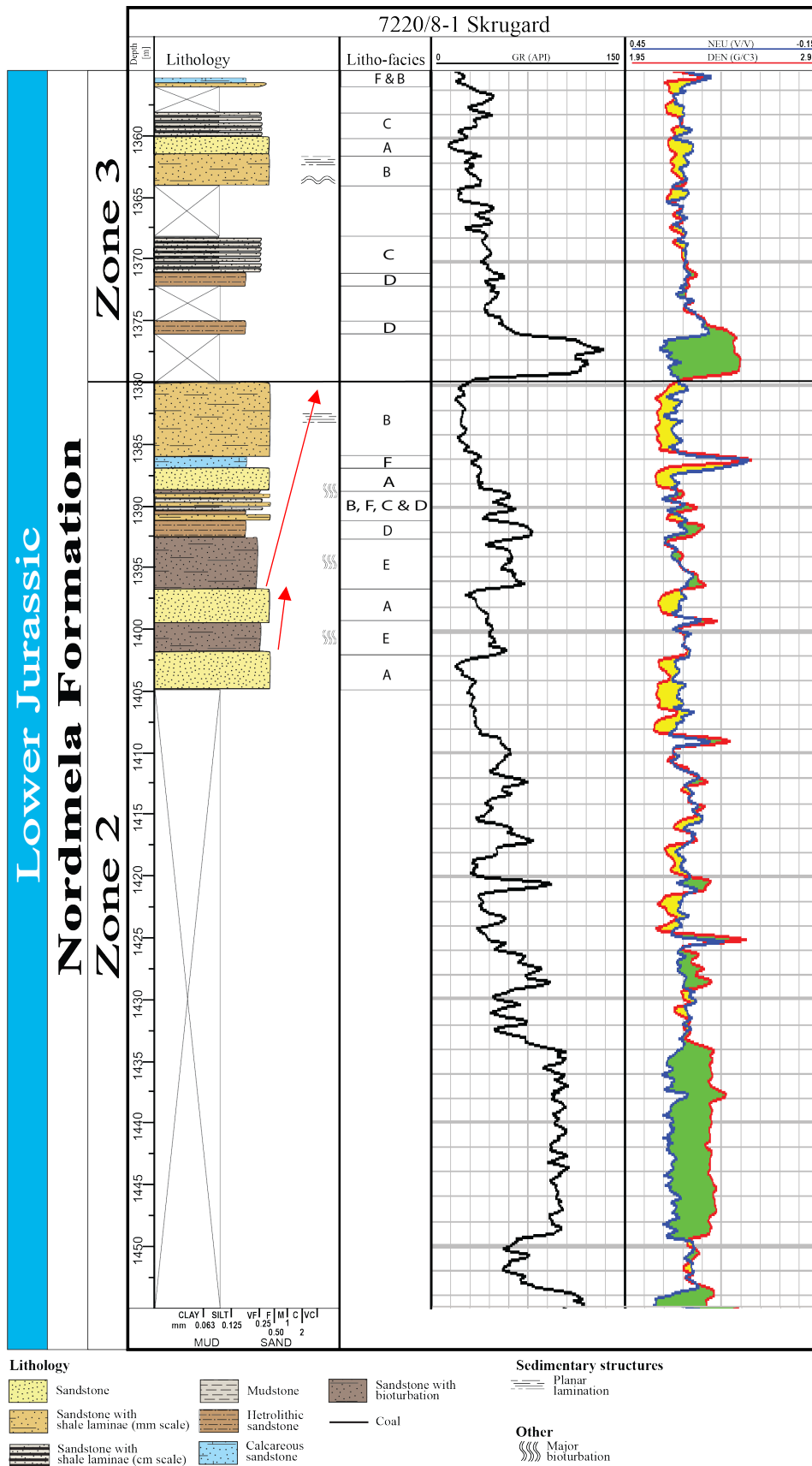


Figure 20 – Core description of well 7220/8-1. The red arrows indicating two coarsening upwards cycles.

### 6.1.2 Core description for well 7220/7-1

The lower part of the core (Nordmela zone 2) from depth 1932 m to 1960 m comprise thin to very thin laminae alternating with shale and sandstone. Some calcite cemented thin (10 cm) intervals is also seen in this lower part. Furthermore, the amount of laminated shale varies from 30 % to 50 %. Overall, the Nordmela Formation zone 2 comprises two larger coarsening upwards cycles from depth 1960 m to 1925 m and from depth 1924 m to 1894 m (red arrows, Figure 21). These two intervals are fairly heterolithic, but three thicker fine grained sandstone intervals can be found from depth 1932 m to 1925 m, from depth 1909 m to 1902 m and a 5 m thick interval around depth 1895 m. A one-meter interval above depth 1915 m includes a thick calcite cemented interval containing mud clast and some thin mud layers (mm scale). From 1894 to 1897 m an overall fining upwards cycle is observed (blue arrow, Figure 21), marking the transition between Nordmela zone 2 and zone 3 as a siltstone interval with a thickness of approximately one meter. For Nordmela Formation zone 3, an overall coarsening upward cycle is observed (green arrows, Figure 21). Starting with the siltstone marking the transition between zone 2 and 3, and into a very fine grained bioturbated interval from depth 1857 m to 1877.5 m. A thick, fine grained sandstone interval with thin shale lamination (mm scale) is overlying the bioturbated sandstone. From approximately 1875 m to 1865 m a thick interval of fine-grained sandstone is observed with thicker shale laminae (cm scale). From depth 1865 m to 1862.5 contains a bioturbated interval of fine-grained sandstone. This interval is coarser than the bioturbated interval observed from (depth) 1857 m to 1877.5 m. The top of Nordmela Formation zone three is an approximately two meter thick interval of fine-grained sandstone with some thin shale laminae (mm scale).

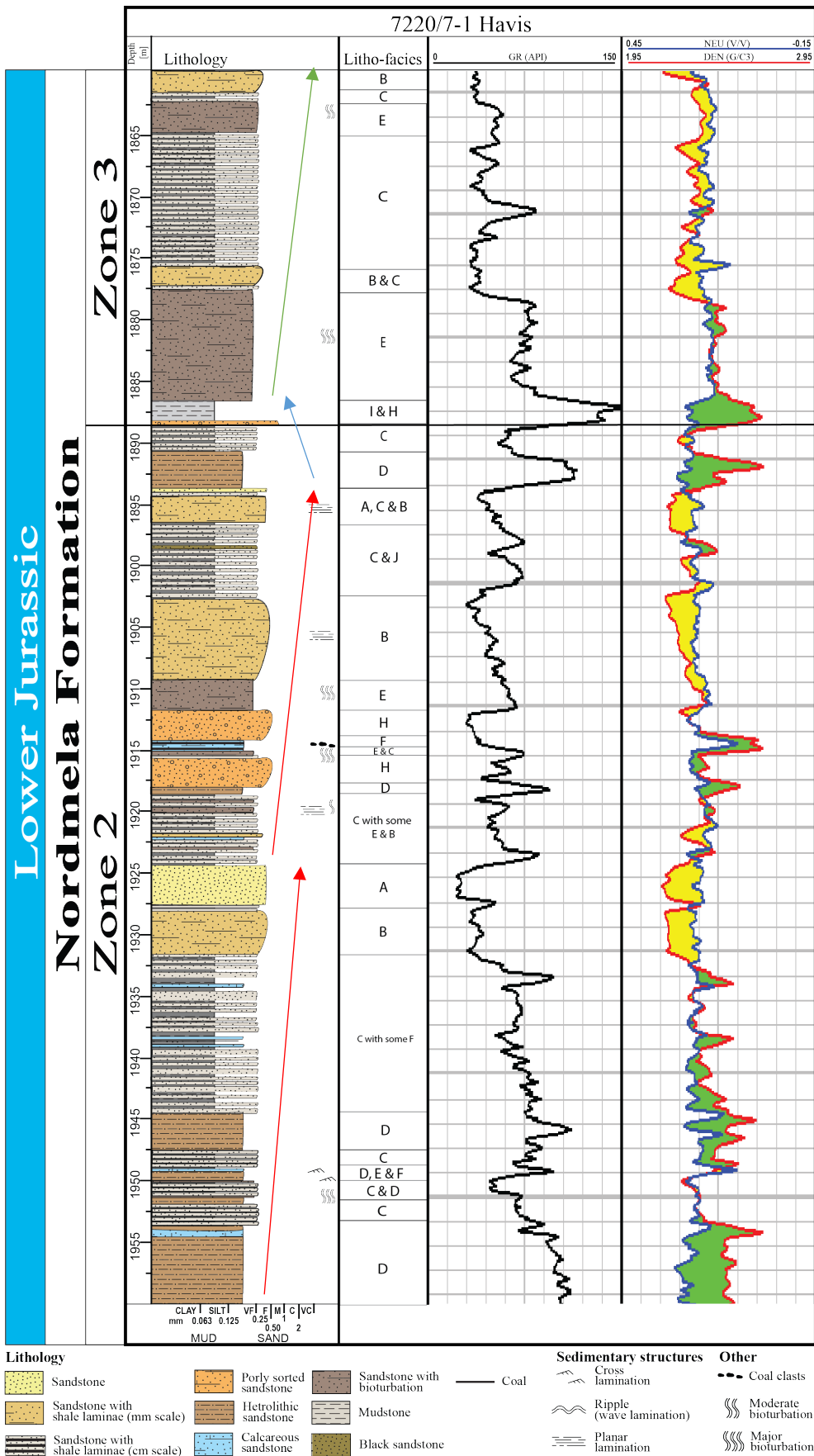
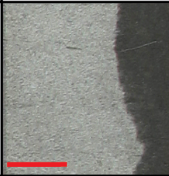
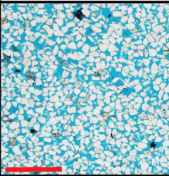

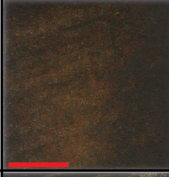
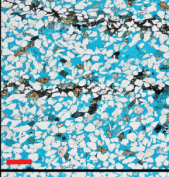

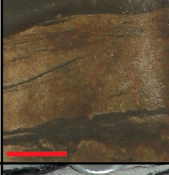
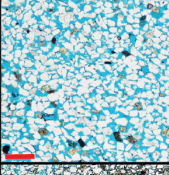
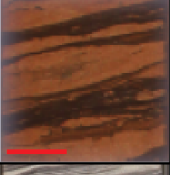
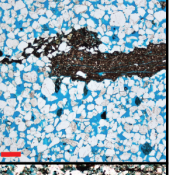
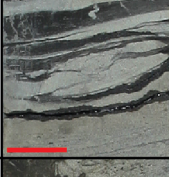
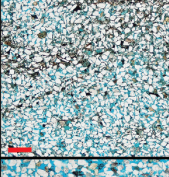

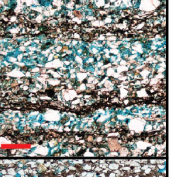

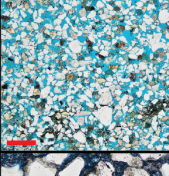
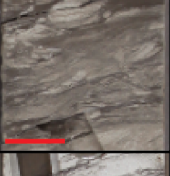
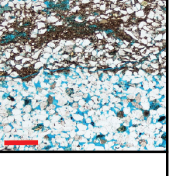

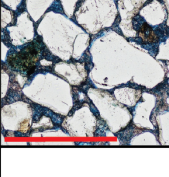



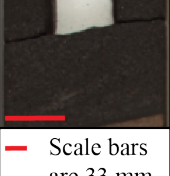
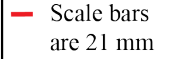
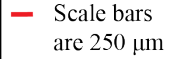
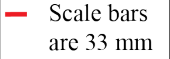
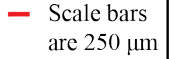


Figure 21 – Core description of well 7220/7-1. The red arrows indicating two fining upwards cycles and the blue arrow indication a coarsening upwards cycle.

### 6.1.3 Lithofacies results

The Nordmela Formation in both wells (7220/8-1 and 7220/7-1) displayed alternation between sandstone, heterolithic layering and siltstone to shale intervals. Nine different facies were observed in well 7220/7-1, whilst well 7220/8-1 only comprises of facies from one to six (Table 5): (1) Lithofacies A includes massive sandstone, with little or no shale. The thickness varies from thick beds to medium-sized beds (Figure 5); (2) Lithofacies B comprises of thin to very thin sandstone intervals with very thin to very thin lamina of shale; (3) Lithofacies C is very fine to fine grained sandstone with interbedding of medium to thin shale laminae. The sandstone interval varies in thickness but is not often observed thicker than 10 cm, which may be referred to as thin beds; (4) Lithofacies D is observed as well consolidated thick beds to thin beds. The lithofacies comprise of heterolithic very fine-grained sandstone and shale which are alternating from thin to very thin lamina scale with an estimation of approximately 50 % shale versus 50 % sandstone. Using ultraviolet light (in the oil zone) reveals little or no residual oil; (5) Very fine-grained sandstone mixed with shale and high grade of bioturbation are observed in lithofacies E. Without the bioturbation this lithological facies could represent lithofacies C or D; (6) Calcite cemented sandstones with brighter color than the rest of the lithofacies, are observed in lithofacies F. The core plugs in these intervals revealed low porosities (below 10 %) and almost no permeability (plugs largely <0.1 mD). In some intervals this lithofacies occurred in tick laminae and in other one-meter thick beds; (7) Lithofacies H comprises of very poorly to poorly sorted fine-grained to coarse-grained sandstone. This lithofacies is observed in intervals from thick beds to thin bed in well 7220/7-1; (8) A thick bed of light gray colored mudstone to siltstone corresponds to lithofacies I in well 7220/7-1. This lithofacies lied in the oil zone, but the ultraviolet light reveals little to no oil saturation; and (9) One single thin bed (15 cm) of dark to black fine-grained sandstone is marked as lithofacies J in well 7220/7-1.

Table 5 – Lithological facies interpreted from core analyses. Nine different facies are classified in well 7220/7-1. Six of them were found in well 7220/8-1.

Litho-facies	Skrugard (7222/8-1)		Havis (7222/7-1)		Description
	Core	Thin section	Core	Thin section	
A					Massive sandstone with little to no lamination. Fine grained, sub-rounded to sub-angular grains, well sorted and with little clay. Mode porosity 30.5 %
B					Fine grained sandstone with thin laminae of shale. Sub-rounded to sub-angular grains and well sorted. Mode porosity 25.5 %
C					Fine grained sandstone with thin laminae of shale. Sub-rounded to sub-angular grains and well sorted. Mode porosity 20.5 %
D					Heterolithic lamination of very fine grained sandstone with siltstone and claystone. Sub-angular grains and well sorted. Mode porosity 10.5 %
E					Fine grained sandstone with thin laminae of shale. Bioturbation. Mode porosity 15.5 %
F					Fine grained sandstone, well cemented with calcite cement. Mode porosity 3.5 %
H					Fine- to coarse grained sandstone with gray. Poor- to very poor sorted. Sub-angular grains. Mode porosity 15.5 %
I					Very well consolidated siltstone to claystone. Mode porosity 11.5 %
J					Fine to medium grained darker/black sandstone. Medium sorted and sub-angular grains. Mode porosity 23.5 %
					

The three available x-ray diffraction results from the Nordmela Formation in well 7220/8-1 are taken from lithofacies E and A (Table 6). In well 7220/7-1 six x-ray diffraction measurements are taken from lithofacies B, C and E in the Nordmela Formation (Table 7). X-ray diffraction results indicate that the clay minerals are dominated by kaolinite (3-8 wt% of the whole rock) in well 7220/8-1 and illite + mica (1-5 wt%) in well 7220/7-1 (tables 6, 7). Smectite is present only in well 7220/7-1 in trace amounts (< 1 wt% together with illite) and are found in lithofacies E.

Table 6 – X-ray diffraction results of clay minerals versus lithofacies and shale fractions after Thomas and Stieber (1975) in well 7220/8-1 where: wt% - weight percentage; fr.b.p.v – fraction by pore volume; and fr.b.v – fraction by volume

**Well 7220/8-1**

Measured depth [m]	Illite/Smectite [wt%]	Illite + mica [wt%]	Kaolinite [wt%]	Chlorite [wt%]	Lithofacies	Dispersed Shale [fr.b.p.v.]	Laminated shale [fr.b.v.]
1394.48	0	5.6	8.3	1.8	E	0.012	0.441
1397.63	0	1.1	2.8	0.6	A	0	0.190
1403.61	0	2.6	2.7	0.6	A	0.101	0.046

Table 7 – x-ray diffraction results of clay minerals versus lithofacies and shale fractions after Thomas and Stieber in well 7220/7-1 where: wt% - weight percentage; fr.b.p.v – fraction by pore volume; and fr.b.v – fraction by volume

**Well 7220/7-1**

Measured depth [m]	Illite/Smectite [wt%]	Illite + mica [wt%]	Kaolinite [wt%]	Chlorite [wt%]	Lithofacies	Dispersed Shale [fr.b.p.v.]	Laminated shale [fr.b.v.]
1864.52	0	1.3	0.5	0	C	0.0520	0.098
1881.57	0.5	5.1	1.6	0	E	0.416	0.257
1888.57	0	4.7	5.9	0.8	C	-	0.247
1903.57	0	2.4	1.2	1	B	0	0.165
1909.57	0.6	5.0	3.8	1.1	E	0.284	0.283
1927.26	0	0.6	1.5	0	B	-	0.060

#### 6.1.4 Net confining pressure

The net confining pressure in the Nordmela Formation obtained from wells 7220/8-1 and 7220/7-1 is estimated to be 100 bar and 130 bar, respectively (Table 8). The porosity and permeability corrections, respectively, are 0.986-0.970 and 0.799-0.905 (Table 8).

Table 8 – Porosity- and permeability overburden correction coefficient for core plugs measurements.

Well	7220/8-1	7220/7-1
Net Confining Pressure	80 Bar	130 Bar
Porosity Correction	0.986	0.970
Permeability Correction	0.799	0.905

#### 6.2 Petrophysical evaluation results

The porosities generally are lower (mean of 15 %) in the deeper well 7220/7-1 than in the shallower well 7220/8-1 (mean of 25 %; Table 9). Well 7220/8-1 have a mean permeability of 983 mD from 140 core plugs where well 7220/7-1 has a mean permeability of 510 mD from 538 core measurements (Table 9).

Table 9 – Mean porosity and permeability values from routine core analyses results obtain from the Nordmela Formation. The brackets indicate how many measurements the mean is based on.

Well	Nordmela Formation	
	Porosity [fr.b.v]	Permeability [mD]
7220/8-1	0.25 (151)	983 (140)
7220/7-2	0.15 (627)	510 (538)

The depth relationship between core corrected porosity measurements revealed lower porosities related to the depth trend in well 7220/7-1 than well 7220/8-2 (Figure 22, A). A less steep trend was observed when plotting the depth versus core corrected permeability (Figure 22, B). Nevertheless, there are few permeability values below 1 mD in well 7220/8-1 compared to well 7220/7-1. It can also be observed that the sampling of the core plugs is much denser and over a larger depth interval in well 7220/7-1 than in well 7220/8-1.



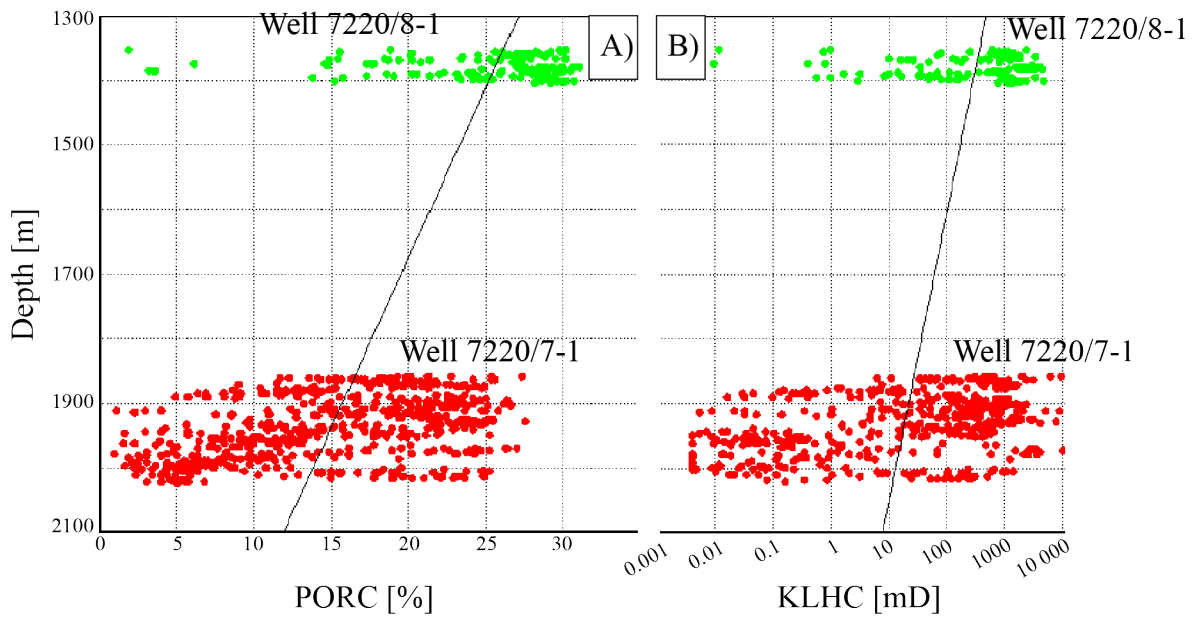


Figure 22 – Measured depth versus core corrected measurements in wells 7220/8-1 and 7220/7-1: A) Depth versus porosity and B) Depth versus permeability.

Volume of shale calculated from neutron-density separation and results from neutron and density cross-plot (Figure 10) revealed higher neutron values and lower density values for both shale and sandstone in well 7220/8-1, correlated with well 7220/7-1 (Table 10).

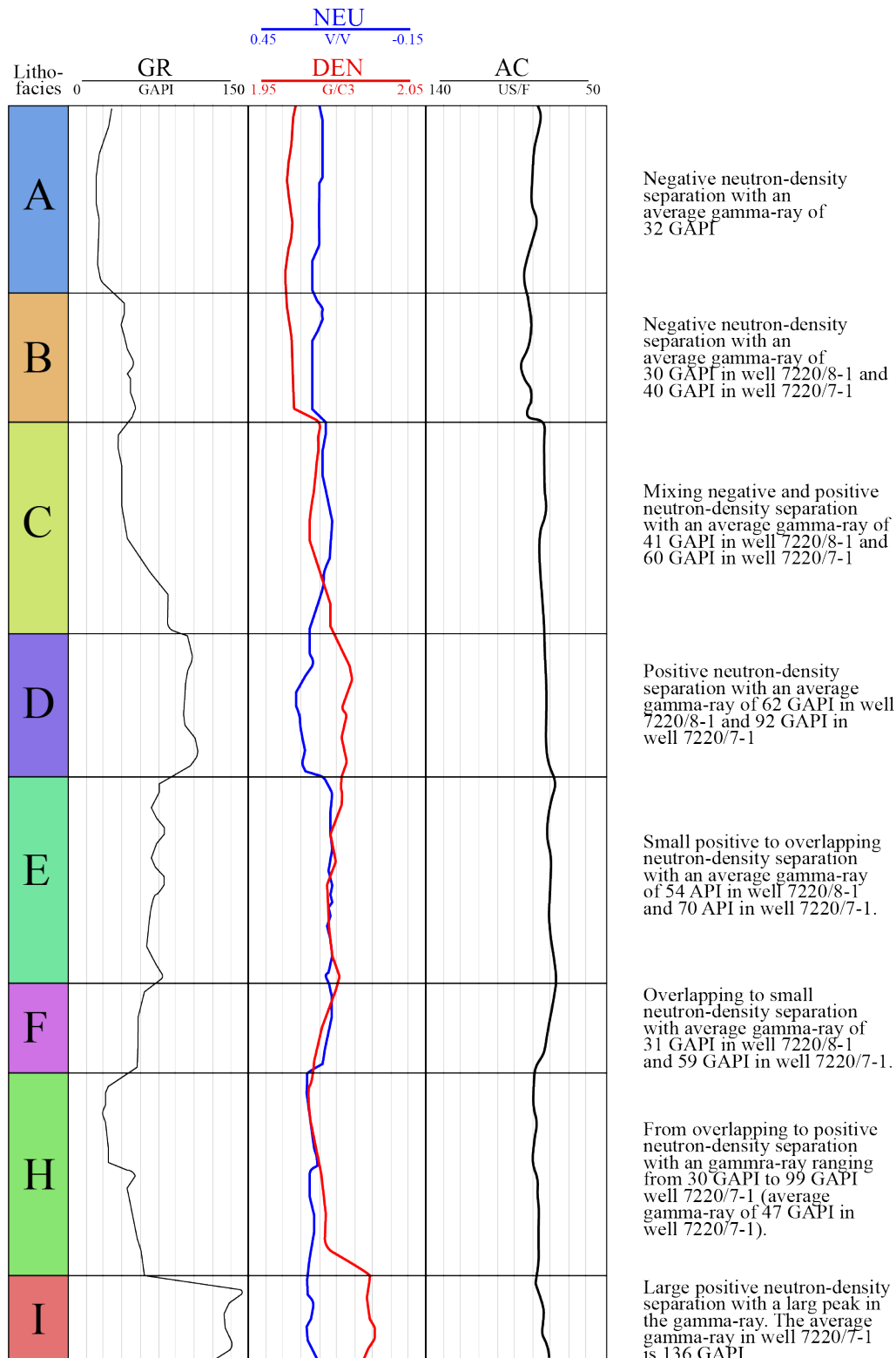
Table 10 – Resultant density- and neutron log values for calculating the volume of shale from neutron-density separation in wells 7220/8-1 and well 7220/7-1.

	Sand point		Shale point	
	<i>NEU</i> [fr.b.v]	<i>DEN</i> [g/c3]	<i>NEU</i> [fr.b.v]	<i>DEN</i> [g/c3]
7220/7-1	0.228	2.17	0.245	2.614
7220/8-2	0.284	2.123	0.312	2.529

The gamma ray values are lowest for lithofacies A, with an increasing trend via B, C, E, and D to lithofacies I (Table 11). The neutron-density separation in lithofacies A and B are negative (sand separation), whereas lithofacies D and I have a positive neutron-density separation (shale separation). Lithofacies E is commonly seen as a positive neutron-density separation but also, they are often observed overlapping. In lithofacies C, the neutron-density separation generally was observed as a negative sand separation but is also commonly observed as a positive neutron-density separation in thinner intervals (Table 11). Lithofacies C is sandstone comprising of medium shale laminae (Figure 5). When the shale laminae are thick enough for the tool to detect them, the neutron-density separation shifts from negative to positive. In lithofacies H no trend is observed in the gamma ray or the neutron-density separation, probably

due to the sorting of these intervals. In lithofacies F the neutron and density logs are commonly observed overlapping with a lower transit time correlated with the other lithofacies (Table 11).

Table 11 – Synthetic type log displaying the relationship between lithofacies and well log response in well 7220/8-1 and well 7220/7-1 (Lithofacies J is excluded because it was only observed in an interval of 10 cm in well 7220/7-1). GR – gamma ray, NEU – neutron log and DEN – density log. AC – sonic log.



### 6.3 Porosity model

Porosity models constructed from the density log only underestimates the porosity by 0.6 %-point (absolute) and 0.4 %-point (absolute) (Table 12). The porosity model calculated from the sonic log instead gives an overestimation of the porosity of 3.7 %-point (absolute). The empirical combined porosity model using both sonic and density logs as input results matches with the core corrected porosity values obtained from routine core analysis. It overestimates the porosity with only 0.018 %-point (absolute). Thus, it is considered as the most unbiased model.

Table 12 – Results for the four generated porosity models where both the density log derived, and sonic log derived porosity were calculated (For the corresponding histogram, where porosity from core plugs is subtracted from the resultant porosity model. The x-axis is the difference between the two. A distribution skewed to/with a mean on the negative side indicates that the model underestimates porosity and oppositely. The y-axis is the fraction of the model representing each x value. To the right side the cumulative fraction is listed for the black line in the histogram. Combination of the two (sonic and density) displayed the best results.

	Histogram of core porosity subtracted from porosity model	Statistics	Description
Porosity model for density log		Minimum Values -0.24929 Maximum Values 0.23093 Range 0.48022 Mean -0.00638 Variance 0.00214 Standard Deviation 0.04627 Median -0.00368 Mode -0.00400	Filter with VSH less than 50% and PORC > 10 % Mean grain density: 2.66 Fluid density in oil zone: 0.883 g/cc Fluid density in water zone: 1.08 g/cc  The model displays slightly underestimation of porosity with a mean of 0.6 %
Porosity model for density log (Different parameters for each facies)		Minimum Values -0.24929 Maximum Values 0.23809 Range 0.48022 Mean -0.00413 Variance 0.00219 Standard Deviation 0.04681 Median -0.0013 Mode 0.00400	Grain density based on mean for each facies. Fluid density in oil zone: 1.08 g/cc Fluid density in water zone: 1.08 g/cc  The model displays a slightly underestimation of porosity with a mean of -0.4 %
Porosity model for sonic log		Minimum Values -0.18660 Maximum Values 0.19883 Range 0.38544 Mean 0.03736 Variance 0.00251 Standard Deviation 0.05006 Median 0.00340 Mode 0.00440	Interval transit time of matrix ( $\Delta t_{ms}$ ): 54 $\mu$ s/ft Interval transit time for fluid ( $\Delta t_f$ ): 189 $\mu$ s/ft  Resultant model displays overestimation of porosity with a mean of 3.7 %
Porosity model for sonic- & density log		Minimum Values -0.22592 Maximum Values 0.22611 Range 0.45203 Mean 0.00018 Variance 0.00190 Standard Deviation 0.04360 Median 0.00300 Mode 0.00400	Porosity from density log combined with porosity from sonic log weighted 85 % and 15 % respectively.  Resultant model displays a slightly overestimation of porosity with a mean of 0.018 %

Well 7222/7-1 Well 7222/8-1

#### 6.4 Thomas and Stieber (1975)

Clean sand points in well 7220/8-1 was set to a porosity of 28.5 % and gamma ray of 15 API and 34 % porosity and gamma ray of 17.4 API in Nordmela zone 2 and 3 respectively (Table 13). The shale end point was defined by point 9 in Figure 23, with a porosity of 14.6 % and a gamma ray of 120 API. Based on similar well logs response, this point was assigned lithofacies I as found in well 7220/7-1. Furthermore, the shale resistivity in 7220/8-1 was 5.65  $\Omega$ m. In well 7220/7-1 the clean sandstone end point was set to 27 % and a gamma ray of 29 API. Furthermore, the laminated shale end point was set to a porosity and gamma ray of 8 % and 134 API respectively. The resistivity of pure shale in this well was 24.54  $\Omega$ m (Table 13). Hence, the conductivity of shale from resistivity logs are lower in well 7220/7-1 correlated with well 7220/8-1.

Table 13 – The resultant endpoints for clean sandstone and clean laminated shale

Well	Gamma ray Clean sandstone [GAPI]	Porosity of clean sandstone [fr.b.v]	Gamma ray laminated shale [GAPI]	Porosity of laminated shale [fr.b.v]	Resistivity of 100% laminated [ $\Omega$ m]
7220/8-1	15	0.34	120	0.146	5.65
7220/7-1	29	0.27	134	0.08	24.54

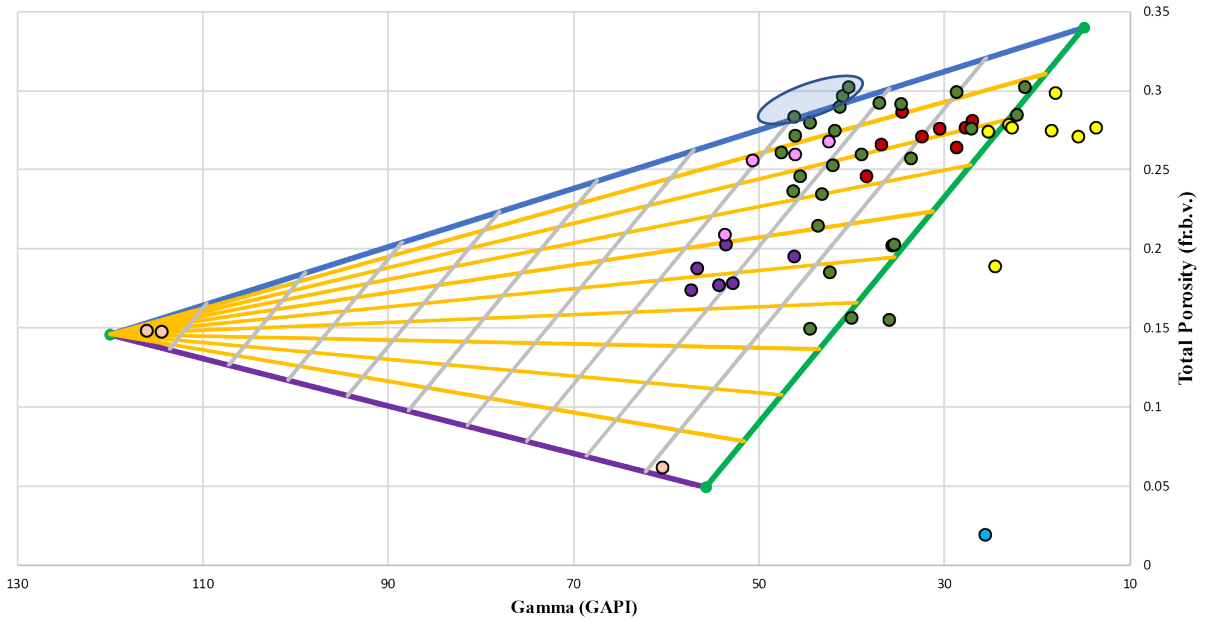
##### 6.4.1 Well 7220/8-1 Skrugard

The graphical results after Thomas and Stieber (1975) reveal some trends related to the different lithofacies observed in the core (Figure 23). The yellow and red points corresponding to lithofacies A (yellow) and B (red) respectively (observed as the “cleanest” sandstone from core interpretations) are mainly plotted towards the “clean” sandstone endpoint. Lithofacies C, which is from core observations a mixture between sand and shale laminae are plotted in a large area of the envelope. Nevertheless, the points are more towards the “clean” sandstone endpoint correlated with lithofacies D and I. Lithofacies E is plotted in the intermediate range in the envelope. Furthermore, lithofacies D (purple) and I (beige), respectively heterolithic sandstone and shale and mudstone are plotted toward the more laminated shale end point. Lithofacies F (one turquoise point in Figure 23, A) and the red circle in Figure 23, B) is plotted outside the envelope. From core data and lithofacies interpretations these intervals are calcite cemented sandstone resulting in low porosity values and gamma ray. The point which plotted slightly above the laminated shale line (blue shaded circles in Figure 23, A and B) were projected down to the line.

A)

Thomas og Stieber (1975)

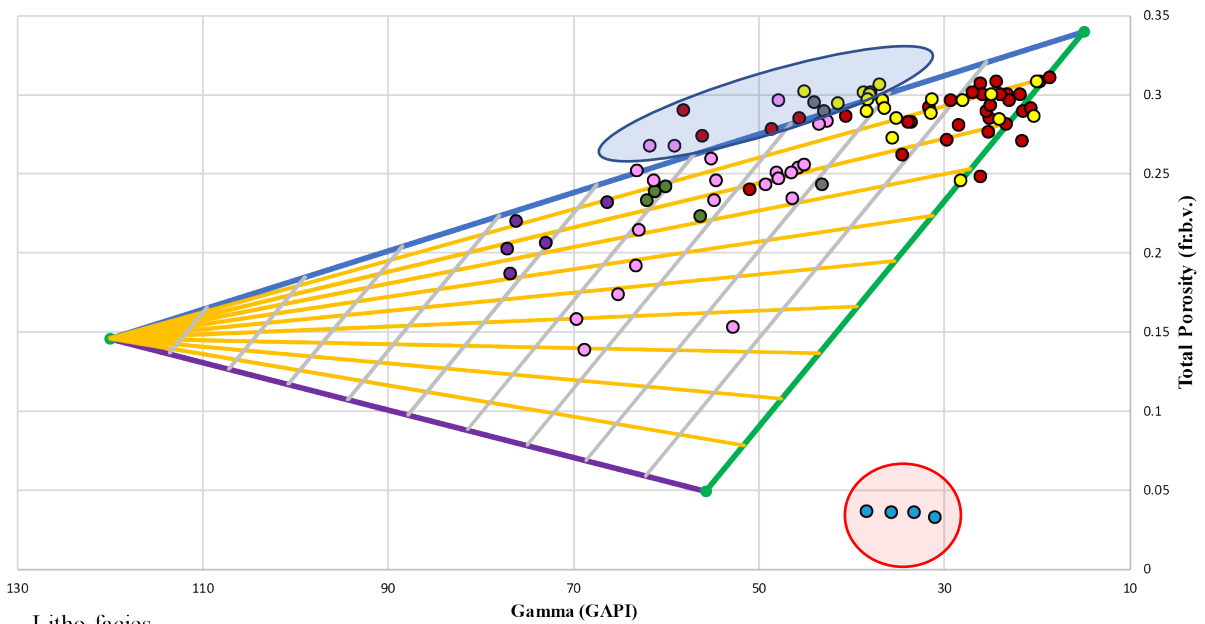
7220/8-1 - Nordmela 3



B)

Thomas og Stieber (1975)

7220/8-1 - Nordmela 2



Litho-facies  
 ● A ● B ● C ● D ● E ● F ● I ● Undefined

Figure 23 – Cross-plot after Thomas and Stieber (1975) from well 72208-1: A) Nordmela Formation zone 3 and B) Nordmela Formation zone 2. The blue shaded circles corresponding to points plotted above the laminated shale line and the red shaded circles in Figure 23, B corresponding to calcite cemented sandstone and lithofacies F.

The results after Thomas and Stieber calculation in well 7220/8-1 with correlation to core interpretation is displayed in Figure 24: (a) In the interval from 1360.2 m to 1360.5 m measured depth, clean sandstone with no shale lamination and lithofacies A is observed in the core. The calculation reveals a net sand of 100 % (no laminated shale). The porosity of the net sand fraction is 28 % where the relative (percentage, fraction) dispersed shale is calculated to be approximately 25 % (Figure 24, a); (b) Lithofacies C is observed in the interval from 1368.7 m to 1369.0 m measured depth. The laminated shale is calculated to be 19 %. The total porosity of the 81 % net sand fraction is 27 % with 24 % relative (percentage, fraction) dispersed shale (Figure 24, b); (c) The interval from 1381.1 to 1381.4 m measured depth is interpreted to be lithofacies B. The net sand fraction is calculated to be 100 % (no laminated shale) with a total porosity of 31 %. The relative (percentage, fraction) disperse shale content is calculated to be 10 % (Figure 24, c); (d) Lithofacies F is observed from 1386.1 to 1386.4 m measured depth. This interval plots outside the envelope to the right, with low porosity and low gamma ray (Red circle in Figure 23, B). Hence, the calculation is not valid. Nevertheless, the position of the points indicate calcite cemented sandstone and a non-net interval (Figure 24, d); (e) From 1391.4 m to 1991.7 m measured depth lithofacies D is observed. The calculations after Thomas and Stieber (1975) reveals laminated shale of 47 % where the 53 % resultant net sand have a total porosity of 22.6 % because of 40 % (percentage, fraction) dispersed shale (Figure 24, e); (f) From 1396.1 m to 1396.4 m measured depth, the core interpretation reviles lithofacies E. The total porosity of the net sand is calculated to be 23 % where 39 % of the pore space consist of dispersed shale. The laminated shale is 44 % (Figure 24, f); and (g) From measured depth 1402.1 m to 1402.4 m medium grained sandstone defined as lithofacies A is observed. The rock has a calculated laminated shale of 20 %. The net sand has a total porosity of 33 % because of 3 % (percentage, fraction) dispersed shale.

# Well 7220/8-1

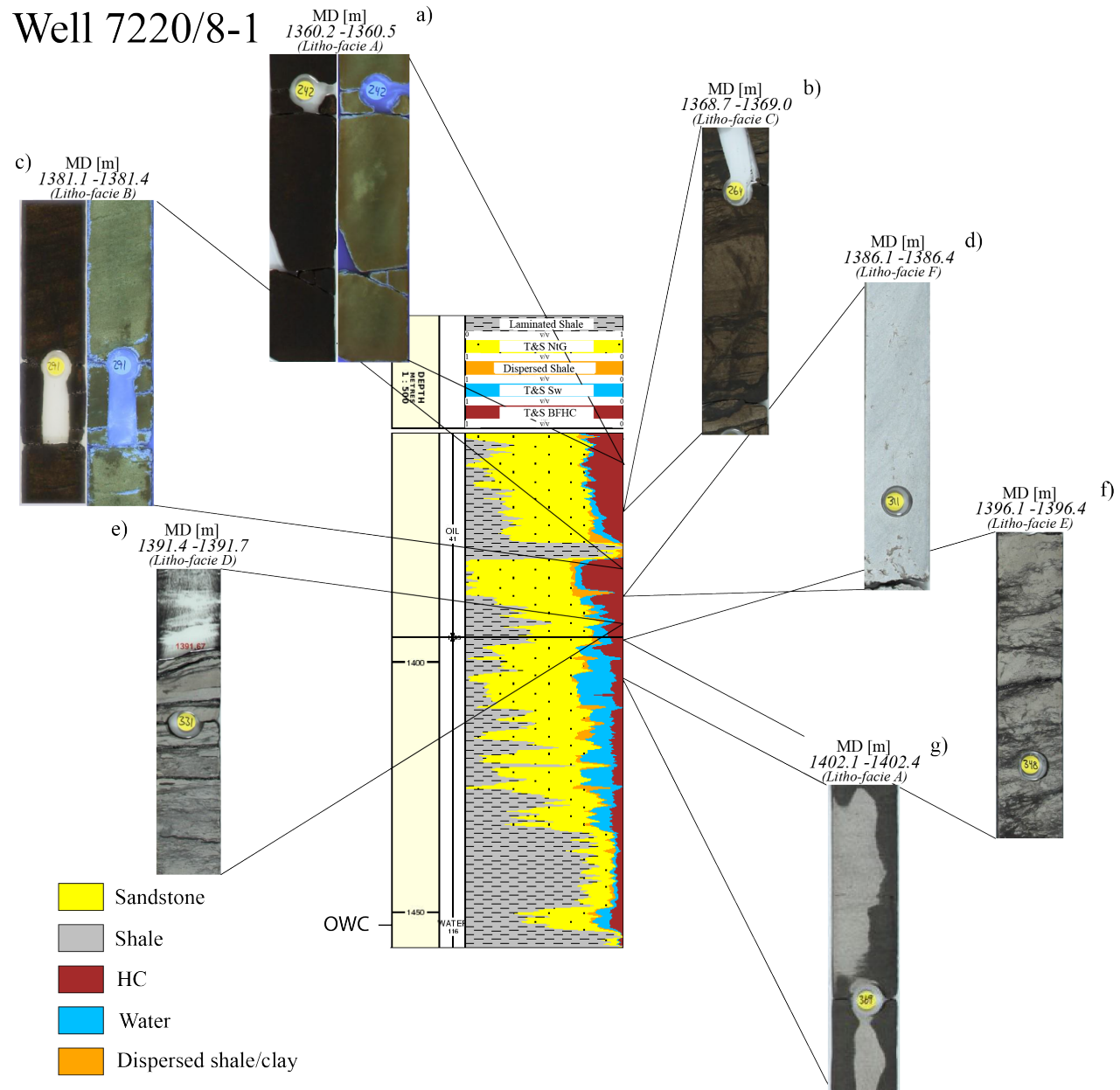


Figure 24 – Calculation of net sand, dispersed shale and laminated shale after Thomas and Stieber (1975) in well 7220/8-1 (Skrugard). The results are correlated with core observations and photos in seven intervals: a) Lithofacie A; b) Lithofacie C; c) Lithofacies B; d) Lithofacies F; e) Lith-facies D; f) Lithofacies E; and g) Lithofacies A. Due to high oil saturation in points a) and c) the ultraviolet images is added to the right of the core photos to better display the rocks.

#### 6.4.2 Well 7220/7-1 Havis

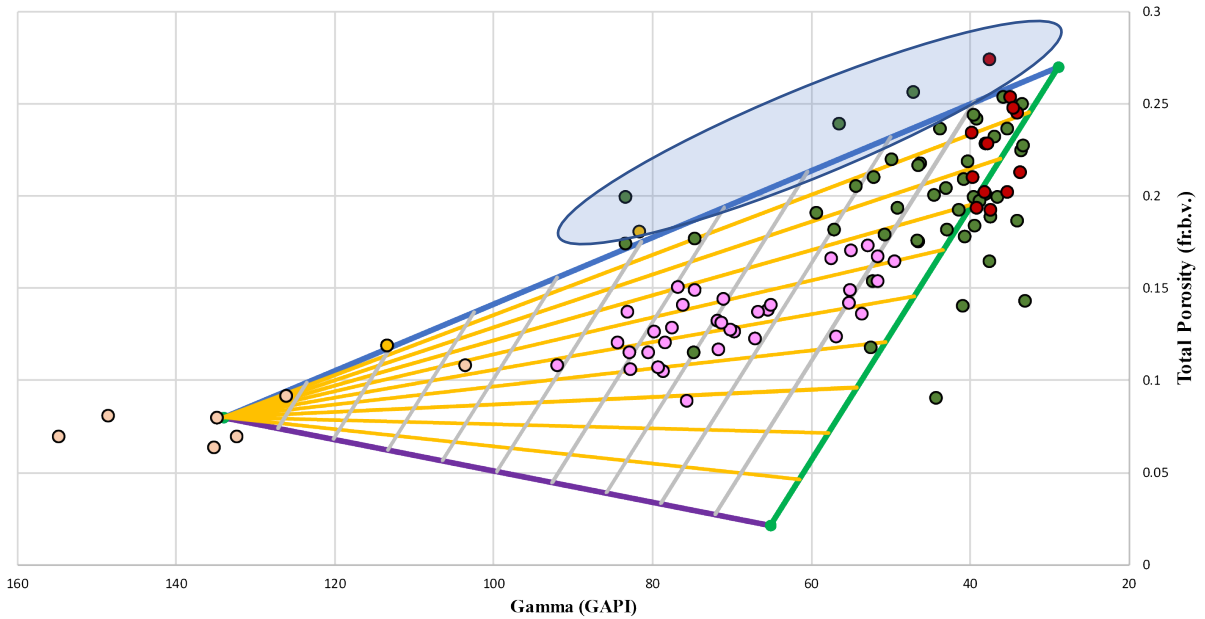
The graphical representations of the gamma ray versus total porosity from well 7220/7-1 reveals a large variety in lithology due to the spreading of the points (Figure 25). Assigning the lithofacies from the core observations some clear trends can be identified. Lithofacies A and B are plots more towards the “clean” sandstone endpoint correlated with the other lithofacies. Lithofacies C is commonly plotted between lithofacies E and B from approximately 5 % to 50 % laminated shale. Lithofacies E is commonly plotted in the intermediate range of the envelope but with higher gamma ray and porosity correlated to lithofacies D and I. Lithofacies I consist of almost 100 % laminated shale and a high peak in the gamma ray is observed in this interval. The poorly sorted sandstone intervals, lithofacies H (orange), has no clear trend in where it is plotted in the envelope. Sometimes the lithofacies is plotted almost toward the clean sandstone end-point or with some dispersed shale (Figure 25, B) and alternatively it is plotted toward 70 to 80 % laminated shale (Figure 25, A). Some of the points corresponding to lithofacies A, are plotted to the right of the dispersed shale line (yellow shaded circle in Figure 25, B). From lithology description the points contain some calcite, which may result in lower gamma ray, therefore these points were projected to the dispersed shale line. Lithofacies F (turquoise) is commonly plotted outside the envelope with low porosities and permeabilities and therefore the calculations after Thomas and Stieber (1975) are not valid for these intervals (red shaded circle Figure 25, B). In addition, some of the points plots above the laminated shale line but they are included in the calculations by being projected down to the laminated shale line (blue shaded circles Figure 25, A and B).



A)

Thomas og Stieber (1975)

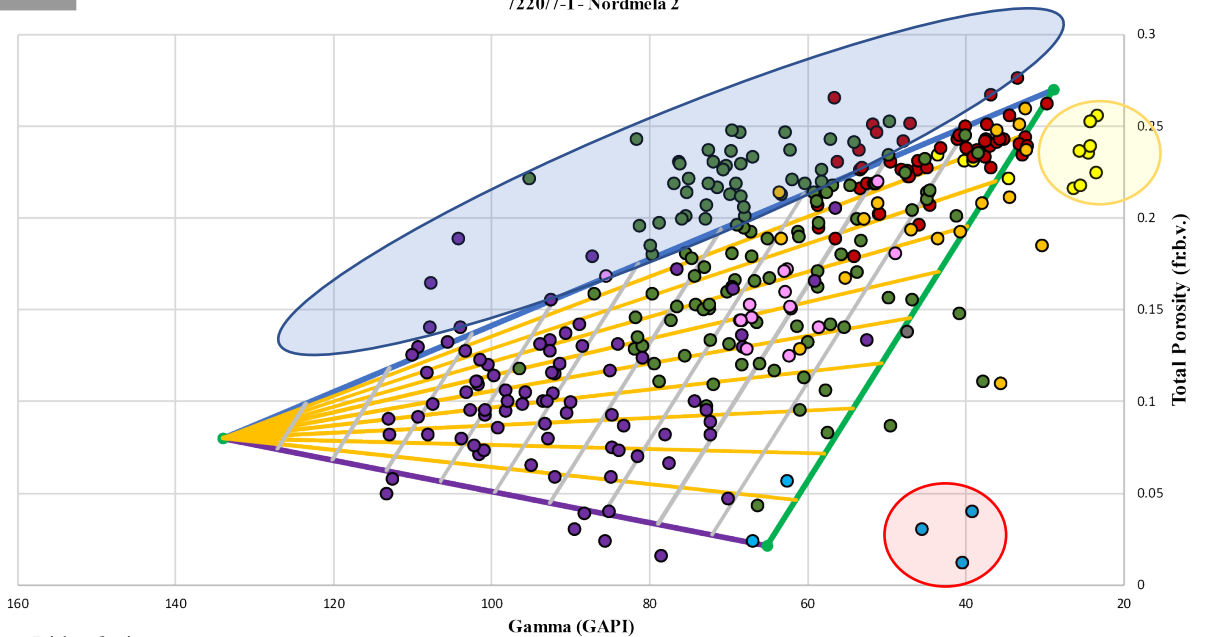
7220/7-1 - Nordmela 3



B)

Thomas og Stieber (1975)

7220/7-1 - Nordmela 2



Litho-facies

- A
- B
- C
- D
- E
- F
- H
- I
- J

Figure 25 – Cross-plot after Thomas and Stieber (1975) from well 7220/7-1: A) Nordmela Formation zone 3 and B) Nordmela Formation zone 2. The blue shaded circles corresponding to points plotted above the laminated shale line and the red shaded circles in Figure 23, B corresponding to several points interpreted as calcite cemented sandstone, lithofacies F. The yellow shaded circle contains several points from lithofacies A, where some calcite is observed in the core description from routine core analysis.

The results after Thomas and Stieber (1975) calculation in well 7220/7-1 with correlation to core interpretation is displayed in Figure 26: (a) The core from 1859.8 m to 1860.1 m measured depth displays thin darker laminae which are interpreted to be possible shale laminae or alternation of color. Based on the thickness of possible shale laminae, this interval is classified as lithofacies A. The net sand fraction is 100 % in this interval meaning that there is no laminated shale. The porosity of the net sand is calculated to 19.2 % because of 32.1 % relative (percentage, fraction) dispersed shale (Figure 26, a); (b) The cored interval from 1884.9 to 1885.2 m measured depth consists of bioturbated sandstone and lithofacies E. Laminated shale from calculation is 62 %, resulting in a net sand of 38 %. The net sand has a total porosity of 14 % and the relative (percentage, fraction) dispersed shale is 51 % (Figure 26, b); (c) Thin alternating heterolithic sandstone and shale is observed in the interval from 1891.6 m to 1891.9 m measured depth, which is defined as lithofacies D. In this interval the laminated shale volume is calculated to be 68 %. The remaining net sand fraction has a total porosity of 20 % because of 29 % relative (percentage, fraction) dispersed shale (Figure 26, c); (d) Calcite cemented sandstone with a light to white color is observed from 1912.8 m to 1913.1 m measured depth. The method after Thomas and Stieber (1975) is not valid for this interval because the points are plotted outside (blue shaded circle in Figure 25, B) the envelope (Figure 26, d); (e) An interval with clean sandstone is observed from 1924.8 m to 1925.1 m measured depth. The interval is highly saturated with oil which makes the core dark to black in color. The ultraviolet light reveals residual oil as a yellow color. Also, this indicate that this interval is fairly clean regarding shale lamination. The calculation of net sand is 100 % (no laminated shale), with a total porosity of 27 %. The pore space is filled with 4 % (percentage, fraction) dispersed shale (Figure 26, e); (f) From 1934.8 m to 1935.1 m measured depth thicker shale laminae (> 1 cm) is alternating between sandstone intervals. Based on the thickness of the shale laminae, this interval is referred to as lithofacies C. The net sand is calculated to be 60 %, meaning 40 % shale lamination. The resulting total porosity due to 10 % relative (percentage, fraction) dispersed shale is 25 % (Figure 26, f); and (g) Below the oil-water contact, heterolithic sandstone with alternating shale laminae is observed in the interval from 1953.9 m to 1954.2 m measured depth. The core description from routine core analysis reveals that the sandstone grains are very fine grained with sub-angular sphericity and classified as lithofacie D. The calculation reveals 53 % laminated shale. The net sand has a porosity of 14 % where the relative dispersed shale (percentage, fraction) is calculated to be 52 % (Figure 26, g).

# Well 7220/7-1

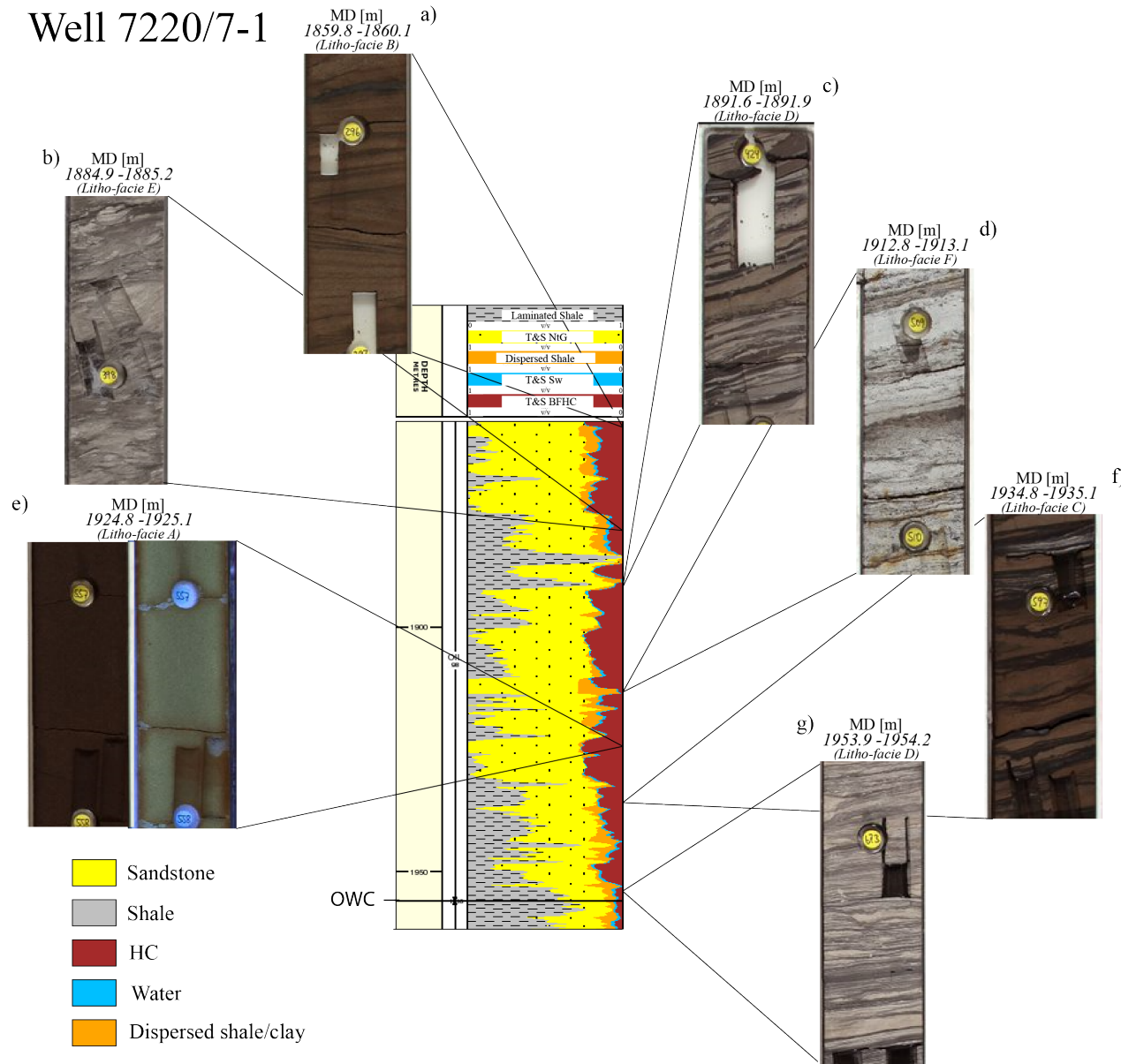


Figure 26 – Calculation of net sand, dispersed shale and laminated shale after Thomas and Stieber (1975) in well 7220/7-1 (Havis). The results are correlated with core observations and photos in seven intervals: a) Lithofacies B; b) Lithofacies E; c) Lithofacies D; d) Lithofacies F; e) Lithofacies A; f) Lithofacies C; and g) Lithofacies D. Due to high oil saturation in point e) the ultraviolet image is added to the right of the core photo to better display the rock.

## 6.5 Permeability model

Two clear trends (one for each well) were observed by plotting the core corrected porosities and permeabilities in a cross-plot (Figure 27). The overall porosities in well 7220/8-1 (purple) were higher than in well 7220/7-1 (orange). Well 7220/7-1 also had higher abundance of core measurement permeability values below 15 mD compared to well 7220/8-1 (Figure 27). Based on the difference in the two wells, one regression line for each well was constructed and used as an input for the permeability model (dotted black line for well 7220/7-1 and black line for well 7200/8-1, (Figure 27).

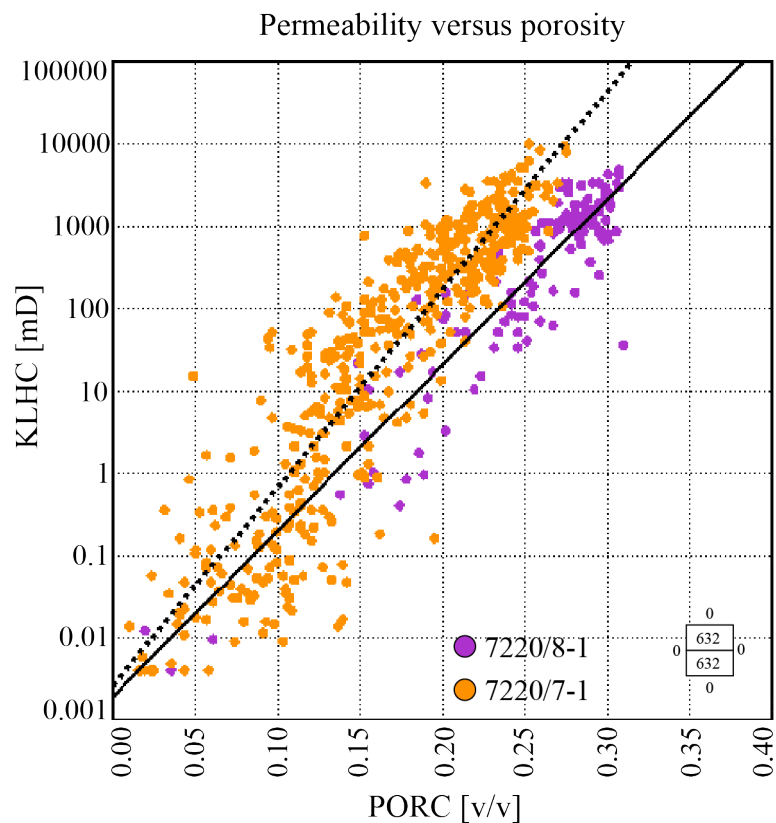


Figure 27 – Linear relation between the logarithm of permeability and total porosity where. Permeability (KLHC) and porosity (PORC) from core corrected routine core analyses measurements in wells 7220/8-1 (purple) and 7220/7-1 (orange). The resultant regression lines for the wells is displayed as a black line and a black dotted line respectively.

The total porosity versus per permeability cross-plot colored after volume of shale confirmed that there was permeability trend related to shale distribution (Figure 28). It also could be observed that the volume of laminated shale after Thomas and Stieber (1975) displayed a clearer trend than for example volume of shale from neutron-density separation (blue, turquoise and orange polygons, Figure 28).

### Permeability versus porosity

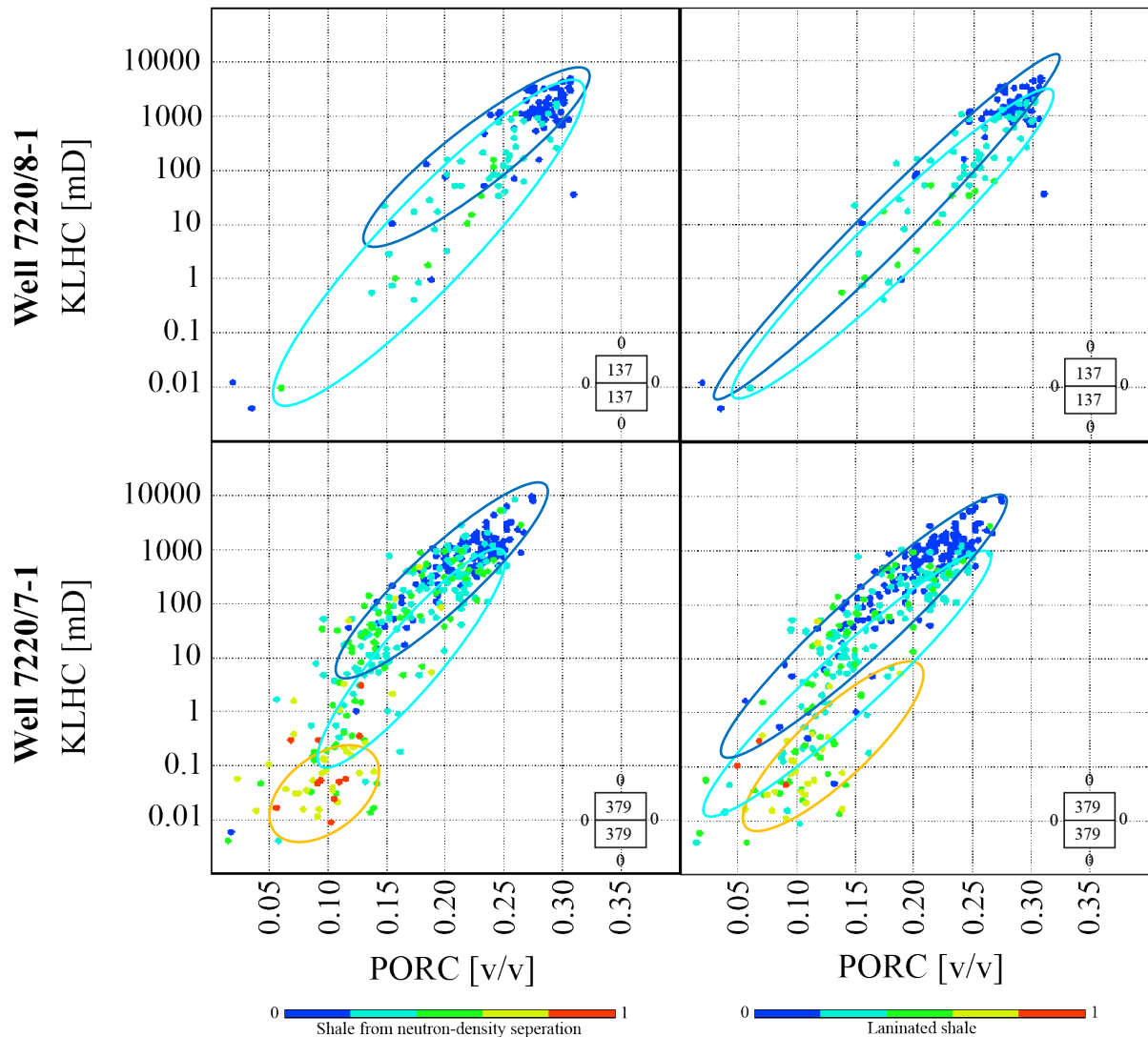


Figure 28 – Core corrected horizontal permeability (KLHC) versus Core corrected total porosity (PORC) plots from wells 7220/8-1 and 7220/7-1. The data points are colored according to shale volume obtained from neutron-density separation and laminated shale after Thomas and Stieber (1975). The blue, turquoise and orange polygons are marking the trends observed in the cross-plots with two obvious trends in well 7220/8-1 and three trends in well 7220/7-1 (Calcite cemented intervals are excluded and only Nordmela zone 2 and 3 are included in these cross-plots).

The coefficient of correlation for the simple linear regression and multivariate linear regression in well 7220/8-1 are 0.92 and between 0.93 to 0.94 respectively when the total porosity from corrected core measurements are used as independent variable (Appendix 7). When total log porosity is used as independent variable the coefficient of correlation for all (simple linear and multivariate linear) regressions equal to 0.76 (Appendix 8). The highest coefficient of correlation of 0.94 is obtained from the multivariate linear regression using the volume of shale obtained after Thomas and Stieber (1975) as inputs.

In well 7220/7-1 the coefficient of correlation for the simple linear regression and multivariate linear regressions are 0.90 and 0.92 respectively (Appendix 9) when corrected total porosity measurements from routine core analysis are used as independent variable. When the calculated porosity log is used instead of porosity from core measurements the difference in coefficient of correlation is larger. The simple regression has a coefficient of correlation of 0.76. For the multivariate linear regressions, the coefficient of correlations are 0.76, 0.79 and 0.79 for volume of shale from neutron-density separation, dispersed and laminated shale after Thomas and Stieber (1975) and laminated shale after Thomas and Stieber respectively (Appendix 10).

From the correlation between the calculated horizontal permeability curves with the corrected horizontal permeability measurements both for well 7220/8-1 (Figure 29) and well 7220/7-1 (Figure 30) there is a small improvement for the horizontal permeability curves from the multivariate linear regression from neutron-density separation correlated with the permeability curve obtained from simple linear regression. The larger improvement was observed for the multivariate linear regressions using volume of shale from the method after Thomas and Stieber (1975) as input. Where a slightly improvement is observed from using both the laminated and dispersed volume of shale obtained as input (green area, (Figure 29)).

Correlating the permeability models using volume of shale obtained after Thomas and Stieber (1975) and the measured core corrected permeabilities it was observed that the models did not have a good match in some parts of the well, especially in litho-facies C (green marked area with core to the left Figure 30). It could also be observed that in some intervals the sampled core plugs were taken in between the shale laminae (green marked area with core to the left Figure 30). Hence the permeability measurements were representing the sandstone laminae and not the whole interval. In other intervals the core plugs were taken such that it represented more the true variation of the core (blue marked area with core to the right, Figure 30)

## Permeability models for well 7220/8-1

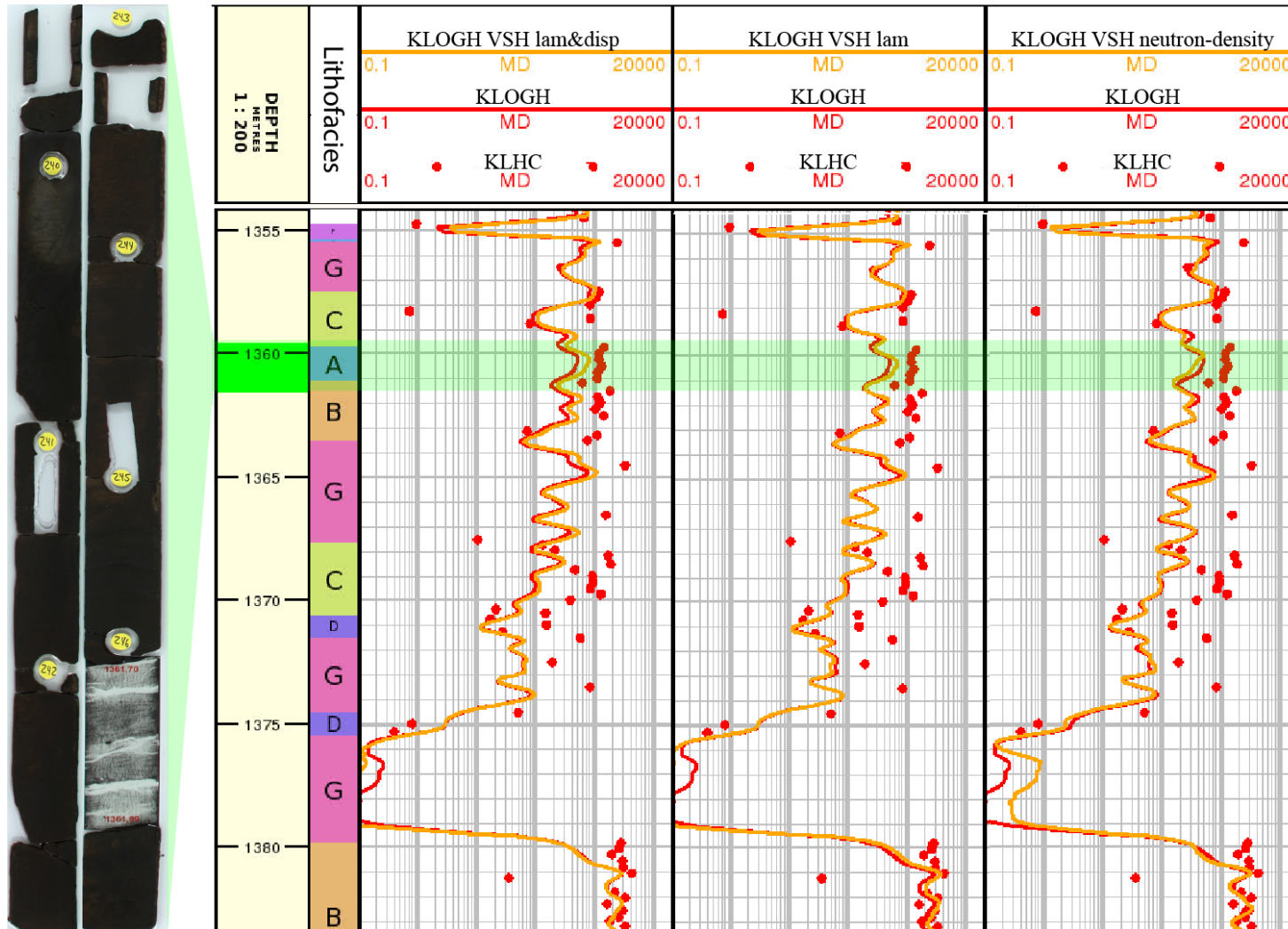


Figure 29 – Resultant permeability models for well 7220/8-1. Corrected horizontal core permeabilities (KLHC) and horizontal absolute permeability curve (KLOGH), correlated with the three multivariate regressions using porosity and three different volume of shale calculation as dependent variables: (1) Volume of shale (laminated and dispersed) calculated after Thomas and Stieber (1975) – KLOGH VSH lam&disp (2) Volume of laminated shale after Thomas and Stieber (1975) – KLOGH VSH lam; and (3) Volume of shale calculated from neutron-density separation – KLOGH VSH neutron-density. The green area marks one of the relatively good improvement for the multivariate regressions using shale obtained from gamma ray log and shale obtained from Thomas and Stieber (1975) as input. The corresponding core is displayed to the left and is resulting to lithofacies A to a transition to lithofacies B. The dark color is due to the high saturation of oil.

## Permeability models for well 7220/7-1

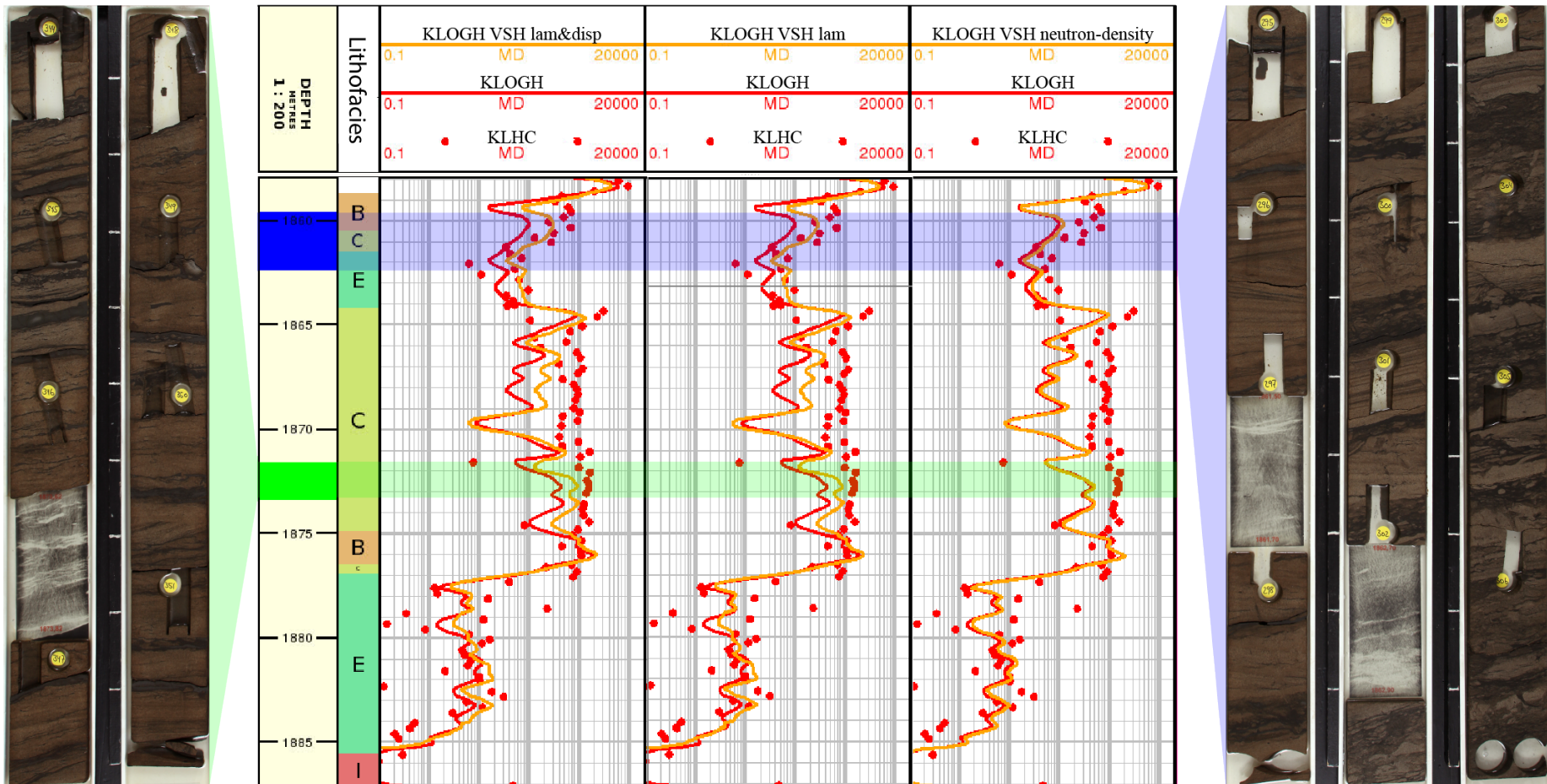


Figure 30 – Resultant permeability models for well 7220/7-1. Corrected horizontal core permeabilities (KLHC) and horizontal absolute permeability curve (KLOGH), correlated with the three multivariate regressions using porosity and three different volume of shale calculation as dependent variables: (1) Volume of shale (laminated and dispersed) calculated after Thomas and Stieber (1975) – KLOGH VSH lam&disp (2) Volume of laminated shale after Thomas and Stieber (1975) – KLOGH VSH lam (3) Volume of shale calculated from neutron-density separation – KLOGH VSH neutron-density. The green and blue area marks two of the good improvement for the multivariate regressions using shale obtained from gamma ray log and shale obtained from Thomas and Stieber (1975) as input. The corresponding cores is displayed to the left (green) and is resulting to lithofacies C and right (blue) corresponding to lithofacies B, C and E.



## 6.6 Water saturation model

Results for the corrected resistivity from water samples of well 7220/7-1 is  $0.031 \Omega\text{m}$  (Table 14) and for well 7220/8-1 is estimated to be  $0.041 \Omega\text{m}$ .

Table 14 – Resistivity of water obtained from water sample in well 7220/7-1 and from depth versus pressure trend for well 7220/8-1 (measurements at standard condition (SC) versus reservoir condition (RC)).

Well	Depth	Resisitvity (SC)	Resisitvity (RC)	Density (SC)	Density (RC)
7220/7-1	2063 mRKB	$0.06 \Omega\text{m}$	$0.031 \Omega\text{m}$	$1.1024 \text{ g/cc}$	$1.08 \text{ g/cc}$
7220/8-1	1420 mTVD	-	$\sim 0.041 \Omega\text{m}$	-	$\sim 1.12 \text{ g/cc}$

### 6.6.1 Archie (1942) and Waxman and Smits (1968)

Resultant Archie (1942) parameters ( $m$  and  $n$ ) and the clay corrected parameters ( $m^*$  and  $n^*$ ) for Waxman and Smits (1968) are listed in Table 15.

Table 15 – Resultant Archie (1942) and Waxman and Smits (1968) parameters obtained from special core analysis data ( $m$ ,  $n$ ,  $m^*$  and  $n^*$ ). The resistivity of the water ( $R_w$ ) is obtained from the fluid sample in well 7220/7-1 and from fluid density in well 7220/8-1.

Well	$m$	$n$	$m^*$	$n^*$	$R_w [\Omega\text{m}]$
7220/8-1	1.72	2.06	1.73	2.10	0.041
7200/7-1	1.81	1.97	1.84	2.09	0.031

Correlating the  $BQ_v$  with the dispersed and laminated shale in wells 7220/8-1 (Table 16) and 7220/7-1 Table 17 revealed that  $BQ_v$  varies from  $0.148 \Omega\text{m}^{-1}$  to  $0.424 \Omega\text{m}^{-1}$  in well 7220/8-1 where the four measurement are taken from relatively clean sandstone intervals (Table 16). One sample is taken in the bioturbated lithofacies E at 1401.68 m measured depth which has the highest  $BQ_v$  value (0.424). In well 7220/7-1 five measurements are available where the  $BQ_v$  ranges from  $0.391 \Omega\text{m}^{-1}$  to  $1.071 \Omega\text{m}^{-1}$  (Table 17). These special core analysis plugs are manly taken in more shalier intervals (lithofacies) correlated with well 7220/8-1. In well 7220/8-1 the dispersed shale varies from 0 to 0.24 fraction by pore volume where the dispersed shale 7220/7-1 varies from 0 to 0.42 fractions by pore volume. Overall the shale fractions and the cation exchange capacity of the shale is higher in well 7220/7-1 then well 7220/8-1.

Table 16 – BQ<sub>v</sub> measurements from special core analyses correlated with shale distribution obtained after Thomas and Stieber (1975) and lithofacies in well 7220/8-1 where: fr.b.v. – fraction by volume and fr.b.p.v – fraction by pore volume.

<b>Well 7220/8-1</b>				
Depth [m MD]	BQ <sub>v</sub> [1/Ωm]	Lam Shale [fr.b.v.]	Disp Shale [fr.b.p.v.]	Lithofacies
1359.19	0.148	0.029	0.243	C
1368.38	0.096	0.179	0.172	C
1387.67	0.085	0.214	0	A
1401.68	0.424	0.386	0.122	E

Table 17 – BQ<sub>v</sub> measurements from special core analyses correlated with shale distribution obtained after Thomas and Stieber (1975) and lithofacies in well 7220/7-1 where: fr.b.v. – fraction by volume and fr.b.p.v – fraction by pore volume.

<b>Well 7220/7-1</b>				
Depth [m MD]	BQ <sub>v</sub> [1/Ωm]	Lam Shale [fr.b.v.]	Disp Shale [fr.b.p.v.]	Lithofacies
1864.521	0.456	0.097	0.053	C
1881.57	1.071	0.257	0.420	E
1895.57	0.391	0.283	0.000	B
1903.57	0.539	0.165	0.000	B
1909.57	0.790	0.283	0.284	E

Based on average core plug measurements from the special core analysis, cation exchange capacity of the core measurements in well 7220/8-1 and well 7220/7-1 is approximately 0.03 meq/cm<sup>3</sup> and 0.06 meq/cm<sup>3</sup> respectively in the Nordmela Formation (Table 18). Furthermore the calculation from equation (22), showed that shale causes 3 % decrease in resistivity in well 7220/8-1 and 21 % decrease in resistivity in well 7220/7-1 .

Table 18 – Resultant cation exchange capacity of [Q<sub>v</sub>] of the core plugs in well 7220/8-1 and 7220/7-1 (BQ<sub>v</sub> is an average for all the available measurements from the Nordmela Formation in each well).

Well	Depth [m] MD RKB	T [°C]	R <sub>w</sub> [Ωm]	B [Ωm <sup>-1</sup> / meq.cm <sup>-3</sup> ]	BQ <sub>v</sub> [1/Ωm]	Q <sub>v</sub> [meq/cm <sup>3</sup> ]
7220/8-1	1380.5	39.1	0.041	6.8	0.2144	~ 0.03
7220/7-1	1971.0	61.6	0.031	10.7	0.6494	~ 0.06

There was observed little to no difference between the water saturation model obtained after Archie (1942) versus the model obtained after Waxman and Smits (1968), Figure 31. The more

shale rich interval in the wells (facies D and E) have little difference between the two saturation models. It was only in facies I which is a dense claystone package a change can be observed in well 7220/8-1 (red circle in Figure 31). But observing the water saturation from the Dean-Stark measurements in this area, they are closer to the method after Archie (1942) than that after Waxman and Smits (1968). In the lower part of the oil-zone of well 7220/7-1 the water saturation has a slight change within lithofacies D (orange circle, Figure 31) This corresponds to the most shaly interval from the core interpretation with 50 % shale lamina.

#### 6.6.2 Poupon and Leveaux (1971)

Comparing results from the two water saturation models proposed and tested by Poupon and Leveaux (1978), equation 25 has fairly similar water saturation in the water zone compared with equation 26. In the oil zone equation 25 has a higher oil saturation, hence higher bulk fraction hydrocarbon estimation correlated with equation 26 (red shaded areas, Figure 32). Therefore, the final water-saturation models for wells 7220/8-1 and 7220/7-1 was made using equation 25 as input for the volume of shale based water saturation model after Poupon and Leveaux (1971).

**Well 7220/8-1**

**Well 7220/7-1**

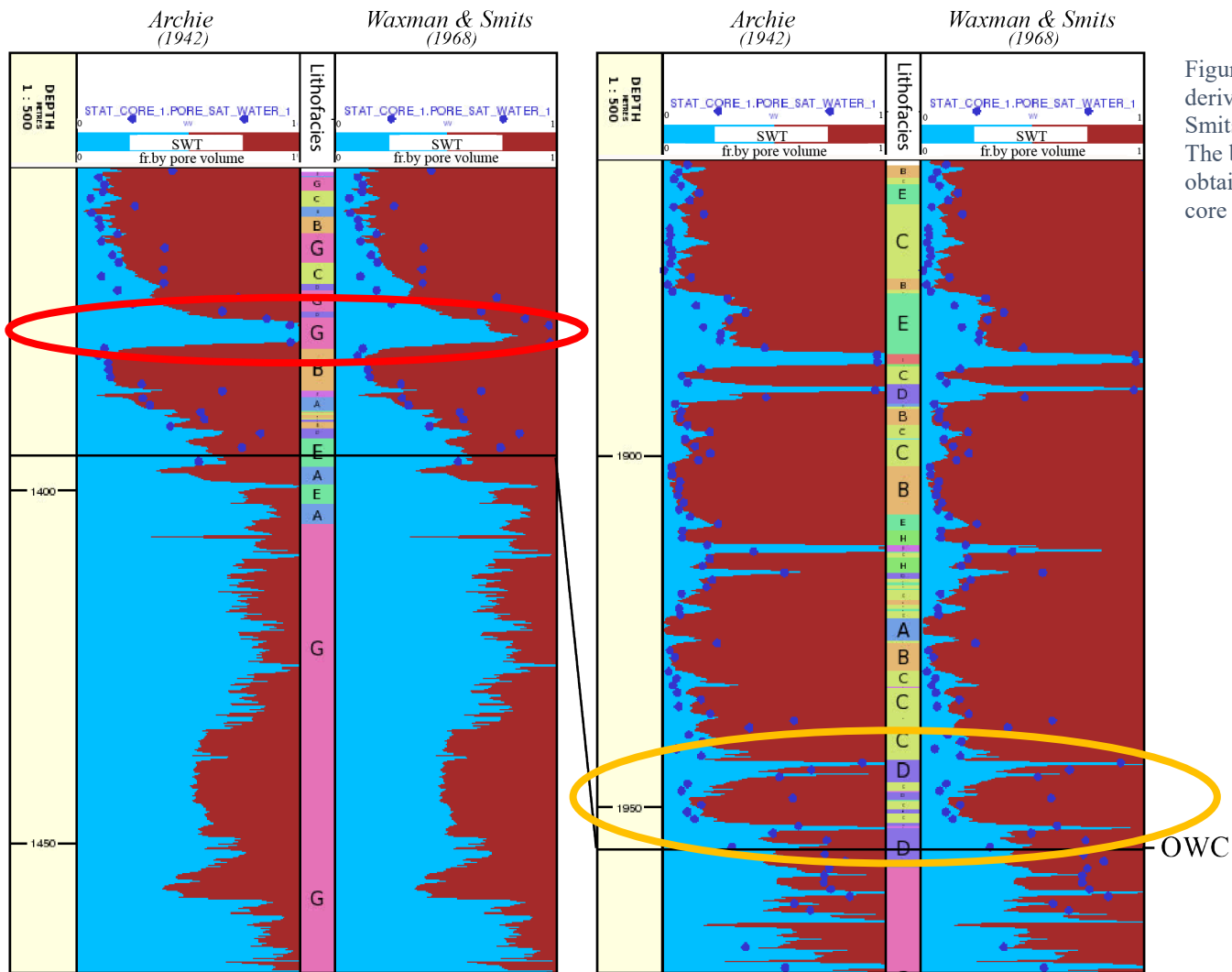


Figure 31 – Correlation between water saturation derived after Archie (1942) versus Waxman and Smits (1968) from wells 7220/8-1 and 7220/7-1. The blue dots are the water saturation measurements obtained from Dean-Stark extractions on the routine core analysis samples.

● Sw from Dean-Stark extraction

- Lithofacies**
- A
  - C
  - E
  - Undefined
  - B
  - D
  - I

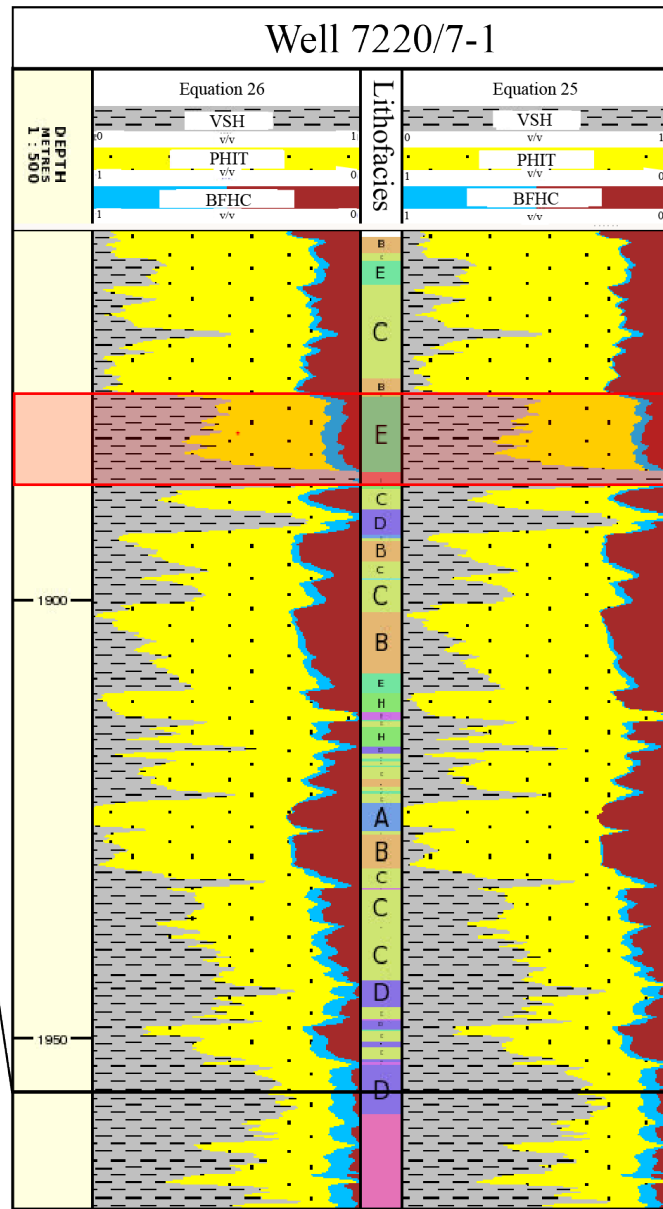
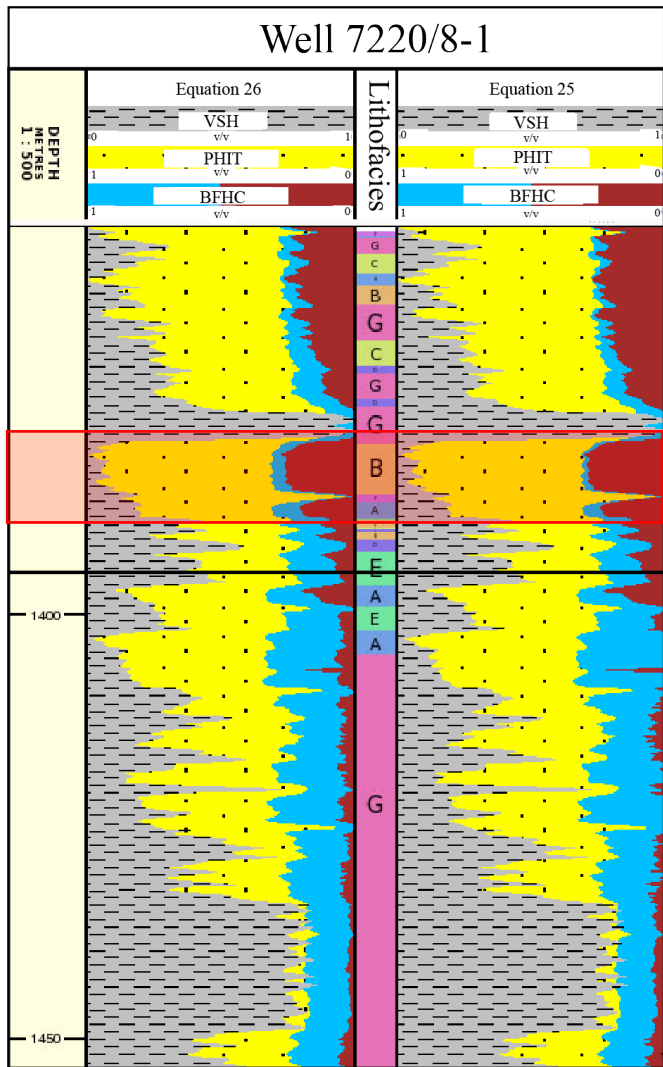
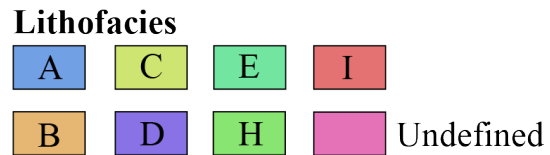


Figure 32 – Resultant bulk fraction hydrocarbon after Poupon and Leveaux (1971) using equations 25 and 26 in wells 7220/8-1 and 7220/7-1. The oil-water contact (OWC) is marked with a black line in the two wells



### 6.6.3 Klein and Martin (1997)

Higher shale resistivity values can be observed in well 7220/7-1 compared with well 7220/8-1 (Table 19). The difference in resistivity in the two wells, where the vertical shale resistivity is higher than the horizontal resistivity indicates that the shale in the Nordmela Formation is anisotropic.

Table 19 – The resultant horizontal and vertical resistivity of shale used as input in the modified Klein and Martin (1997) series resistivity model after Minh et al. (2007). In both wells the vertical resistivity are higher indicating shale anisotropy.

Well	$R_h$ [ $\Omega m$ ]	$R_v$ [ $\Omega m$ ]
7220/7-1	5.84	26.97
7220/8-1	4.14	12.35

### 6.6.4 Bulk fraction hydrocarbon results

From the series resistivity model after Klein and Martin (1997) and Thomas and Stieber (1975) a resulting net-to-gross of 0.76 and 0.75 respectively were generated based on net sand calculations (Table 20). Hence, these two methods are in good correspondence with similar net-to-gross calculations. Using Archie (1942) or Poupon and Leveaux (1971) as method no such relation is established. Therefore, these methods were modelled with and without cut-off, where the net-to-gross without cut-off is 1 and the one with cut-off is 0.87. The bulk fraction hydrocarbons in well 7220/8-1 varies from 0.149 to 0.177, whereas in well 7220/7-1 they vary from 0.032 to 0.149 (Table 20). The method of Klein and Martin (1997) gives overall lower estimations for the bulk fraction of hydrocarbon in both wells. These results indicate that the difference in bulk fraction hydrocarbon regarding the five different methods is not large.

Table 20 – Resultant net-to-gross (NtG) and bulk fraction hydrocarbon calculations from the different methods in wells 7220/8-1 and 7220/7-1

	<b>Well 7220/8-1</b> <i>1354-1395 m [MD]</i>		<b>Well 7220/7-1</b> <i>1858-1956 m [MD]</i>	
	<i>NtG</i>	<i>BFHC [fr.b.v]</i>	<i>NtG</i>	<i>BFHC [fr.b.v]</i>
<b>Archie</b> <i>Without cut-off</i>	1	0.172	1	0.149
<b>Archie</b> <i>With cut-off</i>	0.87	0.169	0.81	0.139
<b>Poupon &amp; Leveaux</b> <i>Without cut-off</i>	1	0.177	1	0.148
<b>Poupon &amp; Leveaux</b> <i>With cut-off</i>	0.87	0.176	0.81	0.139
<b>Thomas &amp; Stieber</b>	0.75	0.162	0.75	0.14
<b>Klein &amp; Martin</b>	0.76	0.149	0.76	0.132

The resultant models (with cut-off for Archie (1942) and Poupon and Leveaux (1971) are displayed in (Figure 33) for well 7220/8-1 and in (Figure 34) for 7220/7-1. Without cut-off values the methods after Archie (1942) and Poupon and Leveaux (1971) revealed high oil saturation also in the water zone. The five different approaches to calculate water saturation in the Nordmela Formation did not reveal significant differences. Nevertheless, the water saturation model with net-sand calculations after Klein and Martin (1997) resulted in water saturation in the water zone close to 1. In addition a fairly different volume of shale curve was obtained from the model after Klein and Martin (1997) than what were estimated using volume of shale calculations both from gamma ray log and neutron-density separation. Furthermore, the method after Thomas and Stieber (1975) revealed the difference between the shale types (gray as laminated shale and orange as dispersed shale in wells 7220/8-1 and 7220/7-1 (figures 33 and 34). An important reminder is that the dispersed shale situated inside the pores also contains (micro) porosity that is filled with water.

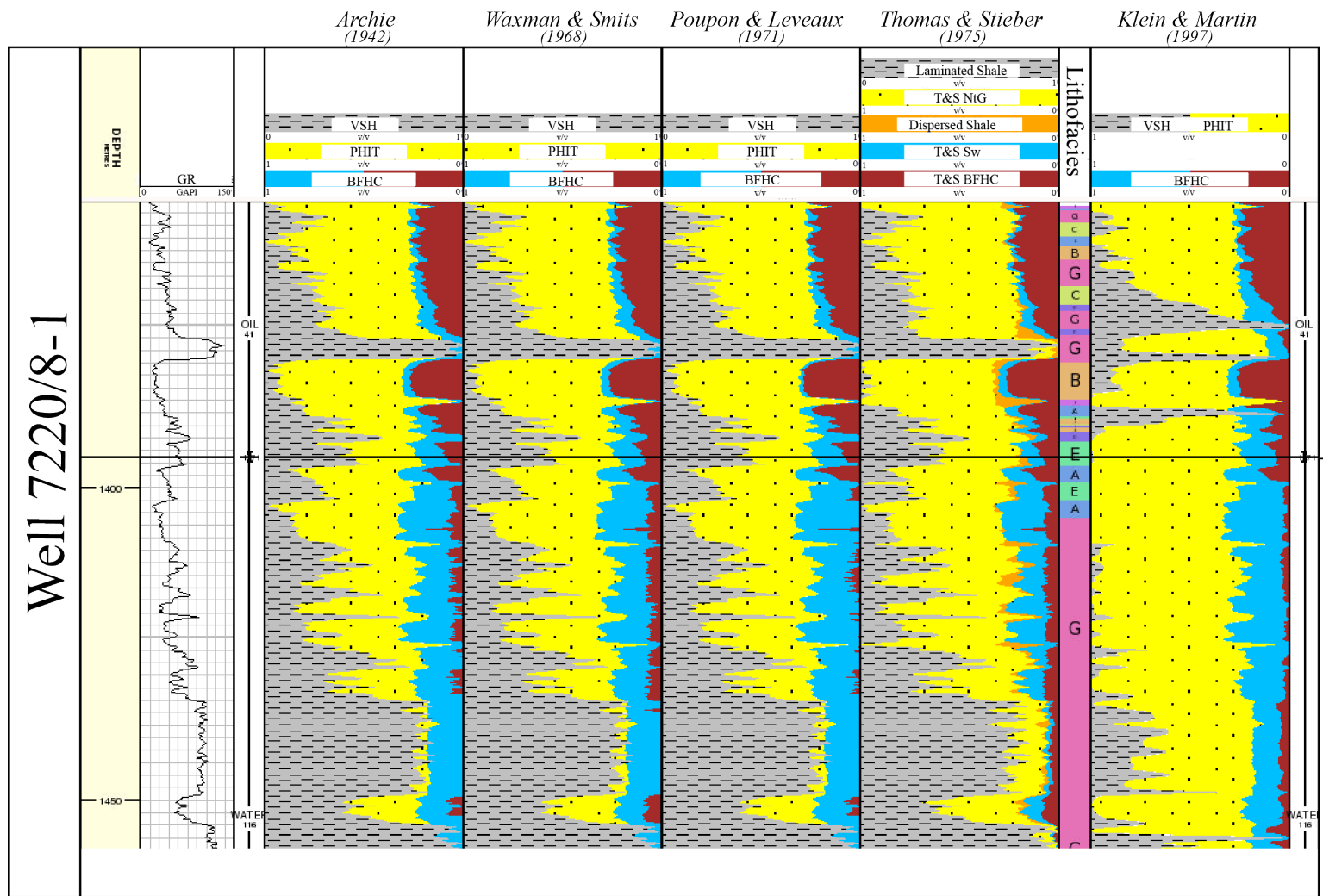
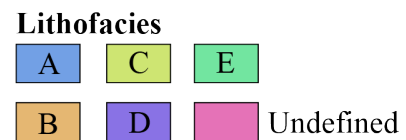
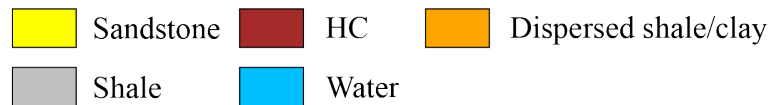


Figure 33 – Bulk fraction hydrocarbons obtained from five different models in well 7220/8-1. Only the method after Thomas and Stieber (1975) differentiate between laminated shale and dispersed shale (orange).





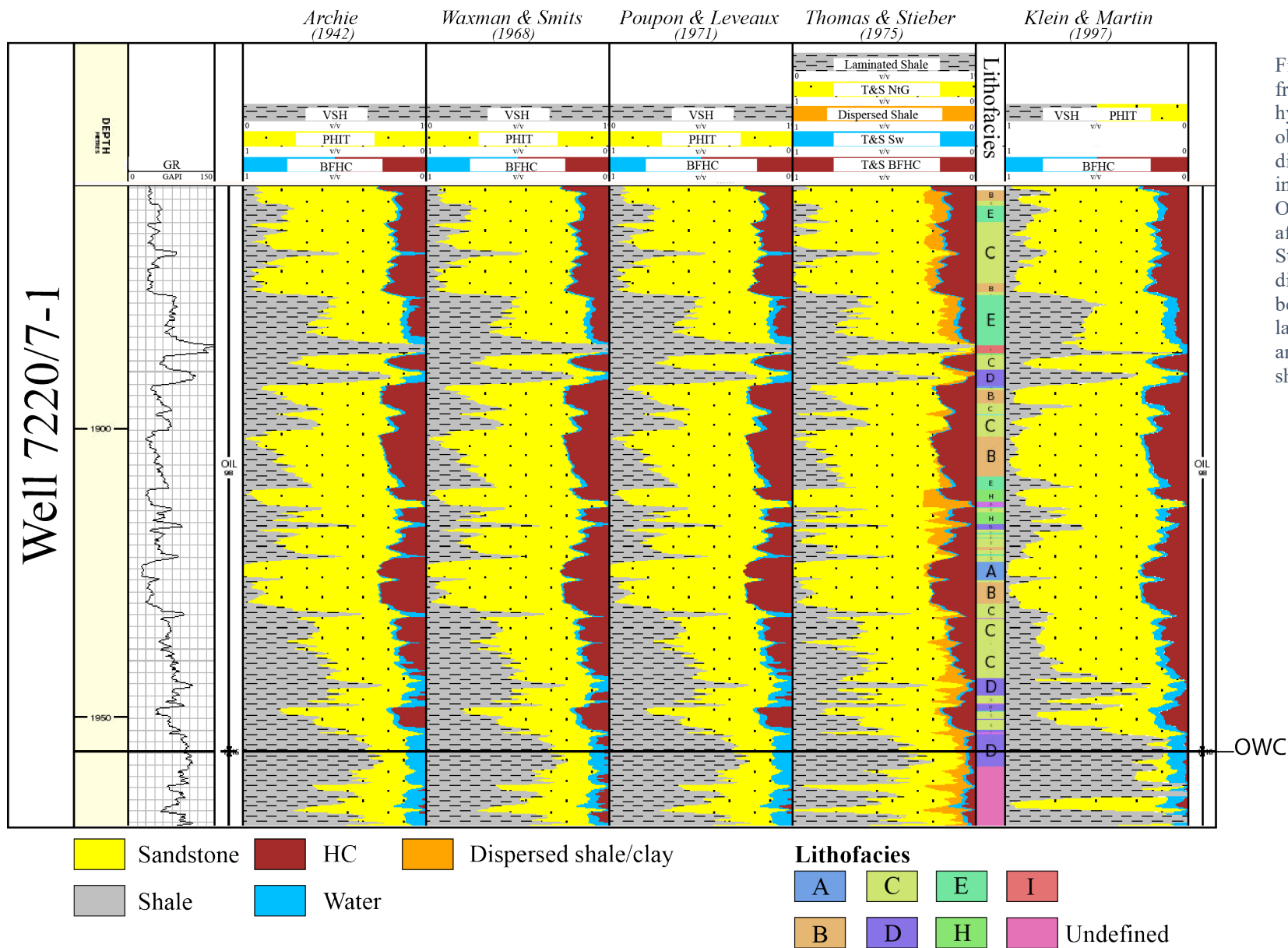


Figure 34 – Bulk fraction hydrocarbons obtained from five different models in well 7220/7-1. Only the method after Thomas and Stieber (1975) differentiate between laminated shale and dispersed shale (orange).

## 7 Interpretation and discussion

The study fails to divide the resultant lithofacies into distinct electrofacies. In order to be able to divide the resultant lithofacies observed in the core into electrofacies with similar petrophysical properties an overall trend of each lithofacies would be needed. This is supported by Davis (2018) who defines electrofacies as an interval where a unique combination of petrophysical log responses are describing the petrophysical properties and should solely be characterized based on well log response. According to Kennedy (2015) the recorded log becomes an average of the true variation in the reservoir when the beds are below well log resolution. Furthermore, the average beds in the Nordmela Formation is according to the definition after Passey et al. (2006) below well log resolution. In addition, the variable well log response observed in lithofacies C and E is prone to errors in defining the electrofacies and is interpreted as being related to the different amount of shale and thickness of shale laminae in the two lithofacies. Based on the variable thickness and petrophysical properties of the beds in the Nordmela formation and the shoulder bed effects of shale, the petrophysical evaluation of the Nordmela Formation is produced as one single interval.

### 7.1 Petrophysical quality of the Nordmela Formation

The Nordmela Formation in wells 7220/8-1 and 7220/7-1 should be regarded as two different facies related to the petrophysical evaluation. From variability in core measurements and core observations, the reservoir quality of well 7220/8-1 is higher than well 7220/7-1. The wells have a depth differences of approximately 500 meters, and therefore a petrophysical depth-difference is expected. Nevertheless, the wells have differences in petrophysical properties observed from core measurements and petrophysical trends such as different porosity versus permeability trend (Figure 27) in the wells. These differences are interpreted as being related to different facies related to the depositional system. According to Knight (2017) well 7220/7-1 is located further away from the source compared to well 7220/8-1. The source is interpreted as coming from the east to north-east (Knight, 2017). Based on this it would be expected that well 7220/7-1, which is in the more distal part of the mouth bar complex comprises of finer grain sediments, lower porosities and lower permeabilities than well 7220/8-1. This is also supported by the results after Thomas and Stieber (1975).

This study implies that new wells drilled in or around the study area may not be addressed in the same way as wells 7220/8-1 and well 7220/7-1. The petrophysical approach will be

dependent on where they are drilled related to the depositional system. Based on the evaluation on the two wells, the porosity model generated for the combination from density and sonic log indicates that this may be a good solution independently of depositional system for other wells. With available gamma ray log and true resistivity scanner, future wells can construct a reliable water saturation model after Thomas and Stieber (1975) and from series resistivity model after Klein and Martin (1997) respectively. Furthermore, the information obtained for the model after Thomas and Stieber (1975) were similar to what was observed in the cores. Hence Thomas and Stieber (1975) in thinly bedded reservoir will be a good tool to understand the shale distribution and reservoir properties for future wells which are drilled without being cored. The uncertainty for future wells from this study is the permeability model, hence more wells should be considered in order to create a general model for the Nordmela Formation.

## 7.2 Porosity models

Combining the two derived porosity models from sonic and density log make a good alternative for the Nordmela Formation. Since the porosity from density are underestimated and porosity from sonic are overestimated, combined they seem to compensate for each other's weaknesses and a better porosity model can be established. Porosity from high resolution density is often preferred as method (Springer et al., 2015). Nevertheless, in an oil-water system with porosities much less than 50 % the calculated porosity from density log (equation 8) will be much more sensitive to change in density (Kennedy, 2015). For input in equation 8, an average matrix density is used. This may give error especially in a heterolithic formation such as the Nordmela Formation which alternates between shale and sandstone. According to Kennedy (2015) the sonic derived porosity should not be the first choice due to the fact the lack of a universal relationship between porosity and compressional velocity. Nevertheless, he describes that the advantages of this method are in low porosity intervals it does not lose accuracy.

## 7.3 Thomas and Stieber (1975) methodology

Previously, the method of Thomas and Stieber (1975) has frequently been misunderstood in the way that the volume of shale calculated from the gamma ray log is used as input to the diagram instead of gamma ray obtained from the gamma ray log (e.g., Dejtrakulwong et al., 2009; Nasser et al., 2011; Kantaatmadja et al., 2015). This is because the three endpoints in their cross-plot are calculated based on gamma, which is one minus the volume of shale ( $\text{gamma} = 1 - \text{volume of shale}$ ) calculated from gamma ray log. This leads to higher values of laminated shale then the model tends to (if the point dose not accurately located on the

laminated shale line) because the dispersed shale end point are located slightly to the right (red) from where it should be (Figure 35). Using the Thomas and Stieber (1975) cross-plot, the dispersed clay content will come in addition to the already existing sandstone fraction. Hence, if a clean sandstone has a gamma ray value of 20 API and porosity of 30 % where the 30 % is filled with dispersed clay. Using the volume of shale as input this will result 0.3 fr.b.v shale and converting this to gamma ray the value should then be 50 API. This is only corrected if the sandstone fraction is displaced by shale ( $0.3 \text{ fr.b.v} * 120 \text{ API} + (1 - 0.3) \text{ fr.b.v} * 20 \text{ API}$ , red envelope in Figure 35), which is not the case. The resultant gamma ray reading will therefore be 56 API ( $20 \text{ API} + (120 \text{ API} * 0.3 \text{ fr.b.v})$ , blue envelope in Figure 35).

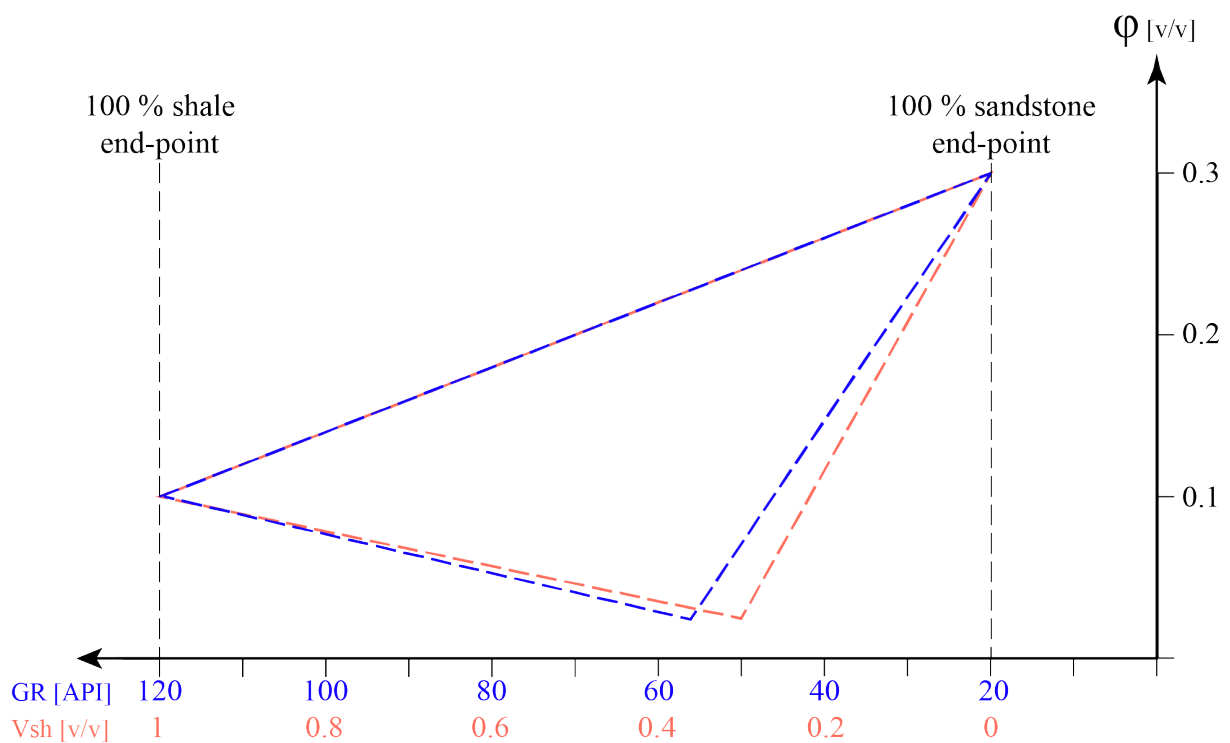


Figure 35 – Thomas and Stieber cross-plot using gamma ray (GR) and volume of shale ( $V_{sh}$ ) as input together with porosity. Using gamma ray the envelope displayed in blue, which is the correct approach after Thomas and Stieber, correlated with the wrong approach (red envelope) using volume of shale as input.

Based on the results obtained from the blue envelope (Figure 35) correlated with core observations, this study implies that the method after Thomas and Stieber (1975) may reveal great understanding related to petrophysical properties of a thinly bedded reservoir such as the Nordmela Formation. The method can be applied on future wells with available gamma ray log and a calculated porosity log (in this study from density and sonic log for both wells).

#### 7.4 Conflicting shale conductivity results

The different shale volumes calculated after Thomas and Stieber (1975) is used to understand the shale conductivity results in the Nordmela Formation. Furthermore, this promotes that shale is not only shale, but the position and distribution are also important. Shale conductivity in wells 7220/8-1 and 7220/7-1 are contradicting correlating results from special core analysis with results from resistivity logs. The reason for this is related to what shale type the measurements is affected by. Where the special core analysis is taken in the sandstone intervals in order to reveal sandstone properties, hence the dispersed clay will be the contributor to increased shale conductivity. For the resistivity log, the volume of laminated shale is the largest contributor to increasing shale conductivity. Results for dispersed shale calculation and lithofacies interpretation reveal that the plugs in well 7220/8-1 are taken in the cleaner sandstone intervals correlated with well 7220/7-1. The plugs represent that exact lithofacies or interval, but it does not necessarily mean that it is representing the entire well. In addition, for the resistivity in the water zone obtained from the resistivity logs, the uncertainty lies in the fact that there are observed residual oil below water-oil contact (Skjelle et al., 2011; Paulsen et al., 2012).

#### 7.5 Hydrocarbon underestimation

For the simplicity of this chapter the methods after Archie (1942), Waxman and Smits (1968) and Poupon and Leveaux (1971) are referred to as conventional methods.

According to Passey et al. (2006) conventional water saturation analysis tends to overestimate water saturation in beds below resolution of logging tools due to presence of shale and the cation exchange capacity of clay minerals and, accordingly, the increase in parallel conductivity. Based on the water saturation results, this is not the case for the Nordmela Formation. Using the water zone as a reference point for the water saturation models, it would be expected that the water saturation in this zone would be close to or equal to 1. Culley et al. (1976) explain that resistivity of earth materials are controlled by four major factors: Type of materials, fluid content, temperature and ice content. Furthermore, they describe how resistivity is affected by the different materials (from high to low resistivity values) where basement rocks have relatively high resistivity values, then loose sand, sandstone and clay as the highest conductive material. The Loppa High is most likely the source of the Nordmela Formation at the Johan Castberg Field (Knight, 2017). Eroded crystalline rocks from this high with redeposition in the Lower Jurassic may be a possibility but is not documented in the

petrography reports (Aase, 2011; Tårup, 2012). Furthermore, the petrography reports conclude that the wells have been buried much deeper (500-1000 m), which makes unconsolidated loose sand less possible. Temperature increases with depth and will be reflected as a decrease in resistivity. According to Skjelle et al. (2011) and Paulsen et al. (2012) residual oil shows are observed in the core chips below oil-water contact in wells 7220/8-1 and 7220/7-1. The oil shows in well 7220/8-1 are observed down to 1400 m measured depth and in well 7220/7-1 down to 2121 m measured depth. Hence, this may be the reason for having high resistivity readings in the water zone. Nevertheless, oil saturation is observed below 1400 m measured depth (where residual oil is observed) in well 7220/8-1 which may indicate that especially the conventional water saturation models are underestimating the water saturation in the Nordmela Formation. In thin laminated formation Hagiwara (1997) found that the resistivity of sand was overestimated by conventional shoulder bed corrections (equation 27), when anisotropy of shale was not accounted for. Furthermore Passey et al. (2006) stated that if it was possible to develop a resistivity tool that accurately measured the resistivity perpendicular and parallel to bedding in thinly laminated reservoirs, the uncertainty of water saturation calculations would be greatly reduced.

According to Bergaya and Lagaly (2013) montmorillonite is a part of the smectite family with high cation exchange capacity. Well 7220/7-1 have measured higher cation exchange capacity on core plugs from special core analysis than well 7220/8-1. Well 7220/7-1 is the only well that contains some smectite. According to Holtz and Kovacs (1981) montmorillonite, hence smectite have much higher ability to adsorb water than for example illite and kaolinite due to the large surface area which supports the differences in the cation exchange capacity from special core analysis. Nevertheless, the difference in cation exchange capacity has not affected the estimation of water saturation as explained by Passay et al. (2006) with higher water saturation estimation in well 7220/7-1 using the conventional water saturation models. This is probably related to the conflicting shale conductivities in the two wells.

Waxman and Smits (1968) divided their shaly sand into two ranges: (1) clay fraction composing of almost pure montmorillonite with a cation exchange capacity between 0.3 and 1.5 meq/cm<sup>3</sup>; and (2) clay fraction with mainly kaolinite and illite with an exchange capacity between 0 and 1.5 meq/cm<sup>3</sup>. Based on the low shale conductivity found from equation 24 in the Nordmela Formation related to the two ranges from Waxman and Smits (1968), the shale effect on resistivity log is regarded as neglectable for hydrocarbon saturation estimation. In

addition, Poupon and Leveaux (1971) state that equation 26 should be used to correct for overestimation of water saturation where the resistivity of shale versus resistivity of water fraction is low in reservoirs with high shale content. Equation 26 had not the expected effect in the Nordmela Formation which indicates that the resistivity of shale versus resistivity of shale fraction is not low. Hence, this supports the results obtained from equation 24 after Juhasz (1981) that the conductivity of shale in the Nordmela Formation is neglectable.

#### 7.6 Net sand fraction from cut-off

Using the methods after Thomas and Stieber (1975) and Klein and Martin (1997) a trustworthy fractional net-to-gross could fairly easy be established correlated with the estimated cut-off used for conventional water saturation models. Passey et al. (2006) demonstrated using a synthetic thin-bedded model how net sand fractions from cut-off bear little resemblance to the actual value. Furthermore, they simulate how net-to-gross is overestimated with cut-off over 50 % and underestimated with cut-off below 50 %. Again, the overestimation will lead to overestimation of hydrocarbon pore fraction using these methods in the Nordmela Formation.

From Thomas and Stieber (1975) a relationship of different shale content could be obtained. The water saturation model was constructed based on net-sand, which also was the case from using the series resistivity model after Klein and Martin (1997). With conventional water saturation models, cut-off need to be set to exclude zones in formations that are non-net. Therefore, the results obtained after Thomas and Stieber (1975) and Klein and Martin (1971) are regarded as more certain for the production profile. If the resistivity scanner data is available, it is regarded as giving the most accurate results for hydrocarbon estimation in a thinly bedded reservoir such as the Nordmela Formation. However, the net-to-gross obtained after Thomas and Stieber (1975) were very similar what was obtained from the series resistivity model after Klein and Martin (1997). Therefore, if the resistivity scanner data is not available, the method after Thomas and Stieber gives accurate results also when it comes to net-to-gross, and thus hydrocarbon saturation.

#### 7.7 Permeability model

This study demonstrates that the volume of shale obtained from Thomas and Stieber (1975) improves the permeability model. Relating the permeability not only to the porosity but also to the type (dispersed- and laminated) of shale is also described by Neasham (1977) and seen in this analysis. When the core plugs are taken such that the shalier intervals are included the

(blue area, Figure 30) the porosity model is a good match with the core permeability points. Nevertheless, if the core plugs are taken in such a way that the shalier intervals are not included (green area, Figure 30) the gap between the core points increases and the permeability model is reflecting the difference of permeability in sandstone lamina and log permeability. The reason for this is that the permeability model uses log porosity as input, and the density curve does not detect the shalier laminae that are missed by the core plugs. Although not perfect, the volume of shale after Thomas and Stieber (1975) as input corrects a long way in the right direction. Hence, without extracting sand only properties one would make an erroneous model. The method of Thomas and Stieber was mainly used to obtain relations between dispersed and laminated shale in the Nordmela Formation and further to improve the water saturation model. Nevertheless, the results from the permeability model may provide new insight into how to use the shale distributions obtained from Thomas and Stieber (1975) to improve the permeability model in thinly bedded reservoirs such as the Nordmela Formation.

#### 7.8 Source of errors

The study is based on wells 7220/8-1 and 7220/7-1 which are places with approximately seven kilometers from each other in the proximal and distal setting of a prograding mouth bar complex respectively. Therefore, uncertainty on where this study applies to wells targeting the Nordmela Formation should be considered on how far away they are drilled from the study area and in which part of the depositional system they are drilled.

The overburden permeability correction for the 500 m deeper well 7220/7-1 was lower than well 7220/8-1. Looking at the core plugs in well 7220/7-1, they were sampled in sandstone intervals with relatively low permeabilities, correlated with the core plugs from well 7220/8-1. Based on this, the overburden permeability correction estimated for well 7220/7-1 seemed unrepresentable. Hence, the overburden correction estimated for well 7220/8-1 was used as an analog to correct the plugs well 7220/7-1.



## 8 Conclusions

This study demonstrates using several methods (e.g. Archie (1942), Waxman and Smits (1968), Poupon and Leveaux (1971), Thomas and Stieber (1975) and Klein and Martin (1997)) that all petrophysical estimates in the Nordmela Formation end up wrong without thin-bed analysis. This will further lead to incorrect volume in place calculations and possible misleading dynamic properties such as permeability.

- 1) If true resistivity scanner data is available, it is regarded as giving the most confident water saturation model and net-to-gross ratio. Hence, the series resistivity model as input for the water saturation model in the Nordmela Formation is recommended.
- 2) The results obtained using the method after Thomas and Stieber (1975) improves both the permeability model and the water saturation model in the Nordmela Formation. In addition, a realistic net-to-gross ratio is achieved. This method should be used for water saturation and net-to-gross calculations if true resistivity scanner data is not available. In addition, correlation between the laminated and dispersed shale calculation results and core interpretations show good differentiation between laminated and dispersed shale. Hence, the method give rise to an overall better understand of the reservoir and could be used for enhancing the production profile of the formation. Especially for future wells where core data is missing. Furthermore, this method demonstrates how important the understanding of shale distribution in a thinly bedded reservoir is. Shale should not be just considered as shale, but the position and distribution are important and can be using the method after Thomas and Stieber (1975).
- 3) The sonic log could be an additional input for the porosity model in the Nordmela Formation to correct for underestimation of porosity from the density log.
- 4) The understanding of the petrophysical properties of the shale in thinly bedded reservoirs contributes to correct the well logs for the shale effect. Therefore, core measurements not only in sandstone intervals but also in the shale lamina may give valuable information for the petrophysical evaluation.

- 5) Previous work done using the method after Thomas and Stieber (1975) should be revised in order to confirm if volume of shale as input instead of gamma ray have given falsely values affecting the petrophysical results.

## References

- Aase, N.E., 2011, Petrography report - Mineralogy, Diagenesis and Reservoir Quality of Well 7220/8-1 (Skrugard): Coporate Statoil, 31 p. [Restricted]
- Archie, G.E., 1942, The Electrical Resistivity Log as an Aid in Determining Some Reservoir Characteristics: Society of Petroleum Engineers, v. 146, p. 54–62.
- Barton, C.D., and Karathanasis, A.D., 2017, Clay Minerals, *in* Lal, R. ed., Encyclopedia of Soil Science, Boca Raton, CRC Press, Taylor & Francis Group, p. 421–425.
- Bergaya, F., and Lagaly, G., 2013, General Introduction: Clays, Clay Minerals, and Clay Science, *in* Lagaly, G. and Bergaya, F. eds., Handbook of Clay Science (Second edition), London, Elsevier, p. 1–17.
- Bonewitz, R., 2012, Rocks and Minerals: New York, DK Publishing, 352 p.
- Breckels, I.M., and Van Eekelen, H.A.M., 1983, Relationship between Horizontal Stress and Depth in Sedimentary Basins: Journal of Petroleum Technology, v. 20, p. 2191–2199, doi:10.1016/0148-9062(83)91624-8.
- Campbell, C.V., 1967, Lamina, Laminaset, Bed and Bedset: Sedimentology, v. 8, p. 7–26, doi:10.1111/j.1365-3091.1967.tb01301.x.
- Cheng, K., and Heidari, Z., 2018, A New Method for Quantifying Cation Exchange Capacity in Clay Minerals: Applied Clay Science, v. 161, p. 444–455, doi:10.1016/j.clay.2018.05.006.
- Culley, R.W., Jagodits, F.L., and Middleton, R.S., 1976, E-Phase System for Detecting Buried Granular Deposits, *in Proceedings*, 54th Annual Meeting of the Transportation Research Board, Washington District of Columbia January 1975, Innovations in Subsurface Exploration of Soils, p. 1-10.
- Davis, J.C., 2018, Electrofacies in Reservoir Characterization, *in* Daya Sagar, B.S., Cheng, Q., and Agterberg, F. eds., Handbook of Mathematical Geosciences: Fifty Years of IAMG, Canada, Springer International Publishing, p. 211–223, doi:10.1007/978-3-319-78999-6\_11.
- Dejtrakulwong, P., Mukerji, T., and Mavko, G., 2009, Investigating Thomas-Stieber model for Property Estimation of Thin-bedded Shaly-sand Reservoirs, *in Proceedings*, SEG Technical Program Expanded Abstracts 2009, Huston, Texas, Society of Exploration Geophysicists, p. 1965–1969, doi:10.1190/1.3255240.
- Gabrielsen, R.H., Færseth, R.B., Jensen, L.N., Kalheim, J.E., and Riis, F., 1990, Structural Elements of the Norwegian Continental Shelf - Part I: The Barents Sea Region: Norway, Norwegian Petroleum Directorate, NPD-Bulletin 6, 57 p.
- Glover, P.W.J., 2005, Petrophysics: Aberdeen, United Kingdom, University of Aberdeen, p. 328.

- Glørstad-Clark, E., Faleide, J.I., Lundschieen, B.A., and Nystuen, J.P., 2010, Triassic Seismic Sequence Stratigraphy and Paleogeography of the Western Barents Sea Area: Marine and Petroleum Geology, v. 27, p. 1448–1475.
- GoogleEarth, 2020, Google Earth: <https://earth.google.com/web/@72.6793504,37.3807943,-22.35953895a,3543591.19096351d,35y,0h,0t,0r/data=Ck8aTRJHCiUweDQ0NTRiMTM4YmFiNGQyZDE6MHg4ODI2ZTQ3Y2QxOTAzOGYwGfxH8NBBv1JAIWLq-HmdjUJAKgxCYXJlbnRzaGF2ZXQYAiAB> (accessed January 2020).
- Hagiwara, T., 1997, Induction Log Shoulder-Bed Corrections to Anisotropic Formations and the Effect of Shale Anisotropy in Thinly Laminated Sand/Shale Sequences: SPE Formation Evaluation, v. 12, p. 235–240, doi:10.2118/36508-PA.
- Henriksen, E., Ryseth, A.E., Larssen, G.B., Heide, T., Rønning, K., Sollid, K., and Stoupakova, A.V., 2011a, Tectonostratigraphy of the greater Barents Sea: Implications for Petroleum Systems: Geological Society, v. 35, p. 163–195, doi:10.1144/M35.10.
- Henriksen, E. et al., 2011b, Uplift and Erosion of the Greater Barents Sea: Impact on Prospectivity and Petroleum Systems: Geological Society, v. 35, p. 271–281, doi:10.1144/M35.17.
- Holtz, R.D., and Kovacs, W.D., 1981, An Introduction to Geotechnical Engineering: Englewood Cliffs, New Jersey, Prentice-Hall, 733 p.
- Indrevær, K., Gabrielsen, R.H., and Faleide, J.I., 2017, Early Cretaceous Synrift Uplift and Tectonic Inversion in the Loppa High Area, Southwestern Barents Sea, Norwegian shelf: Journal of the Geological Society, v. 174, p. 242–254, doi:10.1144/jgs2016-066.
- Juhasz, I., 1981, Normalised Qv - The Key to Shaly Sand Evaluation Using the Waxman-Smits Equation in the Absence of Core Data, in *Proceedings*, 22nd Annual Logging Symposium, Mexico, Society of Petrophysicists and Well-Log Analysts, p. 36.
- Kantaatmadja, B.P., Rashid, S.Bt., Nurhono, A.A., Masoudi, R., Neville, T., Taesoo, K., and Basu, D., 2015, Thinly Bedded Reservoir Study, Application of Sand-Slit-Clay (SSC)-SHARP-Thomas Stieber Juhasz Models, in a Deep Water Field, Offshore Sabah, Malaysia, in *Proceedings*, SPE/IATMI Asia Pacific Oil & Gas Conference and Exhibition, Nusa Dua, Bali, Indonesia, Society of Petroleum Engineers, p. 16, doi:10.2118/176302-MS.
- Kennedy, M., 2015, Practical Petrophysics: Amsterdam, Elsevier, Developments in petroleum science, v. 62, 403 p.
- Klausen, T.G., Müller, R., Sláma, J., Olausson, S., Rismyhr, B., and Helland-Hansen, W., 2018, Depositional History of a Condensed Shallow Marine Reservoir Succession: Stratigraphy and Detrital Zircon Geochronology of the Jurassic Stø Formation, Barents Sea: Journal of the Geological Society, v. 175, p. 130–145, doi:10.1144/jgs2017-024.
- Klein, J.D., and Martin, P.R., 1997, The Petrophysics of Electrically Anisotropic Reservoirs: The Log Analyst, v. 38, p.25-36

- Knight, S., 2017, Geology-Geophysics and Petrophysics DG3 - Johan Castberg: Project Development, Statoil, 379 p. [Restricted]
- La Vigne, J., Herron, M., and Hertzog, R., 1994, Density-Neutron Interpretation in Shaly Sands, *in Proceedings*, SPWLA 35<sup>th</sup> Annual Logging Symposium, Tulsa, Oklahoma, Society of Petrophysicists and Well-Log Analysts, p. 16.
- Leveridge, R.M., 2010, New Resistivity-Logging Tool Helps Resolve Problems of Anisotropy, Shoulder-Bed Effects: *Journal of Petroleum Technology*, v. 62, p. 20–22, doi:10.2118/0810-0020-JPT.
- Lundegard, P.D., 1992, Sandstone Porosity Loss; a “Big Picture” view of the Importance of Compaction: *Journal of Sedimentary Research*, v. 62, p. 250–260, doi:10.1306/D42678D4-2B26-11D7-8648000102C1865D.
- Matapour, Z., and Karlsen, D.A., 2017, Geochemical Characteristics of the Skrugard Oil Discovery, Barents Sea, Arctic Norway: A “Palaeo-Biodegraded – Gas Reactivated” Hydrocarbon Accumulation: *Journal of Petroleum Geology*, v. 40, p. 125–152, doi:10.1111/jpg.12669.
- Minh, C.C., Clavaud, J.-B., Sundararaman, P., Froment, S., Caroli, E., Billon, O., and Davis, G., 2007, Graphical Analysis of Laminated Sand-Shale Formations in the Presence of Anisotropic Shales, *in Proceedings*, SPWLA 48<sup>th</sup> Annual Logging Symposium, Austin, Texas, Society of Petrophysicists and Well-Log Analysts, p. 10.
- Nasser, M., Mavko, G., Dvorkin, J., and Ostroff, G., 2011, Rock Physics Analysis of Deepwater Sediments, West Africa, *in Proceedings*, SEG Annual Meeting, San Antonio, Texas, Society of Exploration Geophysicists, p. 2103–2107, doi:10.1190/1.3627625.
- Neasham, J.W., 1977, The Morphology of Dispersed Clay in Sandstone Reservoirs and its Effect on Sandstone Shaliness, Pore Space and Fluid Flow Properties, *in Proceedings*, SPE Annual Fall Technical Conference and Exhibition, Denver, Colorado, Society of Petroleum Engineers, p. 8, doi:10.2118/6858-MS.
- NPD, 2019a, Field, Johan Castberg: [https://factpages.npd.no/ReportServer\\_npdpublic?/FactPages/PageView/field&rs:Command=Render&rc:Toolbar=false&rc:Parameters=f&NpdId=32017325&IpAddress=152.94.112.78&CultureCode=en](https://factpages.npd.no/ReportServer_npdpublic?/FactPages/PageView/field&rs:Command=Render&rc:Toolbar=false&rc:Parameters=f&NpdId=32017325&IpAddress=152.94.112.78&CultureCode=en) (accessed November 2019).
- NPD, 2019b, NPD FactMaps: [https://factmaps.npd.no/factmaps/3\\_0/](https://factmaps.npd.no/factmaps/3_0/) (accessed November 2019).
- Onovughe, E., and Sofolabo, A., 2016, Saturation Modelling: Using the Waxman-Smits Model/Equation in Saturation Determination in Dispersed Shaly Sands: *Journal of Multidisciplinary Engineering Science and Technology*, v. 3, p. 4985–4985.
- Passey, Q.R., Dahlberg, K.E., Sullivan, K.B., Yin, H., Brackett, R.A., Xiao, Y.H., and Guzmàn-García, A.G., 2006, Petrophysical evaluation of Hydrocarbon Pore-Thickness in Thinly Bedded Clastic Reservoirs: Tulsa, Oklahoma, The American Association of Petroleum Geologists, 210 p.

- Paulsen, S., Larsen, V., Lambert, A., and Tuppen, D., 2012, Final Well Report, Well 7220/7-1 & 72220/7-U-1, Havis, PL 532: Statoil Final Well Report, 204 p. [Restricted]
- Poupon, A., and Leveaux, J., 1971, Evaluation of Water Saturation in Shaly Formations: The Log Analyst, v. 12, p. 3–8.
- Revil, A., and Cathles, L.M., 1999, Permeability of Shaly Sands: Water Resources Research, v. 35, p. 651–662, doi:10.1029/98WR02700.
- Scherbaum, F., 1982, Seismic Velocities in Sedimentary Rocks — Indicators of Subsidence and Uplift: Geologische Rundschau, v. 71, p. 519–536, doi:10.1007/BF01822381.
- Schlumberger, 2013, Schlumberger Log Interpretation Chart: Texas, Schlumberger Oilfield Communications, 279 p.
- Schön, J.H., 2015, Physical Properties of Rocks: Fundamentals and Principles of Petrophysics: Amsterdam, Elsevier, Developments in petroleum science Volume 65, 497 p.
- Serra, O., and Serra, L., 2004, Well logging: data acquisition and applications: Méry Corbon, Serralog, 674 p.
- Skjelle, H., Larsen, V., Vollan, Ø., and Alm, D., 2011, Final Well Report, Well 7220/8-1, Skrugard, PL 532: Statoil Final Well Report, 222 p. [Restricted]
- Springer, M., Pettersen, I.H.A., and Seland, T.A., 2015, Lithology and Fluid Phase Prediction (LFP): Guideline to Well Logs and Petrophysical Routines: Statoil Internal Guideline, 125 p. [Restricted]
- Tårup, E.O., 2012, Petrography Study for PL 532, Well 7220/7-1 (Havis): Coporate Statoil, 46 p. [Restricted]
- Thomas, E.C., and Stieber, S.J., 1975, The distribution of Shale in Sandstones and its Effect Upon Porosity, in *Proceedings*, SPWLA 16<sup>th</sup> Annual Logging Symposium, New Orleans, Louisiana, Society of Petrophysicists and Well-Log Analysts, p. 15.
- Tourtelot, H.A., 1960, Origin and Use of the Word “shale”: American Journal of Science, v. 258-A, p. 335- 343.
- Vernik, L., 2016, Seismic Petrophysics in Quantitative Interpretation: Tulsa, Oklahoma, Society of Exploration Geophysicists, 227 p.
- Waxman, M.H., and Smits, L.J.M., 1968, Electrical Conductivities in Oil-Bearing Shaly Sands: Society of Petroleum Engineers Journal, v. 8, p. 107–122, doi:10.2118/1863-A.
- Wentworth, C.K., 1922, A Scale of Grade and Class Terms for Clastic Sediments: The Journal of Geology, v. 30, p. 377–392.
- Worsley, D., Johansen, R., and Kristensen, S.E., 1988, The Mesozoic and Cenozoic succession of Tromsøflaket, in Dalland, A., Worsley, D., and Ofstad, K. eds., A Lithostratigraphic Scheme for the Mesozoic and Cenozoic succession offshore mid-

and northern Norway: Stavanger, Norwegian Petroleum Directorate, NPD-Bulletin 4, p. 42–61.

Wyllie, M.R.J., Gregory, A.R., and Gardner, L.W., 1956, Elastic Wave Velocities in Heterogeneous and Porous Media: *Geophysics*, v. 21, p. 41–70, doi:10.1190/1.1438217.

**Total Stress Methode after Breckels and Eekelen (1982)**

Havis									
Nordmeia									
	gradient	g/cc	g/cc	g/cc	ref. Depth	Stress	Stress	Stress	Stress
	bar/m	OB	LOT	Hydrostat	m TVDmsl	from	from	from	used in
				c		sources	other	calc	
Min. horizontal Stress	SigX	0.1530	1.4800		1910	277.0	307.5	292.3	
Max. horizontal stress	SigY				1910			333.6	
Overburden Stress	SigZ	0.1983	1.6200		1910	303.2		374.8	
Pore pressure	Pp				1910			202.4	
Ppn (hydrostatic)	Ppn				1910	187.2		187.2	
Biot's constant	alfa								1
Effective equivalent hydrostatic stress	today								
	NCP	131.2							

	Integrated density	Pore pressure	Formation Pressure
m MID	1950	1950	1950
m TVDmsl	1910	1910	1910
rhob sum	3821 (g/cc)*m	202.4 bar	21.1 Mpa

Skungard									
Nordmeia									
	gradient				ref. Depth	Stress	Stress	Stress	Stress
					m	from	from	from	bar
						sources	other	calc	
Min. horizontal Stress	SigX	0.1490	1.5200		1356	202.0	206.6	202.0	
Max. horizontal stress	SigY				1356			225.5	
Overburden Stress	SigZ	0.1837	1.6200		1356	215.3		249.1	
Pore pressure	Pp				1356			143.5	
Ppn (hydrostatic)	Ppn				1356	132.9		132.9	
Biot's constant	alfa								1
Effective equivalent hydrostatic stress	Initially								
	NCP	82.1							

	Integrated density	Pore pressure	Formation Pressure
m MID	1379		
m TVDmsl	1356		
rhob sum	2539 (g/cc)*m	143.454 bar	14.7 Mpa

Well	7220/8-1	7220/7-1
NCP	80 Bar	130 Bar
Porosity Correction	0.986	0.97
Permeability Correction	0.799	0.905

Integrated density (TVD msf):

**Havis:**  
 Assume 1.035 g/cc from 0-365 m (waterdepth)  
 Assume 2.3 g/cc from 365 to 1014.35 m  
 From 1014.35 onwards: use rhob

**Skungard:**  
 Assume 1.035 g/cc from 0-374 m (waterdepth)  
 Assume 2.3 g/cc from 374 to 816.3 m  
 From 816.3 onwards: use rhob

$S_x = 0.0053 * D^{**1.145} - 0.46 * (P_p - P_{pn})$  in Mpa (D in m)  
 (if no horizontal stress data is available)  
 In this case prefer LOT data, since correlation not appropriate for deep water

$P_{pn} = 9.81 * Depth^{1.0} * 1000 / 165$  - hydrostatic pressure

**Appendix 1**  
 Net confining pressure



## Appendix 2

A – Loglan code for volume of shale from gamma ray log:

```

dowhile GET_FRAME ()
/* Check logs present
if (GR == MISSING) then
  VSH_U = MISSING
  VSH = MISSING
/* Calculate shale volumes from gamma ray log
else
  VSH_U = (GR - GRMIN)/(GRMAX-GRMIN)
/* Limit result
  VSH = min(max(0,VSH_U),1)
endif
/* Store answers
call PUT_FRAME ()
enddo
end
  
```

Location	Mode	Name	Type	Unit	Default	Comment	Validation	Visible
Interval	Input	GRMAX	REAL	GAPI	120	GR value in shale		TRUE
Interval	Input	GRMIN	REAL	GAPI	40	GR value in clean sand		TRUE
Log	Input	GR	REAL	GAPI	GR	Gamma-ray log		TRUE
Log	Output	VSH_U	REAL	V/V	VSH_U	Volume of Shale (unlimited)		TRUE
Log	Output	VSH	REAL	V/V	VSH	Volume of Shale (limited)		TRUE

B – Loglan code for volume of shale from neutron-density separation:

```

dowhile GET_FRAME ()
/* Check logs present
if (DEN == MISSING | NEU == MISSING) then
  VSH_DN = MISSING
  VSH = MISSING
/* Calculate shale volumes in normal situation
else
  OLOG = (((DEN-1.95)*10) - (10-(0.15+NEU )/0.06))
  OSAND = (((DEN_SAND-1.95)*10) - (10-(0.15+NEU_SAND )/0.06))
  OSHALE = (((DEN_SHALE-1.95)*10) - (10-(0.15+NEU_SHALE )/0.06))
  VSH_DN = (OLOG - OSAND) / (OSHALE - OSAND)
/* Limit result
  VSH = LIMIT (VSH_DN, 0, 1)
Endif
/* Store answers
call PUT_FRAME ()
enddo
end

```

Location	Mode	Name	Type	Unit	Default	Comment	Validation	Visible
Constant	Input	OSAND	REAL			Seperation of 100% sands...		FALSE
Constant	Input	OSHALE	REAL			Seperation of 100% shale		FALSE
Constant	Input	NEU_SHALE	REAL	V/V		Neutron porosity		TRUE
Constant	Input	NEU_SAND	REAL	V/V		Neutron porosity		TRUE
Constant	Input	DEN_SHALE	REAL	G/C3		Bulk Density		TRUE
Constant	Input	DEN_SAND	REAL	G/C3		Bulk Density		TRUE
Log	Input	DEN	REAL	G/C3		Bulk Density		TRUE
Log	Input	OLOG	REAL			Log seperation		FALSE
Log	Input	NEU	REAL	V/V		Neutron Log		TRUE
Log	Output	VSH_DN	REAL	V/V		Volume of Shale		TRUE
Log	Output	VSH	REAL	V/V		Volume of Shale		TRUE

C – Loglan code for porosity from density log

```

dowhile GET_FRAME ()
/* Check density present and parameters valid
if (DEN_LOG == MISSING) then
    PHIE_DEN = MISSING
    PHIE = MISSING
else
/* Calculate shale volumes in normal situation
    PHIE_DEN = ( DEN_MA - DEN) / ( DEN_MA - DEN_FLUID )
/* Limit result
    PHIT = LIMIT ( PHIE_DEN, 0, 1 )
endif
/* Store answers
call PUT_FRAME ()
enddo
end

```

Location	Mode	Name	Type	Unit	Default	Comment	Validation	Visible
Interval	Input	DEN_MA	REAL	G/CM3	2.65	Matrix Density	0:200	TRUE
Interval	Input	DEN_FLUID	REAL	G/CM3	1	Fluid Density	0:1000	TRUE
Log	Input	DEN	REAL	G/CM3	DEN	Density log	0:1000	TRUE
Log	Output	PHIT_U	REAL	v/v	PHIT_U	Porosity from gamma ray		TRUE
Log	Output	PHIT	REAL	v/v	PHIT	Limited volume of porosity		TRUE

D – Loglan code for porosity from sonic log

```

dowhile GET_FRAME ()
  /* Check density present and parameters valid
  if (AC == MISSING) then
    PHITDT = MISSING
  else
    /* Calculate shale porosity from sonic log
    PHITDT_U = (1/CP)*(( AC - DT_MA) / ( DT_F - DT_MA )
    /* Limit result
    PHITDT = min(max(0,PHITDT_U),1)
  endif
  /* Store answers
  call PUT_FRAME ()
enddo
end

```

Location	Mode	Name	Type	Unit	Default	Comment	Validation	Visible
Constant	Input	CP	REAL	V/V	1	Compaction		TRUE
Interval	Input	DT_MA	REAL	US/...	54	DT in matrix	0:200	TRUE
Interval	Input	DT_F	REAL	US/...	189	DT in fluid	0:1000	TRUE
Log	Input	AC	REAL	US/...	AC	Sonic Log	0:1000	TRUE
Log	Output	PHITDT_U	REAL	v/v	PHITDT_U	Porosity from sonic		TRUE
Log	Output	PHITDT	REAL	v/v	PHITDT	Limited volume of porosity		TRUE

```

dowhile GET_FRAME ()
  /* Calculate dispersed shale end point
  pordisp = (PORSH*PORS)
  grdisp = GRSA + (GRSH*PORS)

  /* Calculate the slope of the lines
  a0 = (PORS-PORDISP)/(GRSA-GRDISP)
  a2 = (PORSH-PORC)/(GRSH-GR)
  a1 = (PORS-PORSH)/(GRSA-GRSH)
  a3 = (PORSH-PORDISP)/(GRSH-GRDISP)

  /* Calculate porosity value from the three equations defining the Thomas and Stieber
  (1972) envelope
  x1 = (A1*(GR-GRSA)) + PORS
  x2 = (A3*(GR-GRSH)) + PORSH
  x3 = (A0*(GR-GRSA)) + PORS

  /* Check logs present
  if (GR == missing | PORC == missing) then
    XK = missing
    YK = missing
    LAM_SH = missing
    NET_GROSS = missing
    PHIT_NTG = missing
    DISP_SH = missing

  /* Check that point is plotted inside the envelope
  elseif (PORC >= X1) then
    LAM_SH = LIMIT (((GR-GRSA)/(GRSH-GRSA)), 0, 1)
    NET_GROSS = (1-LAM_SH)
    DISP_SH = 0
    PHIT_NTG = PORS
  elseif (PORC < X1 & PORC < X3 & PORC > X2) then
    LAM_SH = 0
    NET_GROSS = 1
    XJ = -(A2*GR)+PORC+(A0*GRSA)-PORS/(A0-A2)
    PHIT_NTG = LIMIT(((A2*(XJ-GR))+PORC), PORC, PORS)
    DISP_SH = LIMIT ((XJ-GRSA)/(GRDISP-GRSA), 0,1)
  elseif (PORC < X2 & PORC < X3 & PORC < X2) then
    LAM_SH = 0
    NET_GROSS = 1
    DISP_SH = 1
    PHIT_NTG = pordisp
  elseif (PORC > X3 & PORC < X1 & PORC < X2) then
    XK = -(A1*GRSA)+PORS+(A0*GR)-PORC/(A0-A1)
    LAM_SH = LIMIT (((XK-GRSA)/(GRSH-GRSA)), 0, 1)
    NET_GROSS = (1-LAM_SH)
    DISP_SH = 1

```

```

PHIT_NTG = pordisp
else
/* Calculate laminated shale and NtG
XK = (-(A1*GRSA)+PORSА+(A0*GR)-PORC)/(A0-A1)
YK = (A1*(XK-GRSA))+PORSА
LAM_SH = LIMIT (((XK-GRSA)/(GRSH-GRSA)), 0, 1)
NET_GROSS = (1-LAM_SH)
/* Calculate dispersed shale and NtG porosity
XJ = (-(A2*GR)+PORC+(A0*GRSA)-PORSА)/(A0-A2)
PHIT_NTG = LIMIT(((A2*(XJ-GR))+PORC), PORC, PORSА)
DISP_SH = LIMIT ((XJ-GRSA)/(GRDISP-GRSA), 0,1)
endif
/* Store answers
call PUT_FRAME ()
enddo
end

```

Location	Mode	Name	Type	Unit	Default	Comment	Validation	Visible
Constant	Input	GRSH	REAL	GAPI	134	Gamma ray laminated shal...		TRUE
Constant	Input	PORSА	REAL	V/V	0.27	Porosity clean sandstone ...		TRUE
Constant	Input	PORSH	REAL	V/V	0.08	Porosity laminated shale e...		TRUE
Constant	Input	GRSA	REAL	GAPI	29	Gamma ray clean sandsto...		TRUE
Log	Input	PORC	REAL	V/V	PHIT	Porosity		TRUE
Log	Input	GR	REAL	GAPI	GR	Gamma Ray		TRUE
Log	Output	LAM_SH	REAL	V/V	LAM_SH	Laminated shale		TRUE
Log	Output	XK	REAL	GAPI	XK	Gammaray of intersection ...		TRUE
Log	Output	YK	REAL	V/V	YK	Porosity of intersection - L...		TRUE
Log	Output	NET_GROSS	REAL	V/V	NET_GR...	Net interval		TRUE
Log	Output	XJ	REAL	GAPI	XJ	Gamma ray of intersection...		TRUE
Log	Output	PHIT_NTG	REAL	V/V	PHIT_NTG	Total Porosity of net to gro...		TRUE
Log	Output	DISP_SH	REAL	V/V	DISP_SH	Dispersed shale		TRUE
Local	Local	pordisp	DOUBLE					FALSE
Local	Local	grdisp	DOUBLE					FALSE
Local	Local	a0	DOUBLE					FALSE
Local	Local	a1	DOUBLE					FALSE
Local	Local	a3	DOUBLE					FALSE
Local	Local	a2	DOUBLE					FALSE
Local	Local	x1	DOUBLE					FALSE
Local	Local	x2	DOUBLE					FALSE
Local	Local	x3	DOUBLE					FALSE

F – Loglan code for water saturation after Archie (1942)

```

dowhile GET_FRAME ()
  /* Check resistivity present and parameters valid
  if (RT == MISSING) then
    SWT = MISSING
    SWT_ARC = MISSING
  elseif (PHIT == 0) then
    SWT = 1
    SWT_ARC =1
  else
    /* Calculate SWT after Archie (1942)
    SWT = (RW / (((PHIT)**M) * RT)) ** (1/N)
    /* Limit results
    SWT_ARC = LIMIT (SWT, 0, 1)
  endif
endif
  /* Store answers
  call PUT_FRAME ()
enddo
end

```

Location	Mode	Name	Type	Unit	Default	Comment	Validation	Visible
Interval	Input	M	REAL		2	Cementation Factor		TRUE
Interval	Input	N	REAL		2	Saturation Exponent		TRUE
Interval	Input	RW	REAL	OHMM	0.03	Resistivity of Water		TRUE
Log	Input	PHIT	REAL	V/V	PHIT	Total Porosity		TRUE
Log	Input	RT	REAL	OHMM	RDEP	True Resistivity		TRUE
Log	Output	SWT	REAL	V/V	SWT	Total Water Saturation		TRUE
Log	Output	SWT_ARC	REAL	V/V	SWT_ARC	Total Water Saturation Archie		TRUE

G – Loglan code for water saturation after Waxman and Smits (1968)

```

dowhile GET_FRAME ()
  /* Check log present and parameters valid
  if (VSH == MISSING) then
    BQV = BB
  else
    BQV = (BB + (AA *VSH))
  endif
  if (RT == MISSING) then
    SWT_W = MISSING
    SWT_WS = MISSING
  elseif (PHIT == MISSING) then
    SWT_W = MISSING
    SWT_WS = MISSING
  elseif (PHIT == 0) then
    SWT_W = 1
    SWT_WS = 1
  else
    /* Calculate SWT using iteration
    SWTB = 1
    do
      SWTA = SWTB
      SWTB = ((RW / (((PHIT)**M) * RT * (1+((RW*BQV)/SWTA)))) ** (1/N)
    until ((SWTA - SWTB) < 0.001)
    SWT_W = SWTB
    /* Limit result
    SWT_WS = LIMIT (SWT_W, 0, 1)
    SWT_WS = LIMIT (SWT_W, 0, 1)
  endif
  /* Store answers
  call PUT_FRAME ()
enddo
end

```

Location	Mode	Name	Type	Unit	Default	Comment	Validation	Visible	Tab Label
Parameter	Input	SWTA	REAL					FALSE	
Parameter	Input	SWTB	REAL					FALSE	
Parameter	Input	BQV	REAL	1/OHMM				FALSE	
Constant	Input	RW	REAL	OHMM	0.03	Resistivity of Water		TRUE	
Constant	Input	AA	DOUBLE			a in Y=ax + b in BQv regr...		TRUE	
Constant	Input	BB	DOUBLE			b in Y=ax + b in BQv regr...		TRUE	
Interval	Input	N	REAL		2	Saturation Exponent		TRUE	
Interval	Input	M	REAL		2	Cementation Factor		TRUE	
Log	Input	VSH	REAL	V/V	0.5	Volume of Shale		TRUE	
Log	Input	RT	REAL	OHMM		True Resistivity		TRUE	
Log	Input	PHIT	REAL	V/V		Total Porosity		TRUE	
Log	Output	SWT_W	REAL	V/V		Total Water Saturation		TRUE	
Log	Output	SWT_WS	REAL	V/V		Total Water Saturation		TRUE	



```

dowhile GET_FRAME ()
  /* calculate effective porosity
  PHIE = (PHIT - (PHISH * VSH))
  /* Check log present and parameters valid
  if (RT == MISSING) then
    SWE1 = MISSING
    SWE2 = MISSING
  elseif (VSH == MISSING) then
    SWE1 = MISSING
    SWE2 = MISSING
  elseif (PHIT == MISSING) then
    SWE1 = MISSING
    SWE2 = MISSING
  else
    /* Calculate water saturation
    d = (1-(bb *VSH))
    SWE1=LIMIT((1/(SQRT(RT)*((VSH**d)/SQRT(RSH)))+(PHIE**
      (M/2)/SQRT(A*RW))))**(2/N),0,1)
    SWE2 = LIMIT((1/((RT)*((VSH**d)/SQRT(RSH)))+(PHIE**
      (M/2)/SQRT(A*RW))))**(2/N),0,1)
    if (SWE1 == MISSING) then
      SWE1 = 1
    endif
    if (SWE2 == MISSING) then
      SWE2 = 1
    endif
    /* Calculate bulk fraction hydrocarbone
    BFHC1 = (1-SWE1)*PHIE
    BFHC2 = (1-SWE2)*PHIE
    /* Store answers
  call PUT_FRAME ()
enddo
end

```

Location	Mode	Name	Type	Unit	Default	Comment	Validation	Visible
Constant	Input	N	REAL			Saturation exponent		TRUE
Constant	Input	M	REAL			Cementation Factor		TRUE
Constant	Input	RW	REAL	OHMM		Resistivity of Water		TRUE
Constant	Input	RSH	REAL	OHMM		Shale resistivity		TRUE
Constant	Input	PHISH	DOUBLE	V/V				TRUE
Constant	Input	BB	DOUBLE		2	$d = 1 - (VSH/bb)$		TRUE
Constant	Input	A	REAL			Archie Constant		TRUE
Log	Input	VSH	REAL	V/V	VSH	Volume of Shale		TRUE
Log	Input	PHIT	REAL	V/V	PHIT_SD	Total Porosity		TRUE
Log	Input	RT	REAL	OHMM	RDEP	True Resistivity		TRUE
Log	Output	SWE1	REAL	V/V	SWE1_PL	Water Saturation		TRUE
Log	Output	SWE2	REAL	V/V	SWE2_PL	Water Saturation		TRUE
Log	Output	PHIE	DOUBLE	V/V		Effective Porosity		TRUE
Log	Output	BFHC1	DOUBLE	V/V				TRUE
Log	Output	BFHC2	DOUBLE	V/V				TRUE
Local	Local	d	DOUBLE					FALSE

I - Loglan code for calculating sand resistivity from parallel resistivity equation

```

dowhile GET_FRAME ()
  /* Check resistivity present and parameters valid
  if (RDEP == MISSING) then
    RSD = MISSING
  elseif (FSD == 0) then
    RSD = RDEP
  /* Calculate resistivity of net sand
  else
    RSD =(FSD/((1/RDEP)-((1-FSD)/RSH)))
  endif
  if (RSD < RDEP) then
    RSD = RDEP
  endif
  /* Store answers
  call PUT_FRAME ()
enddo
end

```

Location	Mode	Name	Type	Unit	Default	Comment	Validation	Visible
Constant	Input	RSH	REAL	OHMM		Shale resistivity		TRUE
Log	Input	FSD	REAL	V/V		Volume of sand		TRUE
Log	Input	RDEP	REAL	OHMM	RDEP	Deep resistivity log		TRUE
Log	Output	RSD	REAL	OHMM		Reisitivity of sand fraction		TRUE

J – Loglan code for calculating sand fraction and resistivity of sand from series resistivity after Klein and Martin (1997)

```

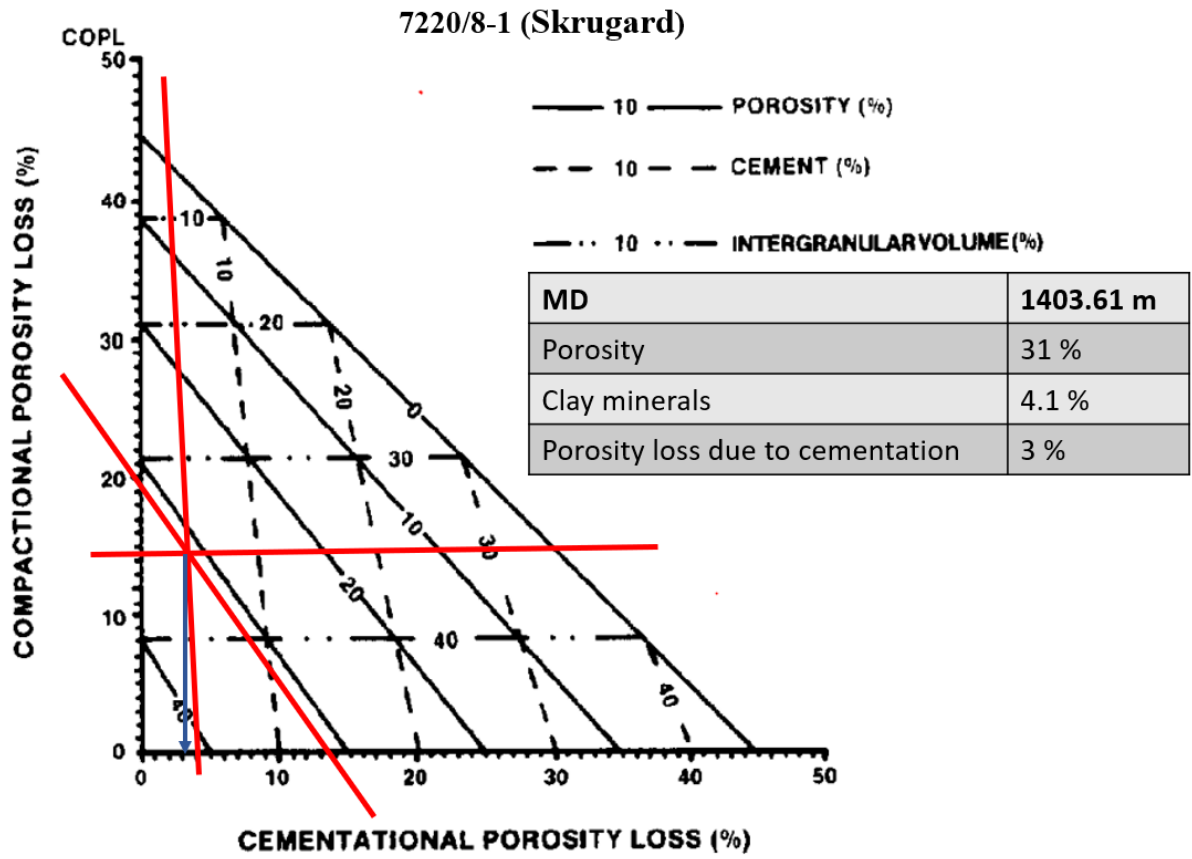
dowhile GET_FRAME ()
  /* factors for the "abc" formula to solve the second-degree equation
aa = (RH*RSHH-RSHV*RH)
bb = (RSHV*RH-RV*RH-RSHV*RSHH+RSHV*RH)
cc = (RSHV*RSHH-RSHV*RH-RV*RSHH+RV*RH)
  /* calculate fraction of sand
FSA1 = LIMIT((( -bb - (bb**2 - 4*aa*cc)**0.5)/(2*aa)),0,1)
  If (FSA1 == 0) then
    RSA1 = RH
  else
    RSA1 = (RV-((1-FSA1)*RSHV))/(FSA1)
    RSA2 = (FSA1*RH*RSHH)/(RSHH-RH+RH*FSA1)
    if (RSA1 == MISSING) then
      RSA1 = RSA2
    endif
  endif
  /* Store answers
call PUT_FRAME ()
enddo
end

```

Location	Mode	Name	Type	Unit	Default	Comment	Validation	Visible
Constant	Input	RSHH	REAL	OHMM	RSHH	Horizontal shale resistivity		TRUE
Constant	Input	RSHV	REAL	OHMM	RSHV	Vertical shale resistivity		TRUE
Log	Input	RH	REAL	OHMM	RH	Horizontal Resistivity		TRUE
Log	Input	RV	REAL	OHMM	RV	Vertical Resistivity		TRUE
Log	Output	FSA1	REAL	V/V	SF1	Sand fraction		TRUE
Log	Output	RSA2	REAL	OHMM	RSA1	Sand resistivity		TRUE
Log	Output	RSA1	REAL	OHMM	RSA1	Resistivity of sand		TRUE
Local	Local	aa	DOUBLE			a in ABC formula		FALSE
Local	Local	bb	DOUBLE			b in ABC formula		FALSE
Local	Local	cc	DOUBLE			c in ABC formula		FALSE

### Appendix 3

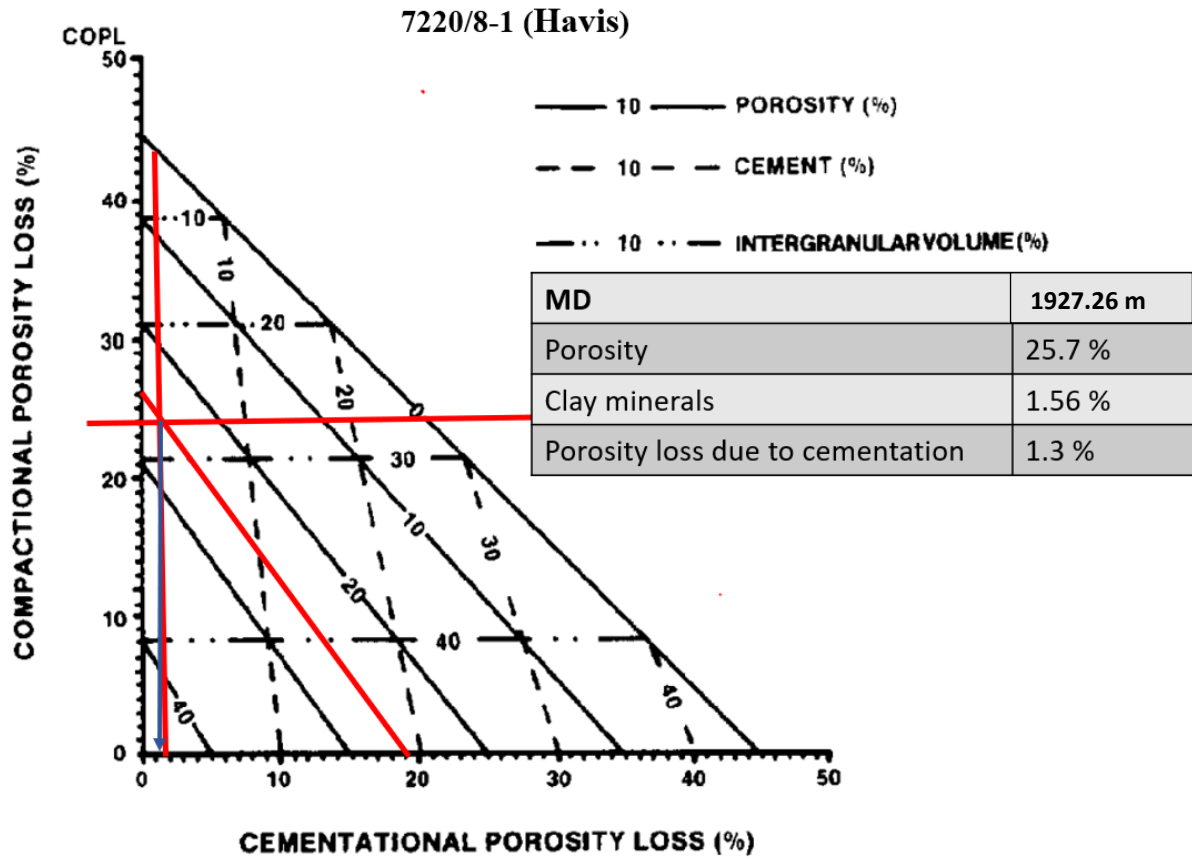
Estimation of porosity loss after Lundegard (1992) to find clean sandstone in Nordmela Formation zone 2 in well 7220/8-1



Cross plot from Lundegard (1992)

## Appendix 4

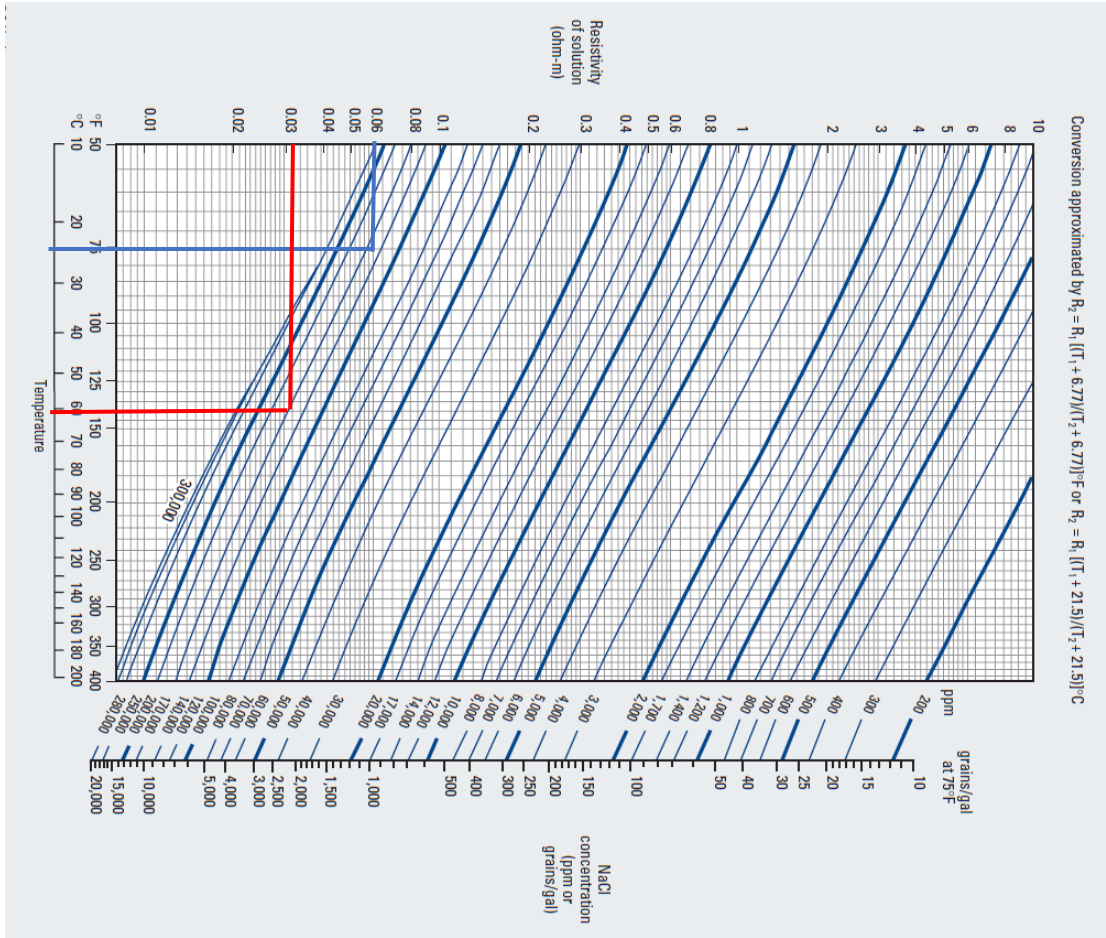
Estimation of porosity loss after Lundegard (1992) to find clean sandstone in Nordmela Formation zone 2 in well 7220/7-1



Cross plot from Lundegard (1992)

# Appendix 5

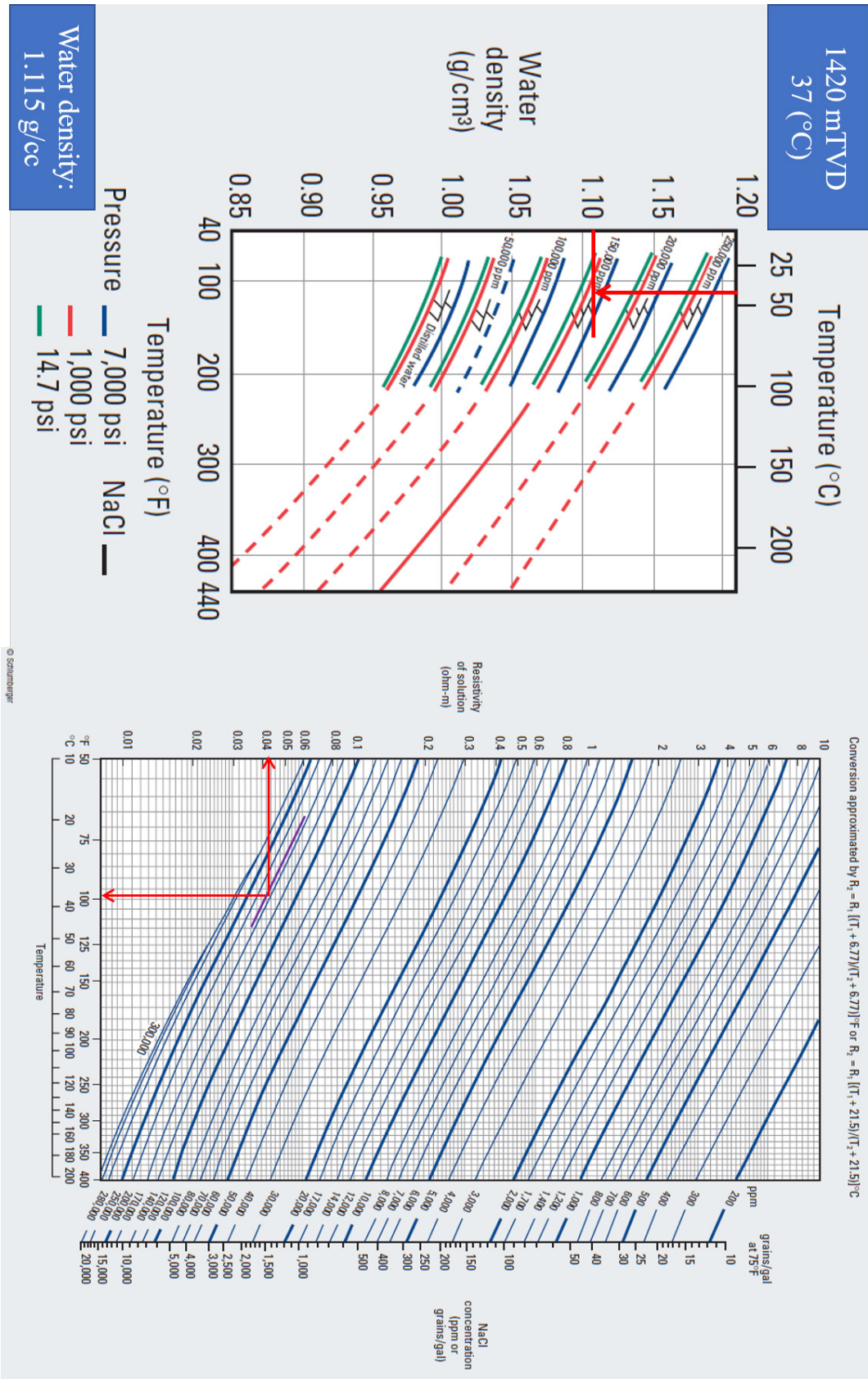
Converting water resistivity measured from standard condition to reservoir condition after Schlumberger (2013) in well 7220/7-1.



Stacoll Petroleum AS		7220/7-1		Havis	
<b>Identification</b>			<b>Sample Analysis</b>		
Sample no:	38-1b	CO2:	%	H2S:	ppm
Chamber no:	4671	Density:	1.1022 g/cc	at 15.0 °C	
Run:	38				
Depth:	1971.0 m MD RKB				
Sample nature:	Water				
Sampling date:	11.01.2012				
<b>Sampling Information</b>			<b>Comments</b>		
Measured pressure:	208.6 bar at 61.6 °C	Volume transferred from MPS = 440cc			
Filling time:	1 mins	50ml used offshore for analysis.			
Maximum drawdown:	4.2 bar	Contamination compared to mud when drilling 1971m MD RKB (lag)			
Pumped:	0.0 litre				
<b>Opening Pressure and Bubble Point</b>			<b>Contamination</b>		
Opening pressure:	50 bar at 0.0 °C	Lithium:	15 mg/l	Initial level in mud: 117.4 Bq/ml	
Bubble point:	bar at °C	Sodium:	40800 mg/l	Measured in sample: 7.8 Bq/ml	
<b>Sample Transfer</b>					
Bottle no:	TS-135604				
Bottle type:	Prolight TT-690-6+MB				
Transfer pressure:	300 bar at 60.0 °C				
Transfer medium:	Synthetic Oil				
Transfer duration:	15 minute				
Bottle volume:	629 cc				
Sample volume:	390 cc				
Gas cap volume:	30 cc				
Shipping pressure:	0 bar at 0.0 °C				
Sample:	1 of 1				
Coupled with samples:					
Transfer By: Finn Høedonsen			Date: 13.01.2012		

## Appendix 6

Converting water resistivity measured on standard condition to reservoir condition after Schlumberger (2013) in well 7220/8-1





## Appendix 7

Resultant regression lines for different input in well 7220/8-1 using core corrected total porosity from routine core analysis (PORC) where: KLHC – core corrected horizontal permeability; Vsh<sub>ND</sub> – volume of shale calculated from neutron-density separation; Vsh<sub>dis</sub> – dispersed (absolute) volume of shale calculated after Thomas and Stieber (1975); and Vsh<sub>lam</sub> – laminated volume of shale calculated after Thomas and Stieber (1975). Marked in yellow is the coefficient of correlation

### Well 7220/8-1 (PORC)

<i>Input</i>	<i>Regression</i>	<i>Correlation of dependent log and the independent log</i>
Simple regression total porosity Coefficient of correlation: 0.92	$\text{KLHC} = 10^{**}(-2.84009 + 20.5261 * \text{PORC})$	PORC: 0.85
Multiple Regression: Total porosity & volume of shale from neutron-density separation Coefficient of correlation: 0.93	$\text{KLHC} = 10^{**}(-2.32015 + 19.2078 * \text{PORC} - 1.11633 * \text{Vsh}_{\text{ND}})$	PORC: 0.85 Vsh <sub>ND</sub> : 0.30
Multiple Regression: Total porosity & laminated shale after Thomas and Stieber (1975) Coefficient of correlation: 0.93	$\text{KLHC} = 10^{**}(-2.45166 - 1.12073 * \text{Vsh}_{\text{lam}} + 19.8134 * \text{PORC})$	PORC: 0.85 Vsh <sub>lam</sub> : 0.12
Multiple Regression: Total porosity & volume of shale after Thomas and Stieber (1975) Coefficient of correlation: 0.94	$\text{KLHC} = 10^{**}(-1.90812 + 18.4186 * \text{PORC} - 5.09559 * \text{Vsh}_{\text{dis}} - 1.30597 * \text{Vsh}_{\text{lam}})$	PORC: 0.85 Vsh <sub>dis</sub> : 0.30 Vsh <sub>lam</sub> : 0.12

## Appendix 8

Resultant regression lines for different input in well 7220/8-1 using total porosity estimated from density and sonic log (PHIT) where: KLHC – core corrected horizontal permeability; Vsh<sub>ND</sub> – volume of shale calculated from neutron-density separation; Vsh<sub>dis</sub> – dispersed (absolute) volume of shale calculated after Thomas and Stieber (1975); and Vsh<sub>lam</sub> – laminated volume of shale calculated after Thomas and Stieber (1975). Marked in yellow is the coefficient of correlation.

### Well 7220/8-1 (PHIT)

<i>Input</i>	<i>Regression</i>	<i>Correlation of dependent log and the independent log</i>
Simple regression total porosity Coefficient of correlation: 0.76	$\text{KLHC} = 10^{**}(-3.21225 + 21.2774 * \text{PHIT})$	PHIT: 0.58 Coefficient of correlation: 0.76
Multiple Regression: Total porosity & volume of shale from neutron-density separation Coefficient of correlation: 0.76	$\text{KLHC} = 10^{**}(-4.07116 + 23.896 * \text{PHIT} + 1.07718 * \text{Vsh}_{\text{ND}})$	PHIT: 0.58 Vsh <sub>ND</sub> : 0.31
Multiple Regression: Total porosity & laminated shale after Thomas and Stieber (1975) Coefficient of correlation: 0.76	$\text{KLHC} = 10^{**}(-3.04478 + 21.1114 * \text{PHIT} - 0.575695 * \text{Vsh}_{\text{lam}})$	PHIT: 0.58 Vsh <sub>lam</sub> : 0.12
Multiple Regression: Total porosity & volume of shale after Thomas and Stieber (1975) Coefficient of correlation: 0.76	$\text{KLHC} = 10^{**}(-2.17961 + 18.3998 * \text{PHIT} - 4.08132 * \text{Vsh}_{\text{dis}} - 0.870471 * \text{Vsh}_{\text{lam}})$	PHIT: 0.58 Vsh <sub>dis</sub> : 0.31 Vsh <sub>lam</sub> : 0.12

## Appendix 9

Resultant regression lines for different input in well 7220/7-1 using core corrected total porosity from routine core analysis (PORC) where: KLHC – core corrected horizontal permeability; Vsh<sub>ND</sub> – volume of shale calculated from neutron-density separation; Vsh<sub>dis</sub> – dispersed (absolute) volume of shale calculated after Thomas and Stieber (1975); and Vsh<sub>lam</sub> – laminated volume of shale calculated after Thomas and Stieber (1975). Marked in yellow is the coefficient of correlation

### Well 7220/7-1 (PORC)

<i>Input</i>	<i>Regression</i>	<i>Correlation of dependent log and the independent log</i>
Simple regression total porosity  <b>Coefficient of correlation: 0.90</b>	$\text{KLHC} = 10^{**}(-2.63552 + 24.3686 \cdot \text{PORC})$	PORC: 0.81
Multiple Regression: Total porosity & volume of shale from neutron-density separation  <b>Coefficient of correlation: 0.92</b>	$\text{KLHC} = 10^{**}(-1.745 + 21.4002 \cdot \text{PORC} - 0.962973 \cdot \text{Vsh}_{\text{ND}})$	PORC: 0.81 Vsh <sub>ND</sub> : 0.48
Multiple Regression: Total porosity & laminated shale after Thomas and Stieber (1975)  <b>Coefficient of correlation: 0.92</b>	$\text{KLHC} = 10^{**}(-1.7045 + 21.2897 \cdot \text{PORC} - 1.33575 \cdot \text{Vsh}_{\text{lam}})$	PORC: 0.81 Vsh <sub>lam</sub> : 0.43
Multiple Regression: Total porosity & volume of shale after Thomas and Stieber (1975)  <b>Coefficient of correlation: 0.92</b>	$\text{KLHC} = 10^{**}(-1.69767 + 21.2721 \cdot \text{PORC} - 0.0723935 \cdot \text{Vsh}_{\text{dis}} - 1.3388 \cdot \text{Vsh}_{\text{lam}})$	PORC: 0.81 Vsh <sub>dis</sub> : 0.06 Vsh <sub>lam</sub> : 0.43

## Appendix 10

Resultant regression lines for different input in well 7220/7-1 using total porosity estimated from density and sonic log (PHIT) where: KLHC – core corrected horizontal permeability; Vsh<sub>ND</sub> – volume of shale calculated from neutron-density separation; Vsh<sub>dis</sub> – dispersed (absolute) volume of shale calculated after Thomas and Stieber (1975); and Vsh<sub>lam</sub> – laminated volume of shale calculated after Thomas and Stieber (1975). Marked in yellow is the coefficient of correlation

<b>Well 7220/7-1 (PHIT)</b>		
<i>Input</i>	<i>Regression</i>	<i>Correlation of dependent log and the independent log</i>
Simple regression total porosity  <b>Coefficient of correlation: 0.76</b>	$\text{KLHC} = 10^{**}(-2.15508 + 21.4246 * \text{PHIT})$	PHIT: 0.59
Multiple Regression: Total porosity & volume of shale from neutron-density separation  <b>Coefficient of correlation: 0.76</b>	$\text{KLHC} = 10^{**}(-1.57424 + 19.2283 * \text{PHIT} - 0.521959 * \text{Vsh}_{\text{ND}})$	PHIT: 0.59 Vsh <sub>ND</sub> : 0.49
Multiple Regression: Total porosity & laminated shale after Thomas and Stieber (1975)  <b>Coefficient of correlation: 0.80</b>	$\text{KLHC} = 10^{**}(-0.731631 - 1.89589 * \text{Vsh}_{\text{lam}} + 16.4523 * \text{PHIT})$	PHIT: 0.59 Vsh <sub>lam</sub> : 0.43
Multiple Regression: Total porosity & volume of shale after Thomas and Stieber (1975)  <b>Coefficient of correlation: 0.79</b>	$\text{KLHC} = 10^{**}(-1.13743 + 17.7264 * \text{PHIT} + 3.09147 * \text{Vsh}_{\text{dis}} - 1.67939 * \text{Vsh}_{\text{lam}})$	PHIT: 0.59 Vsh <sub>dis</sub> : 0.06 Vsh <sub>lam</sub> : 0.43